OUKA
The University of Osaka
Institutional Knowledge Archive

Title	Elastic and Microwave-Absorption Properties of Chitin Nanofiber-Derived Carbon Honeycombs
Author(s)	Li, Xiang
Citation	大阪大学, 2023, 博士論文
Version Type	VoR
URL	https://doi.org/10.18910/93055
rights	
Note	

The University of Osaka Institutional Knowledge Archive : OUKA

https://ir.library.osaka-u.ac.jp/

The University of Osaka

Doctoral Dissertation

Elastic and Microwave-Absorption Properties of Chitin Nanofiber-Derived Carbon Honeycombs

キチンナノファイバー由来カーボンハニカム構造体の弾性および電磁波吸収特性

Xiang Li

June 2023

Graduate School of Engineering
Osaka University

Contents

General Introduction 1

1. Background 1

2. Use of unidirectional freeze-drying in the fabrication of anisotropic microstructures 1

3. Use of chemical treatment in the fabrication of defective carbon structures 4

4. Use of carbonization in the fabrication of sustainable biomass-derived carbon aerogels 5

5. Chitin nanofiber-derived carbon aerogels 9

6. Outline of This Thesis 9

7. References 10

Chapter 1. Chitin nanofiber-derived-carbon honeycomb with anisotropic porous channels and defective carbon structures for strong microwave absorption 15

1.1 Introduction 15

1.2 Experimental section 17

1.3 Results and discussion 19

1.4 Conclusion 34

1.5 References 34

Chapter 2. Frequency-tunable and absorption/transmission-switchable microwave absorber based on a chitin-nanofiber-derived elastic carbon honeycomb 37

2.1 Introduction 37

2.2 Experimental section 38

2.3 Results and discussion 42

2.4 Conclusion 57

2.5 References 58

Chapter 3. Super-compressible, elastic, and robust chitin nanofiber-derived carbon honeycomb and its pressure sensing properties over an ultrawide temperature range ..61

3.1 Introduction 61

3.2 Experimental section 63

3.3 Results and discussion 65

3.4 Conclusion 78

3.5 References 79

Conclusions 82

List of Publications 83

Copyright 84

Acknowledgement 85

General Introduction

1. Background

Aerogels, first invented by Dr. Kistler in 1931, are prepared by replacing the liquid inside a gel with gas, producing a solid material with little or no shrinkage. The first-invented aerogel was an ultralight, porous silica material,[1] with a density close to that of air.[2,3] Carbon aerogels[4,5] have received increasing interest among the various materials that are being developed, owing to their light weight, high thermal stability, large specific surface area, and unique electrical properties (**Fig. 1**).[6,7,8] Carbon aerogels based on graphene,[9] carbon nanotubes,[10] and carbon nanofibers[11]have been fabricated, and the development of high-performance carbon aerogels requires the appropriate design of their microstructures and defective carbon structures.

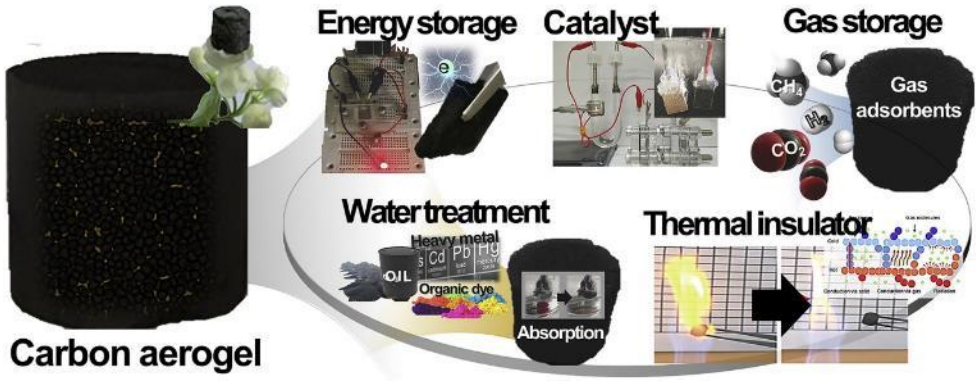


Fig. 1 Carbon aerogel applications. The unique features of carbon aerogels, such as low weight, high thermal stability, and large specific surface area, and their unique electric properties make them suitable for use in various applications, including energy storage, catalysis, gas storage, water treatment, and thermal insulation.[8] Reprinted from Ref. 8.

2. Use of unidirectional freeze-drying in the fabrication of anisotropic microstructures

Ice crystals have emerged as a promising template material and are widely used in the preparation of aerogels and scaffolds.[12,13] In a typical ice-templating process, a gel, sol, or slurry dispersed in water is first frozen and the phase separation that occurs during the process, produces a solidified solvent, which can be used as a template.[14,15] By using directional freezing (directional temperature gradient) and maintaining a constant freezing velocity, the ice crystals can be controlled to grow directionally and produce unique microstructures (**Fig. 2**).[2,16] Mahler and Bechtold reported that by

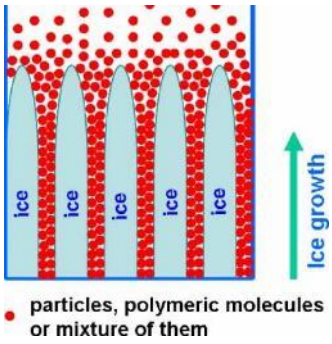


Fig. 2 A typical ice-crystal grown model in an aqueous mixture.[16] Reprinted from Ref. 16.

freezing aqueous silicic acid in a controlled direction, nano/micro-scale fibers with flake-like blocks, honeycomb-like porous structures, and polygonal-like cross-sections could be formed.[17] Moreover, the diameter of each fiber produced via unidirectional freezing was almost constant along its entire length. The fiber diameter can become uniform when silica hydrogel is completely and unidirectionally frozen under conditions in which pseudo−steady-state growth of ice crystals can occur.[2] The fully frozen sample was subsequently transferred to a depressurizing system that used a freeze-dryer or supercritical dryer for directly replacing the solidified solvent template with gas, which was removed by sublimation.[18,19] In this way, the structural framework can be retained well, yielding a well-shaped porous structure, such as the aligned channel structure (**Figs. 3a–b**), pores (**Fig. 3c**), and 'tubule' structures (**Fig. 3d**).[14] Thus, unidirectional freeze-drying is a promising method that can be used to fabricate functional materials with tailored nano/microstructures. However, the microstructures formed via unidirectional freeze-drying are highly dependent on the chemical and physical properties of the precursor used.[20,21] Free-standing three-dimensional (3D) microstructures are hardly formed when the precursor is unable to form a continuous interconnected framework of microstructures.[22]

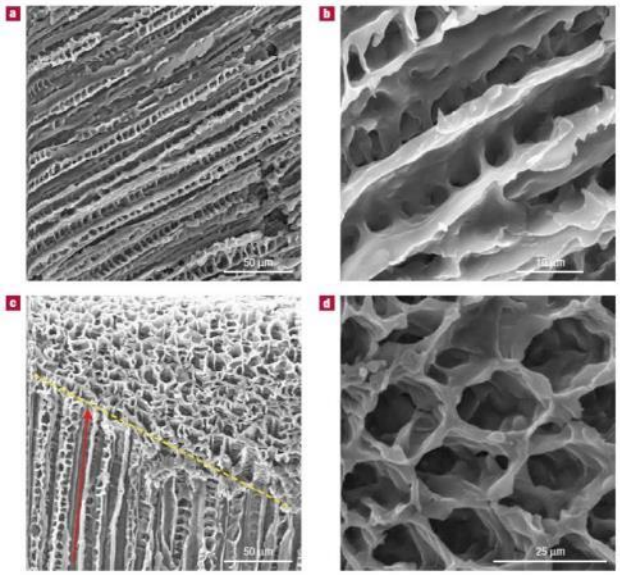


Fig. 3 Scanning electron microscopy images of aligned porous Polycaprolactone material (PCL) formed using directional freezing of a solution of PCL (10 wt%, number average molecular weight Mn =10,000 g mol^{-1}) in dichloroethane. (a) and (b) Aligned channel structure of a sample sectioned along the aligned axis. (c) Sample surface cross sections parallel and perpendicular to the aligned axis. The intersection between the aligned axis (red arrow) and perpendicular cross-section of the sample surface is shown by the dashed yellow line. (d) Close-up image of the aligned pores or 'tubule' structures that can be observed on the perpendicular cross section of the sample surface shown in (c).[14] Reprinted from Ref. 14.

Using the unidirectional freeze-drying method, one-dimensional silicon nanofibers and two-dimensional graphene-based aerogels with continuously interconnected frameworks and anisotropic microstructures have been formed.[18,23] Qiu et al.[24] reported that graphene chemistry along with ice physics could facilitate the fabrication of lightweight and elastic graphene-based aerogels with cellular-like structures. These graphene-based aerogels, mimicking natural cork,

demonstrated structural integrity under a load 50,000 times its weight and rapidly recovered from 80% compression (**Fig. 4a**). Gao et al.[25,26] demonstrated a carbon material prepared using bidirectional freeze-drying through which ice crystals were grown as a plane. After eliminating the in-plane ice crystals, a hierarchical lamellar architecture comprising numerous microscale arches was obtained, endowing the carbon aerogel with elasticity and high fatigue resistance to mechanical compression (**Fig. 4b**). Nishihara and collaborators[27] mimicked the xylem structure of a tree using cellulose and graphene, the major components of a tree structure, via unidirectional freeze-drying to produce wood-like carbon monoliths (**Fig. 4c**). Ding et al.[28,29] used unidirectional freeze-drying to create superelastic konjac glucomannan biomass/SiO_2 nanofiber-derived nanofibrous carbon aerogels with an orderly anisotropic microstructure (**Fig. 4d**). Thus, designing the anisotropic microstructures of a carbon aerogel using the unidirectional freeze-drying method would be effective.

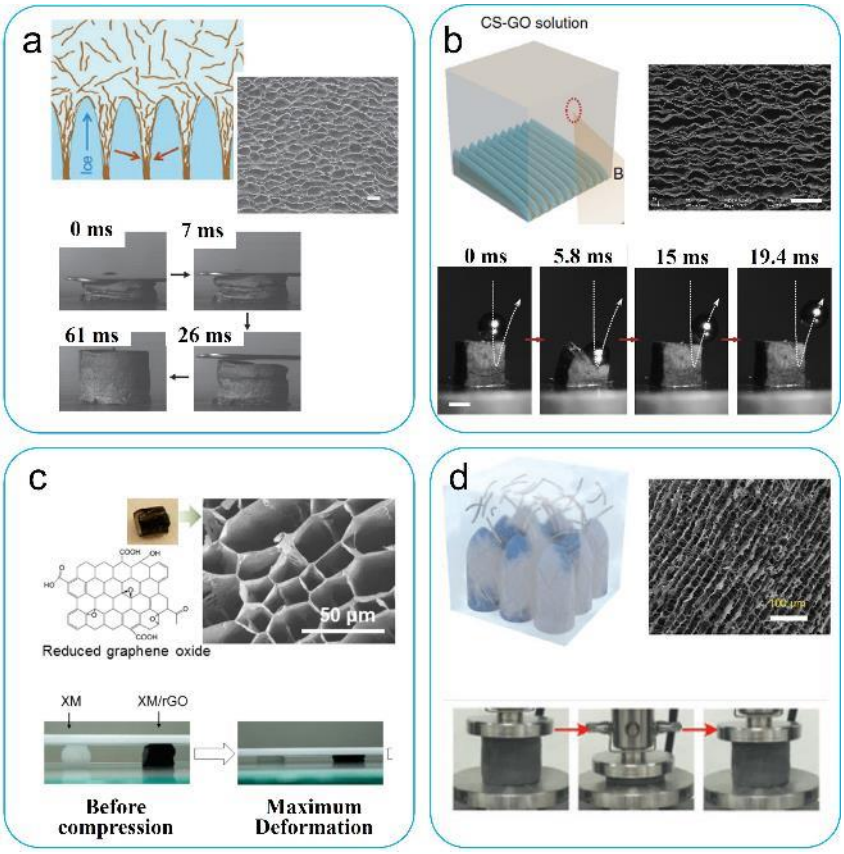


Fig. 4 (a) Unidirectional freeze-drying of graphene aerogel with excellent compressibility.[24] (b) Bidirectional freeze-drying of chitosan/graphene oxide-derived carbon aerogel with superelasticity.[25] (d) Unidirectional freeze-drying of cellulose/graphene monolith with maximum deformation properties.[27] (e) Unidirectional freeze-drying of konjac glucomannan/SiO_2 nanofiber-derived carbon aerogel with superelasticity.[28] (Reprinted and modified from Refs. 24, 25, 27, and 28)

Anisotropic microstructures, such as cellular-,[30] lamellar-,[31] wood-,[32] and honeycomb-like[10] microstructures, can endow carbon aerogels with elastic and tunable electric properties in a direction perpendicular to the designed microstructures.[33] When honeycomb-structured carbon aerogels were examined, inspired by natural honeycombs and their anisotropic microstructures,[34,35] they were found to exhibit apparent densities similar to those of typical aerogels[36] and were found to be structurally robust because of the formation of a "Steiner tree" geometry by their closely connected cell walls (**Fig. 5a**).[37,38] This particular geometry of the honeycomb-structured carbon aerogels could efficiently dissipate mechanical strength and guide the deformations, thereby preventing local large deformations and structural damage (**Fig. 5b**).[39] Therefore, a carbon aerogel with uniform anisotropic honeycomb microstructures will be in high demand and can be fabricated using the unidirectional freeze-drying method, which would encourage the development of their diverse applications, such as flexible energy storage, pressure sensing, and microwave absorption.

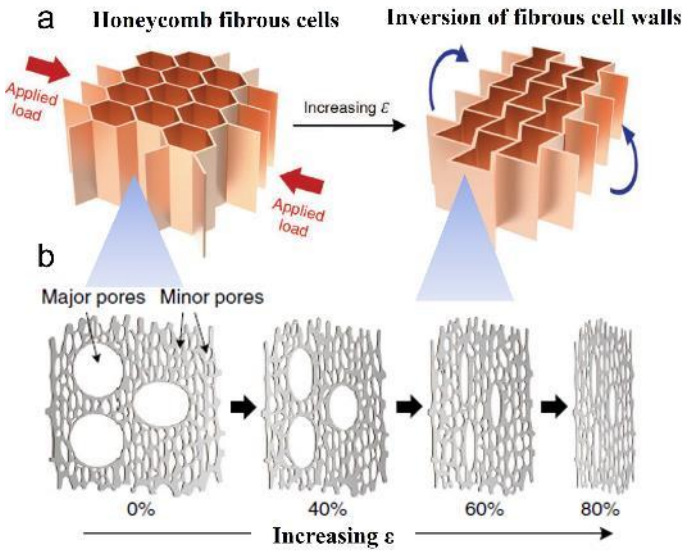


Fig. 5 (a) Schematic illustration of the honeycomb-like structures and inversion of their nanofibrous cell walls with compression strains.[28] Reprinted and modified from Ref. 28. (b) Schematic illustration of the deformation of the honeycomb-like channel walls with hierarchical major and minor pores within them.[33] Reprinted and modified from Ref. 33.

3. Use of chemical treatment in the fabrication of defective carbon structures

The fabrication of defective carbon structures of carbon aerogels using methods such as N-doping via post-chemical treatment with aniline,[40] pyrrole,[41] and amines,[42,43] can generate active sites and tailor the dielectric properties of the carbon aerogels (**Fig. 6**). N-doped carbon aerogels have exhibited excellent catalytic properties, which are superior to those of

commercially available Pt/C catalysts;[44,45] these carbon aerogels are used in energy storage applications, such as fuel cells[46] and metal–air batteries, in the form of metal-free catalysts[47]. For example, graphene[48] and carbon nanotubes[49] doped with pyridinic and pyrrolic N species using $Fe(NO)_3 \cdot 9H_2O$ as the N source showed higher electrocatalytic activity than Pt/C. Moreover, the dielectric polarization of a material can be enhanced using N-doping.[50] For example, Liu et al.[51] prepared N-doped graphene foams with excellent dielectric loss properties, showing a maximum microwave absorption of -53.9 dB, which they attributed to heteroatom doping. Zhou and coworkers[52] synthesized a heteroatom-regulated N-doping carbon aerogel, which demonstrated an optimal microwave absorption of -61.7 dB at 2.6 mm. Urea was used as the N source in both cases. Thus, the appropriate design of microstructures and defective carbon structures has become promising in the fabrication of carbon aerogels with tunable electric and dielectric properties , designed for diverse functional applications, including energy storage,[10] catalysis,[53] sensing,[9] and microwave absorption.[54] However, chemicals such as aniline,[40] pyrrole,[41] amines,[42,43] nitrates,[49] and urea[52] are inevitably used in the fabrication of these carbon aerogels.

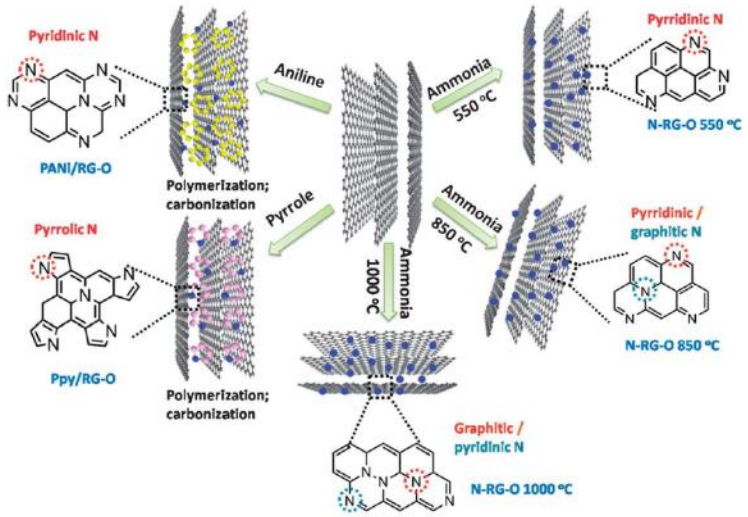


Fig. 6 Schematic diagram showing the preparation of N-doped graphene with different N states. N-RG-O are prepared by annealing G-O powder at 550, 850, and 1000 °C with $NH_3 \cdot N$ as the precursor. PANi/RG-O and Ppy/RG-O are prepared by annealing PANi/G-O and Ppy/G-O composites at 850 °C.[47] Reprinted from Ref. 47.

4. Use of carbonization in the fabrication of sustainable biomass-derived carbon aerogels

The use of fossil resources and its post-chemical-treatment using toxic chemicals have to be avoided in the pursuit of sustainable development; thus carbon aerogels with 3D

microstructures and N-doped carbon structures can be obtained by carbonizing biomass materials.[55] Biomass, containing polysaccharides, lignin, and protein, is a sustainable earth resource, which is abundantly available and inexpensive;[56] it contains heteroatoms, such as H, O, and N. within its carbon molecular chains, which could be easily converted into heteroatom-doped carbon materials.[57] Moreover, various types of biomass, including protein,[18] bacterial cellulose,[58] watermelons,[59] gelatin,[60] and winter melon,[61] have been utilized as precursors to prepare carbonaceous aerogels using hydrothermal or inert gas carbonization methods (**Fig. 7**). For example, Nogi[62] reported that carbon nanofiber aerogels could be fabricated from bionanofiber/water suspensions via solvent exchange and freeze-drying. N/O-doped and O-doped defective carbons can be obtained by tailoring the bionanofiber resources of prawn chitin and wood cellulose, respectively. However, the random porous structures of bulk biomass-derived carbons and the high weight loss and volume shrinkage of their precursors, make certain features of these carbons, such as porosity, mechanical properties, and conductivity, inferior to those of petroleum-derived carbons.[63] Thus, these major challenges encountered in fabricating biomass-derived carbon aerogels have to be addressed.

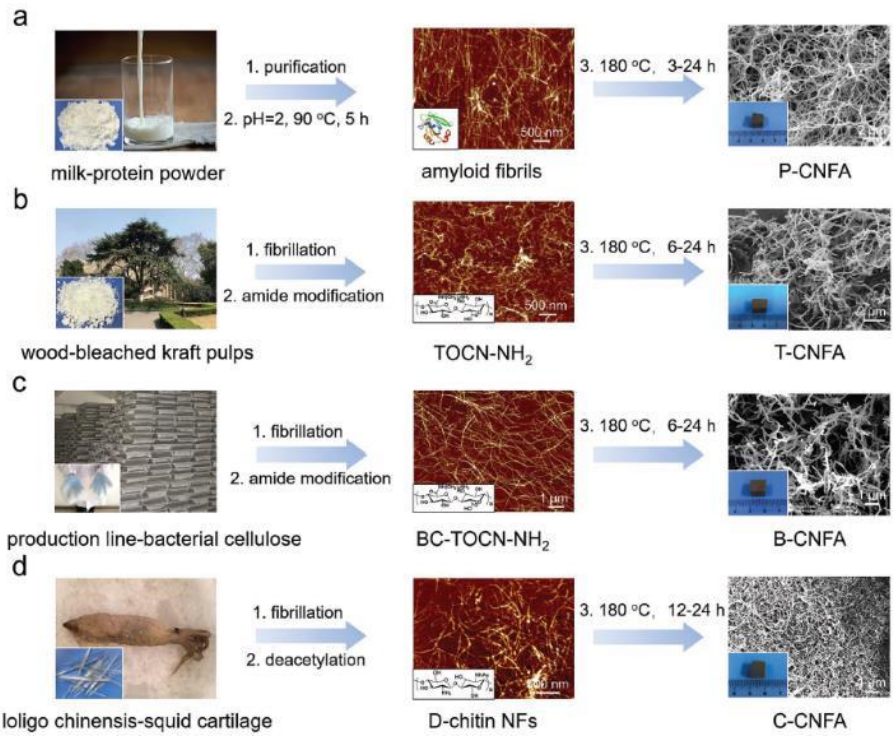


Fig. 7 Schematic illustration of the preparation of carbon nanofibrous aerogels using all biomass precursors. (a) Amyloid fibril template-directed hydrothermal carbonization. (b) TOCN-NH_2 template-directed hydrothermal carbonization. (c) BC-TOCN-NH_2 template-directed hydrothermal carbonization. (d) D-chitin nanofiber template-directed hydrothermal carbonization.[18] Reprinted from Ref. 18.

To address the challenges mentioned, tailoring of anisotropic microstructures of biomass-derived carbon aerogels has been explored.[64] For example, Zhong et al. prepared a biomass-derived carbon aerogel based on chitosan that had nano-reinforcement or support from cellulose nanocrystals (**Fig. 8a**); the resulting carbon aerogel had lamellar-like anisotropic microstructures and an excellent sensitivity of 103.5 kPa^{-1} with a wide linear sensitivity between 0 and 18 kPa (**Fig. 8b**).[65] Peng et al. developed a cellulose nanofiber/lignin-derived composite carbon aerogel; the lignin in the aerogel acted as a "glue" that prevented the volume and shape shrinkage of the cellulose nanofibers (**Fig. 8c**), thereby realizing wood-like anisotropic porous channels and an enhancement in elasticity and fatigue resistance after 30,000 cycles at 50% compressive strain (**Fig. 8d**).[32] However, the reported biomass-derived carbon aerogels were composited with crosslinkers or thermally stable materials to prevent their morphological shrinkage during carbonization; further functionalization and practical application of single-component biomass-derived carbon aerogels remain a challenge due to the difficulties faced during the design of their microstructures and defective carbon structures.

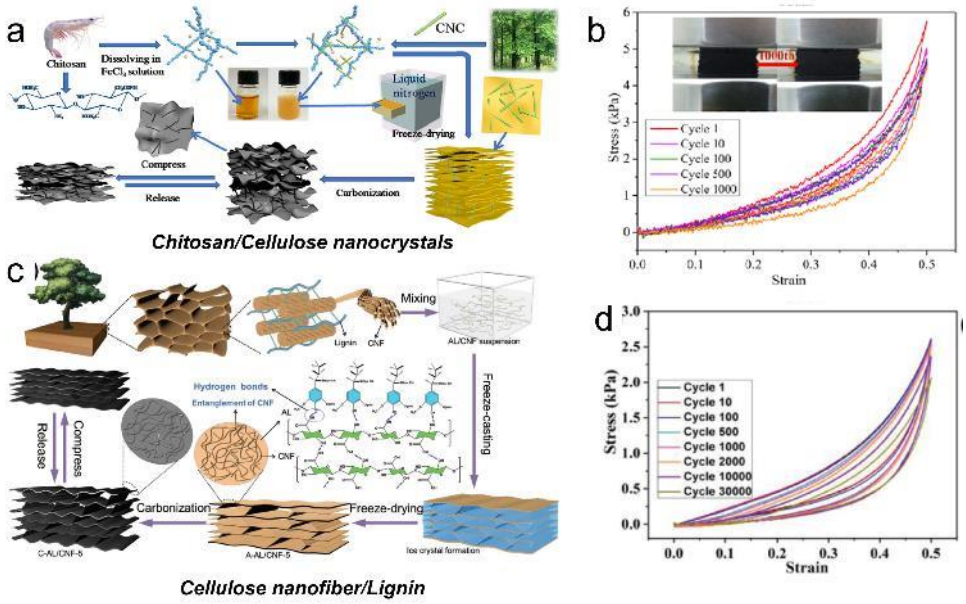


Fig. 8 (a) Schematic illustration of chitosan/cellulose nanocrystal aerogel fabrication and corresponding carbon aerogels using $FeCl_3$ as a crosslinker. (b) Elastic properties of the chitosan/cellulose nanocrystal-derived carbon aerogels subjected up to 1,000 cycles of compression at 50% strain.[65] Reprinted and modified from Ref. 65. (c) Schematic illustration of cellulose nanofiber/lignin aerogel fabrication and corresponding carbon aerogel fabrication using the unidirectional freeze-drying method. (d) Elastic properties of the cellulose nanofiber/lignin-derived carbon aerogel up to 30000 cycles of compression at 50% strain.[32] Reprinted and modified from Ref. 32.

Bio-nanofibers, a biomass material, can be used as building blocks when designing 3D interconnected microstructures.[66] Cellulose nanofibers are one of the most abundant bio-nanofibers on earth (**Fig. 9a**).[67,68] The microstructures of carbonized cellulose nanofibers should have high morphological stability against high-temperature carbonization (**Fig. 9b**).[69] The original morphologies of cellulose nanofibers collapse during high-temperature carbonization. Koga found that the I_2 treatment of cellulose nanofibers could enhance their carbon yield, thereby protecting them from structural collapse during high-temperature carbonization (**Fig. 9e**).[66] The resulting cellulose nanofibers showed excellent electrical conductivity. Therefore, bio-nanofibers, such as natural N-doped bio-nanofibers, with a high carbon yield and a thermal stability similar to that of I_2-doped cellulose nanofibers are promising materials that would maintain their morphological stability while undergoing high-temperature carbonization.

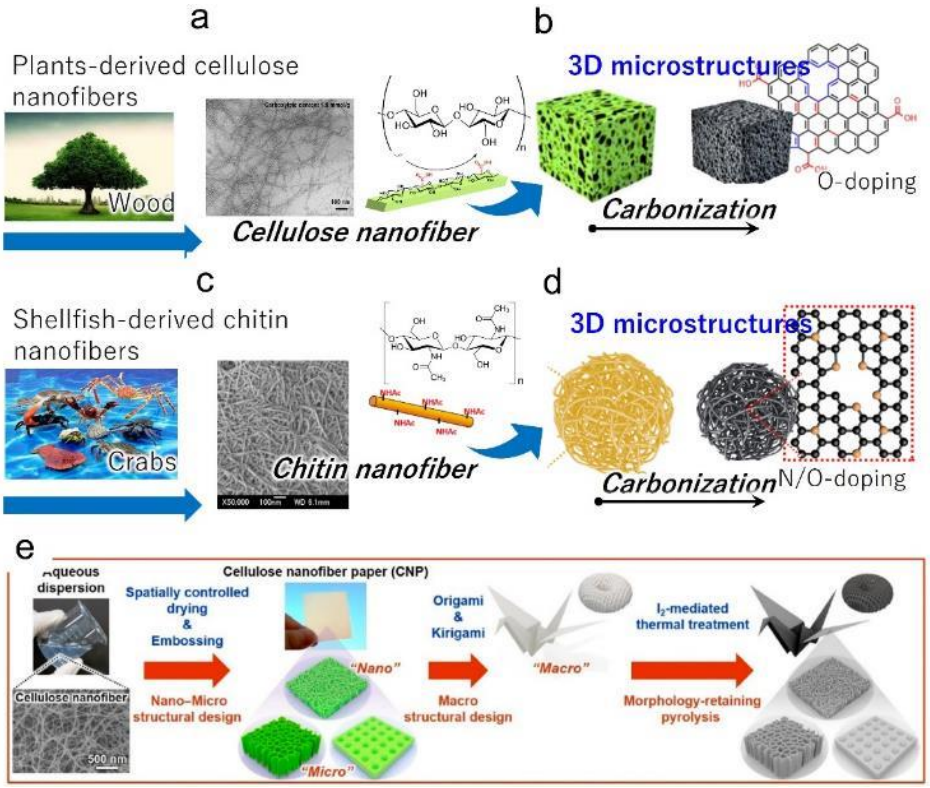


Fig. 9 Bio-nanofibers used as building blocks in the design of three-dimensional (3D) microstructures. (a) Field emission scanning electron microscopy (FE-SEM) images and molecular structures of plant-derived cellulose nanofibers.[68] (b) Cellulose nanofiber-derived carbons with 3D microstructures and defective carbon structures.[69] (c) FE-SEM images and molecular structures of crab-shell-derived chitin nanofibers.[70] (d) Chitin nanofiber-derived carbons with 3D microstructures and defective carbon structures.[71] (e) Nano−micro−macro-structural design and morphology-retaining pyrolysis of cellulose nanofibers using I_2 treatment.[66] Reprinted and modified from Refs. 66, 68, 69, 70, and 71.

5. Chitin nanofiber-derived carbon aerogels

Chitin nanofibers (β-(1-4)-linked 2-acetamido-2-deoxy-D-glucopyranose)[72] maintain a higher morphological stability than cellulose nanofibers when undergoing carbonization (**Fig. 10**).[62,73] Moreover, chitin nanofibers intrinsically contain N atoms derived from their N-acetyl groups,[74] providing an opportunity for enhancing their carbon yield and N doping toward designing defective carbon structures via carbonization (**Figs. 9c–d**).[75,71] The defective carbon structures can be further tailored via carbonization at different temperatures. Thus, chitin nanofibers would be promising building blocks that can be used in the fabrication of carbon aerogels with 3D anisotropic microstructures and defective carbon structures.

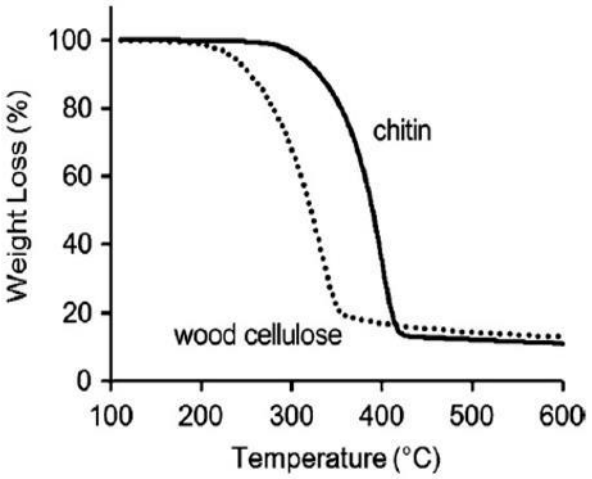


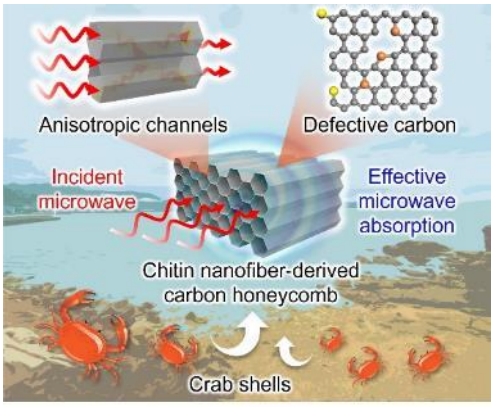
Fig. 10 Thermogravimetric curves of chitin and wood cellulose nanofibers. Reprinted from Ref. 62.

6. Outline of This Thesis

In this dissertation, a crab-shell-derived chitin nanofiber/water dispersion was fabricated into carbon aerogels with anisotropic honeycomb-like microstructures (denoted as carbon honeycomb) by unidirectional freeze drying and subsequent carbonization. The anisotropic microstructures and defective carbon structures of the carbon honeycomb were tailored by controlling the chitin nanofiber concentration and the carbonization temperature to provide elastic, electric, and dielectric properties for microwave absorption and pressure sensing.

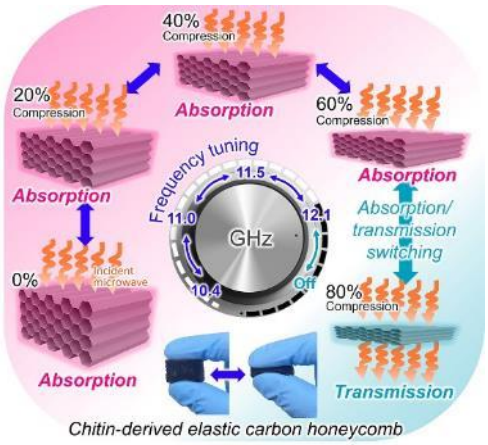
Chapter 1

A chitin nanofiber-derived carbon honeycomb was prepared at different temperatures to tailor its dielectric properties (i.e., impedance matching, conductive loss, and polarization loss) for microwave absorption. The carbon honeycomb carbonized at 800 °C achieved strong microwave absorption, owing to its good impedance matching, moderate conductive loss, and high polarization loss.



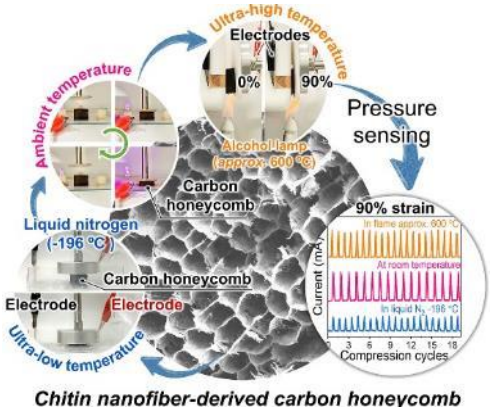
Chapter 2

The elastic properties of the carbon honeycomb carbonized at 800 °C were elaborated for smart microwave absorption. The elastic carbon honeycomb afforded absorption-frequency tuning and absorption/transmission switching upon its controlled compression.



Chapter 3

The elastic properties, such as compressibility and fatigue resistance, of the carbon honeycomb were further enhanced by optimizing the chitin nanofiber concentration and the carbonization temperature. The carbon honeycomb fabricated at 1.0 wt.% and 900 °C provided excellent elastic properties, which are superior even to the state-of-the-art carbon aerogels. Moreover, its high thermal stability even in flame and liquid nitrogen allow effective sensing over an ultrawide pressure and temperature range.



7. References

1 W. Mahler and M. F. Bechtold, *Nature*, 1980, **285**, 1–2.

2 S. R. Mukai, H. Nishihara and H. Tamon, *Chem. Commun.*, 2004, **4**, 874–875.

3 S. P. Patil, A. Rege, Sagardas, M. Itskov and B. Markert, *J. Phys. Chem. B*, 2017, **121**, 5660–5668.

4 H. Hu, Z. Zhao, W. Wan, Y. Gogotsi and J. Qiu, *Adv. Mater.*, 2013, **25**, 2219–2223.

5 S. M. Alatalo, K. Qiu, K. Preuss, A. Marinovic, M. Sevilla, M. Sillanpää, X. Guo and M. M. Titirici, *Carbon*, 2016, **96**, 622–630.

6 G. Ye, X. Zhu, S. Chen, D. Li, Y. Yin, Y. Lu, S. Komarneni and D. Yang, *J. Mater. Chem. A*, 2017, **5**, 8247–8254.

7 K. H. Kim, Y. Oh and M. F. Islam, *Nat. Nanotechnol.*, 2012, **7**, 562–566.

8 J. H. Lee and S. J. Park, *Carbon*, 2020, **163**, 1–18.

9 J. Xiao, Y. Tan, Y. Song and Q. Zheng, *J. Mater. Chem. A*, 2018, **6**, 9074–9080.

10 H. Liu, T. Xu, C. Cai, K. Liu, W. Liu, M. Zhang, H. Du, C. Si and K. Zhang, *Adv. Funct. Mater.*, 2022, **32**, 2113082.

11 T. Kshetri, D. Tran, D. Nguyen, N. Kim, K. Lau and J. Lee, *Chem. Eng. J.*, 2020, **380**, 122543.

12 S. Deville, E. Saiz, R. K. Nalla and A. P. Tomsia, *Science*, 2006, **311**, 515–518.

13 H. Bai, Y. Chen, B. Delattre, A. P. Tomsia and R. O. Ritchie, *Sci. Adv.*, 2015, **1**, 1–9.

14 H. Zhang, I. Hussain, M. Brust, M. F. Butler, S. P. Rannard and A. I. Cooper, *Nat. Mater.*, 2005, **4**, 787–793.

15 D. Jiang, J. Zhang, S. Qin, Z. Wang, K. A. S. Usman, D. Hegh, J. Liu, W. Lei and J. M. Razal, *ACS Nano*, 2021, **15**, 5000–5010.

16 L. Qian and H. Zhang, *J. Chem. Technol. Biotechnol.*, 2011, **86**, 172–184.

17 W. Mahler and M. F. Bechtold, *Nature*, 1980, **285**, 27–28.

18 B. C. Hu, H. R. Zhang, S. C. Li, W. S. Chen, Z. Y. Wu, H. W. Liang, H. P. Yu and S. H. Yu, *Adv. Funct. Mater.*, 2023, **33**, 2207532.

19 X. Zhang, H. Wang, Z. Cai, N. Yan, M. Liu and Y. Yu, *ACS Sustain. Chem. Eng.*, 2019, **7**, 332–340.

20 T. Chen, M. Li, L. Zhou, X. Ding, D. Lin, T. Duan, G. Yang, R. He and W. Zhu, *ACS Sustain. Chem. Eng.*, 2020, **8**, 6458–6465.

21 Y. Wang, H. Qin, Z. Li, J. Dai, H.-P. Cong and S.-H. Yu, *Nat. Synth.*, 2022, **1**, 975–986.

22 Y. Ma and Y. Chen, *Natl. Sci. Rev.*, 2015, **2**, 40–53.

23 H. Qin, Y. Zhang, J. Jiang, L. Wang, M. Song, R. Bi, P. Zhu and F. Jiang, *Adv. Funct. Mater.*, 2021, 1–9.

24 L. Qiu, J. Z. Liu, S. L. Y. Chang, Y. Wu and D. Li, *Nat. Commun.*, 2012, **3**, 1–7.

25 H. L. Gao, Y. B. Zhu, L. B. Mao, F. C. Wang, X. S. Luo, Y. Y. Liu, Y. Lu, Z. Pan, J. Ge, W. Shen, Y. R. Zheng, L. Xu, L. J. Wang, W. H. Xu, H. A. Wu and S. H. Yu, *Nat. Commun.*, 2016, **7**, 1–8.

26 H. L. Gao, Z. Y. Wang, C. Cui, J. Z. Bao, Y. B. Zhu, J. Xia, S. M. Wen, H. A. Wu and S. H. Yu, *Adv. Mater.*, 2021, 2102724.

27 Z. Z. Pan, H. Nishihara, S. Iwamura, T. Sekiguchi, A. Sato, A. Isogai, F. Kang, T.

Kyotani and Q. H. Yang, *ACS Nano*, 2016, **10**, 10689–10697.

28 Y. Si, X. Wang, C. Yan, L. Yang, J. Yu and B. Ding, *Adv. Mater.*, 2016, **28**, 9512–9518.

29 F. Wu, S. Qiang, X. D. Zhu, W. Jiao, L. Liu, J. Yu, Y. T. Liu and B. Ding, *Nano-Micro Lett.*, 2023, **15**, 1–15.

30 L. Qiu, J. Z. Liu, S. L. Y. Chang, Y. Wu and D. Li, *Nat. Commun.*, 2012, **3**, 1241.

31 H. L. Gao, Y. B. Zhu, L. B. Mao, F. C. Wang, X. S. Luo, Y. Y. Liu, Y. Lu, Z. Pan, J. Ge, W. Shen, Y. R. Zheng, L. Xu, L. J. Wang, W. H. Xu, H. A. Wu and S. H. Yu, *Nat. Commun.*, 2016, **7**, 12920.

32 Z. Chen, H. Zhuo, Y. Hu, H. Lai, L. Liu, L. Zhong and X. Peng, *Adv. Funct. Mater.*, 2020, **30**, 1910292.

33 Y. Si, J. Yu, X. Tang, J. Ge and B. Ding, *Nat. Commun.*, 2014, **5**, 5802.

34 M. Murcia-Morales, M. J. Gómez-Ramos, P. Parrilla-Vázquez, F. J. Díaz-Galiano, M. García-Valverde, V. Gámiz-López, J. Manuel-Flores and A. R. Fernández-Alba, *Sci. Total Environ.*, 2020, **710**, 136288.

35 H. Liu, X. Chen, Y. Zheng, D. Zhang, Y. Zhao, C. Wang, C. Pan, C. Liu and C. Shen, *Adv. Funct. Mater.*, 2021, **31**, 2008006.

36 J. Jiang, H. Oguzlu and F. Jiang, *Chem. Eng. J.*, 2021, **405**, 126668.

37 F. K. Hwang and D. S. Richards, *Networks*, 1992, **22**, 55–89.

38 H. Yu, Q. Zhang, B. P. Cumming, E. Goi, J. H. Cole, H. Luan, X. Chen and M. Gu, *Adv. Sci.*, 2021, **8**, 2100141.

39 M. F. Ashby and R. F. M. Medalist, *Metall. Trans. A*, 1983, **14**, 1755–1769.

40 G. Wang, Y. Sun, D. Li, H.-W. Liang, R. Dong, X. Feng and K. Müllen, *Angew. Chemie*, 2015, **127**, 15406–15411.

41 L. W. Lin, M. Qi, Z. T. Bai, S. X. Yan, Z. Y. Sui, B. H. Han and Y. W. Liu, *Appl. Surf. Sci.*, 2021, **555**, 149717.

42 B. M. Matsagar, R. Yang, S. Dutta, Y. Ok and K. Wu, *J. Mater. Chem. A*, 2021, **9**, 3703–3728.

43 D. Hulicova-Jurcakova, M. Kodama, S. Shiraishi, H. Hatori, Z. H. Zhu and G. Q. Lu, *Adv. Funct. Mater.*, 2009, **19**, 1800–1809.

44 L. Qu, Y. Liu, J. B. Baek and L. Dai, *ACS Nano*, 2010, **4**, 1321–1326.

45 D. Geng, Y. Chen, Y. Chen, Y. Li, R. Li, X. Sun, S. Ye and S. Knights, *Energy Environ. Sci.*, 2011, **4**, 760–764.

46 L. Álvarez-Manuel, C. Alegre, D. Sebastián, A. Eizaguerri, P. F. Napal and M. J. Lázaro, *Catal. Today*, 2023, **418**, 114067.

47 L. Lai, J. R. Potts, D. Zhan, L. Wang, C. K. Poh, C. Tang, H. Gong, Z. Shen, J. Lin and R. S. Ruoff, *Energy Environ. Sci.*, 2012, **5**, 7936–7942.

48 L. Feng, Y. Yan, Y. Chen and L. Wang, *Energy Environ. Sci.*, 2011, **4**, 1892–1899.

49 D. R. Paul, W. J. Koros, R. Y. F. Liu, Y. S. Hu, E. Baer, A. Hiltner, H. D. Keith, R. Y. F. Liu, A. Hiltner, E. Baer, R. E. Cohen, A. Bellare, R. J. Albalak, W. Hu and G. Reiter, *Science*, 2009, **323**, 760–764.

50 F. Meng, H. Wang, F. Huang, Y. Guo, Z. Wang, D. Hui and Z. Zhou, *Compos. Part B Eng.*, 2018, **137**, 260–277.

51 P. Liu, Y. Zhang, J. Yan, Y. Huang, L. Xia and Z. Guang, *Chem. Eng. J.*, 2019, **368**, 285–298.

52 P. Liu, S. Gao, C. Chen, F. Zhou, Z. Meng, Y. Huang and Y. Wang, *Carbon*, 2020, **169**, 276–287.

53 C. Moreno-Castilla and F. J. Maldonado-Hódar, *Carbon*, 2005, **43**, 455–465.

54 F. Sultanov, C. Daulbayev, B. Bakbolat and O. Daulbayev, *Adv. Colloid Interface Sci.*, 2020, **285**, 102281.

55 H. Zhao, Y. Cheng, W. Liu, L. Yang, B. Zhang, L. P. Wang, G. Ji and Z. J. Xu, *Nano-Micro Lett.*, 2019, **11**, 1–17.

56 L. D. Gomez, C. G. Steele-King and S. J. McQueen-Mason, *New Phytol.*, 2008, **178**, 473–485.

57 L. Gao, J. Ma, S. Li, D. Liu, D. Xu, J. Cai, L. Chen, J. Xie and L. Zhang, *Nanoscale*, 2019, **11**, 12626–12636.

58 Z. Y. Wu, H. W. Liang, L. F. Chen, B. C. Hu and S. H. Yu, *Acc. Chem. Res.*, 2016, **49**, 96–105.

59 X. L. Wu, T. Wen, H. L. Guo, S. Bin Yang, X. K. Wang and A. W. Xu, *ACS Nano*, 2013, **7**, 3589–3597.

60 Z. Ling, Z. Wang, M. Zhang, C. Yu, G. Wang, Y. Dong, S. Liu, Y. Wang and J. Qiu, *Adv. Funct. Mater.*, 2016, **26**, 111–119.

61 Y. Q. Li, Y. A. Samad, K. Polychronopoulou, S. M. Alhassan and K. Liao, *ACS Sustain. Chem. Eng.*, 2014, **2**, 1492–1497.

62 M. Nogi, F. Kurosaki, H. Yano and M. Takano, *Carbohydr. Polym.*, 2010, **81**, 919–924.

63 H. W. Liang, Q. F. Guan, Z. Z. Zhu, L. T. Song, H. Bin Yao, X. Lei and S. H. Yu, *NPG Asia Mater.*, 2012, **4**, 1–6.

64 C. Li, Y. W. Ding, B. C. Hu, Z. Y. Wu, H. L. Gao, H. W. Liang, J. F. Chen and S. H. Yu, *Adv. Mater.*, 2020, **32**, 1–7.

65 Y. Hu, H. Zhuo, Z. Chen, K. Wu, Q. Luo, Q. Liu, S. Jing, C. Liu, L. Zhong, R. Sun and X. Peng, *ACS Appl. Mater. Interfaces*, 2018, **10**, 40641–40650.

66 H. Koga, K. Nagashima, K. Suematsu, T. Takahashi, L. Zhu, D. Fukushima, Y. Huang, R. Nakagawa, J. Liu, K. Uetani, M. Nogi, T. Yanagida and Y. Nishina, *ACS Nano*, 2022, **16**, 8630–8640.

67 J. Rostami, K. Gordeyeva, T. Benselfelt, E. Lahchaichi, S. A. Hall, A. V. Riazanova, P. A. Larsson, G. Cinar Ciftci and L. Wågberg, *Mater. Today*, 2021, **48**, 47–58.

68 T. Saito, S. Kimura, Y. Nishiyama and A. Isogai, *Biomacromolecules*, 2007, **8**, 2485–2491.

69 X. Li, Y. Zhang, J. Zhang and C. Wang, *Nanoscale*, 2019, **11**, 23110–23115.

70 S. Ifuku, *Molecules*, 2014, **19**, 18367–18380.

71 B. Duan, X. Gao, X. Yao, Y. Fang, L. Huang, J. Zhou and L. Zhang, *Nano Energy*, 2016, **27**, 482–491.

72 S. Ifuku and H. Saimoto, *Nanoscale*, 2012, **4**, 3308–3318.

73 X. Li, L. Zhu, T. Kasuga, M. Nogi and H. Koga, *Chem. Eng. J.*, 2022, **450**, 137943.

74 Y. Tsutsumi, H. Koga, Z. D. Qi, T. Saito and A. Isogai, *Biomacromolecules*, 2014, **15**, 4314–4319.

75 L. Zhu, Y. Huang, Y. Morishita, K. Uetani, M. Nogi and H. Koga, *J. Mater. Chem. C*, 2021, **9**, 4444–4452.

Chapter 1. Chitin nanofiber-derived-carbon honeycomb with anisotropic porous channels and defective carbon structures for strong microwave absorption

1.1 Introduction

In recent decades, the rapid evolution of wireless electronics has resulted in severe electromagnetic interference, which is an omnipresent issue that affects the normal operation of precision instruments and the health of human beings [1,2]. Tremendous developments have been made in microwave absorption materials to address excessive electromagnetic pollution [3,4,5]. Carbon materials, including graphene [6], carbon nanotubes [7], and carbonized biomass [8], have attracted much attention because of their unique advantages; for example, they are lightweight and have good chemical stability and broadband absorption properties [9], and can be functionalized to meet the use in multiple scenes [10]. Given the urgent demand for high-performance microwave-absorption materials [11], the further functional design of carbon materials to enhance their microwave absorption performance has gained prominence.

The leading strategies to realize strong microwave absorption are tailoring the impedance matching and dielectric loss properties of carbon materials [12]. The good impedance matching of carbon materials with air, which includes surface and internal impedance matching, promotes the transmission and scattering of microwaves within carbon materials [13,14], leading to effective microwave capture. The dielectric loss that occurs in carbon materials is a critical property for the conversion of microwave to heat or other forms of energy, thus affecting their microwave absorption properties [15]. The dielectric loss comprises conductive and polarization losses, which are related to the electrical conductivity and defective molecular structures, respectively [6]. Although a high conductive loss allows microwave absorption, excessive conductive loss induces impedance mismatches, resulting in the reflection of microwaves at the surfaces of the absorber, thus reducing microwave absorption [16]. To ensure effective microwave absorption, polarization loss should be high [17]. Overall, it is necessary to balance the trade-offs between impedance matching, conductive loss, and increasing polarization loss in carbon materials to achieve strong microwave absorption.

A promising approach to balance the trade-off between impedance matching and the conductive loss of carbon materials is the rational design of their porous structures [18]. The fabrication of porous structures within carbon materials is effective for impedance matching to the impedance of free air; this is because the introduction of abundant air-filled cavities results in the impedance of the structure approaching that of air [19]. Furthermore, tailoring the porous structures of carbon materials can moderate their conductive loss by decreasing their electrical

conductivity owing to scattered electron conduction pathways [17]. Thus, the rational design of porous structures within carbon materials is of great significance for tailoring both the impedance matching and conductive loss properties, which cannot be achieved effectively by their denser counterparts. For example, Liu et al. recently manipulated conventional organic-polymer-derived dense carbon to produce a random porous carbon aerogel to balance impedance matching and excessive conductive loss; the researchers realized a high microwave absorption of -61.7 dB at 11.1 GHz [20]. Despite this development, there is still a demand for the further improvement of porous structures in carbon materials to achieve stronger microwave absorptions.

While the design of porous structures can tailor impedance matching and conductive loss properties, defect engineering of carbon-based molecular structures is effective in increasing the polarization loss and moderating conductive loss, thereby enhancing the microwave absorption performance [21]. To achieve such defective carbon structures, doping with heteroatoms such as N and O has become a major approach [22]. For example, N-doped defective carbons have been prepared by the post-treatment of carbon materials with reagents such as ammonia [23] and amines [24]. Chitin (β-(1→4)-linked N-acetyl anhydroglucosamine), which is one of the most abundant and renewable biopolymers on earth, intrinsically contains N and O, providing the opportunity to dope N and O atoms to prepare defective carbon structures by simple carbonization. Recently, the carbonization of crab-shell-derived chitin nanofibrous aerogel has been reported [25], providing a facile and sustainable way to fabricate porous and N- and O-doped defective carbon structures. Although chitin nanofiber-derived carbon honeycombs have been applied in energy storage [25], electrocatalysts [26], and photosensing [27], their potential properties and applicability in microwave absorption have not yet been explored. Notably, it remains challenging to optimize all complex functions, i.e., impedance matching with air, conductive loss, and polarization loss, in a single carbon material to achieve strong microwave absorption.

To meet this demand, herein, the design of chitin nanofiber-derived carbon honeycombs with tailored porous structures and defective carbon structures is proposed as a rational strategy. Honeycomb-like anisotropic porous channels were fabricated by the unidirectional freeze drying of chitin nanofiber/water suspensions, followed by temperature-controlled carbonization to tailor defective carbon structures. We found that these materials have good impedance matching and moderate conductive loss, thereby affording much stronger microwave absorption than that of random porous structures. The N- and O-doped defective carbon structures were tailored to provide the highest polarization loss and moderate conductive loss.

The resulting carbon honeycomb had strong microwave absorption when the incident microwave radiation was parallel or perpendicular to the anisotropic channels. This study may provide new insight into the structural and functional design of carbon honeycombs for strong microwave absorption.

1.2 Experimental section

1.2.1 Materials

An aqueous suspension of chitin nanofibers obtained from crab shells was purchased from Sugino Machine, Ltd. (BiNFi-s chitin, SFo-20002, Toyama, Japan). Acrylic plates were purchased from Acrysunday Co., Ltd. (Osaka, Japan). Cu foil (No. 8701-00) was supplied by Maxell Sliontec Ltd. (Kanagawa, Japan). A hydrophilic polytetrafluoroethylene (PTFE) membrane filter (H020A090C, 0.2 μm pore diameter) was purchased from Advantec Toyo Kaisha, Ltd. (Tokyo, Japan).

1.2.2 Fabrication of chitin nanofiber-derived carbon honeycombs

Anisotropic chitin nanofiber-derived carbon honeycombs were fabricated via unidirectional freeze drying and subsequent carbonization. Briefly, chitin nanofiber/water suspension (1.0 wt%, 24 mL) was first defoamed by centrifugal vacuum for 5 min at room temperature (ARV-930TWIN, Thinky Corp., Tokyo, Japan) and then poured into an acrylic box (40 mm width×30 mm length ×20 mm depth), where an inner wall was pre-attached to a Cu foil (**Fig. 1-1**). The unidirectional ice-templating process was performed by attaching the sample mold (with the Cu side) to a cubic open steel box containing liquid N_2. After the chitin nanofiber suspension was fully frozen, the unidirectional frozen sample was freeze dried (EYELA FDU-2200, Tokyo Rikakikai Co., Ltd., Tokyo, Japan) for approximately 60 h to produce the anisotropic chitin honeycomb. Finally, the as-prepared chitin nanofiber-derived honeycomb was carbonized in a temperature-programmable muffle furnace (KDF75, Denken-Highdental Co., Ltd., Kyoto, Japan) under N_2 gas with a flow rate of 0.5 L min^{-1}. The samples were carbonized in three stages: (1) increase in temperature from room temperature to 500 °C at a rate of 2 °C min^{-1} and holding for 2 h; (2) increase in the temperature to 700, 800, or 900 °C at a rate of 5 °C min^{-1} and holding for 1 h; (3) cooling down to room temperature at a rate of 2 °C min^{-1}.

In addition, aerogels with random porous structures were fabricated by the direct freeze-drying method. After the chitin nanofiber suspension was added to the acrylic box, the box was gently immersed in liquid N_2 until the suspension was fully frozen. Thereafter, the frozen sample was freeze dried for approximately 60 h to produce a chitin honeycomb with random porous structures. Finally, carbon honeycomb was obtained using the same carbonization

procedure as that used for the anisotropic carbon honeycomb.

Chitin nanofiber-derived carbon nanofibrous papers with dense structures were obtained using an aqueous suspension of chitin nanofibers (0.2 wt%, 200 mL) that was dewatered on a PTFE membrane filter under vacuum filtration. The resulting chitin nanofibrous film was then peeled off the PTFE filter and immersed in liquid N_2 until fully frozen, followed by freeze drying to prepare the paper. Carbonization was performed under the same conditions as that used for the anisotropic carbon honeycomb.

1.2.3 Microwave absorption measurements

The as-prepared aerogels and papers were cut into waveguide samples with a length of 10.5 mm, width of 23.5 mm, and a thickness less than 9.7 mm. The electromagnetic parameters including permittivity (ε' and ε'') and permeability (μ' and μ'') of the samples were measured using a vector network analyzer (E5071C, Agilent Technologies, Inc., California, USA) with a WR-90 X-band waveguide test chamber (KeyCom Corp, Tokyo, Japan). The microwave absorption performance evaluated by the reflection loss (*RL*) was calculated based on the transmission line theory using the following equations (Eqs. 1.1–1.2) [28,29]:

$$RL(dB) = 20log\left|\frac{Z_{in}-1}{Z_{in}+1}\right| \quad (1.1)$$

$$Z_{in} = \sqrt{\frac{\mu_r}{\varepsilon_r}}tanh\left[j\left(\frac{2\pi fd}{c}\right)\sqrt{\mu_r\varepsilon_r}\right] \quad (1.2)$$

where Z_{in} represents the input characteristic impedance, j is the imaginary unit, ε_r and μ_r are the complex permittivity ($\varepsilon_r=\varepsilon'+j\varepsilon''$) and permeability ($\mu_r=\mu'+j\mu''$) of the absorber, respectively, f (GHz) is the frequency, d (m) is the thickness of the carbon honeycomb, and c is the velocity of light in free space (3×10^8 m s^{-1}).

1.2.4 Evaluation of impedance matching, conductive loss, and polarization loss

Based on Z_{in}, the impedance matching performance ($|Z_{in}/Z_0|$) was evaluated by calculating the ratio of Z_{in} to Z_0, where Z_0 represents the impedance of free space [16]. A Z_{in} closer to Z_0 implies good impedance matching, where the incident wave can entirely enter the absorber. The conductive and polarization loss (ε''_c and ε''_p, respectively) were calculated according to the following equations (Eqs. 1.3–1.4) [6]:

$$\varepsilon_c'' = \frac{\sigma}{2\pi f\varepsilon_0} \quad (1.3)$$

$$\varepsilon_p'' = \varepsilon'' - \varepsilon_c'' \quad (1.4)$$

where ε_0 represents the vacuum dielectric constant (8.854×10^{-12} F m^{-1}) and σ (S m^{-1}) represents the electrical conductivity of the carbon honeycomb measured by a four-probe resistivity meter (Loresta-GP, MCP-T610, Mitsubishi Chemical Analytech Co., Ltd, Tokyo, Japan).

1.2.5 Characterization

FE-SEM was used to observe the anisotropic morphology of the carbon honeycombs at an accelerate voltage of 2 kV (SU-8000, Hitachi High-Tech Science Corp., Tokyo, Japan). Platinum sputtering of the samples was performed before FE-SEM observation. TEM observation was operated at 200 kV (JEM-ARM200F, JEOL, Ltd., Tokyo, Japan). XRD patterns were recorded with an Ultima IV X-ray diffractometer (Rigaku Corp., Tokyo, Japan) using Cu Kα radiation (1.5418 Å) at 30 kV and 40 mA. Raman spectra were recorded with a laser wavelength of 532 nm (RAMAN-touch VISNIR-OUN, Nanophoton Corp., Osaka, Japan). Elemental analysis was performed using an organic trace element analysis device (JM10, J-Science Lab Co., Ltd., Kyoto, Japan). XPS spectra were recorded with a JPS-9010 photoelectron spectrometer (JEOL Ltd, Tokyo, Japan) using monochromatic Al Ka (1486.6 eV) radiation as the excitation source. The electrical conductivities of the samples were analyzed by a four-probe resistivity meter (Loresta-GP, MCP-T610, Mitsubishi Chemical Analytech Co., Ltd., Tokyo, Japan).

1.3 Results and discussion

1.3.1 Anisotropic porous channels of the honeycomb

Crab-shell-derived chitin nanofiber was used as a building unit to fabricate anisotropic porous channels (**Fig. 1-1**). An aqueous chitin nanofiber suspension (1.0 wt%) was first defoamed; this was followed by unidirectional ice templating and freeze drying [30], and subsequent carbonization at different temperatures. Owing to the unidirectional temperature gradient, the ice crystals grew vertically on the surface of the Cu foil side-by-side. The adjacent ice crystals promoted the assembly of chitin nanofibers as a continuous thin layer to form the anisotropic porous channel walls. After eliminating the ice crystals by freeze drying, a chitin honeycomb with an anisotropic porous channel was formed. Although the original chitin honeycomb shrank after carbonization, the carbonized chitin honeycomb was free-standing, enabling easy tailoring of its shape for the desired application (**Fig. 1-2**).

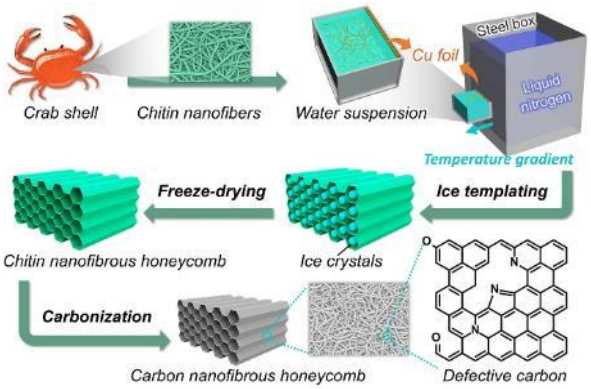


Fig. 1-1 Schematic of preparation process for anisotropic chitin nanofiber-derived carbon honeycomb by unidirectional freeze drying and subsequent carbonization.

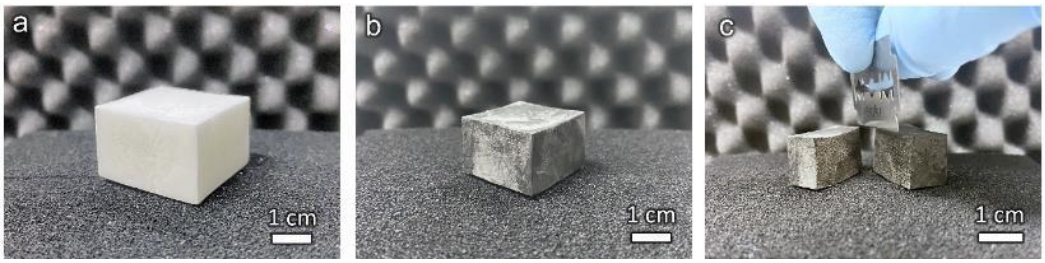


Fig. 1-2 Photographs of chitin nanofiber-derived honeycomb (a) before and (b) after carbonization at 800 °C, and (c) post carbonization sample in (b) after cutting.

As shown in **Fig. 1-3a, b**, a laser pen was used to irradiate the chitin honeycomb in the parallel and perpendicular directions to the anisotropic porous channels. Light transmission through the honeycomb was observed in the parallel direction but not in the perpendicular direction, indicating that the anisotropic porous channels had formed successfully.

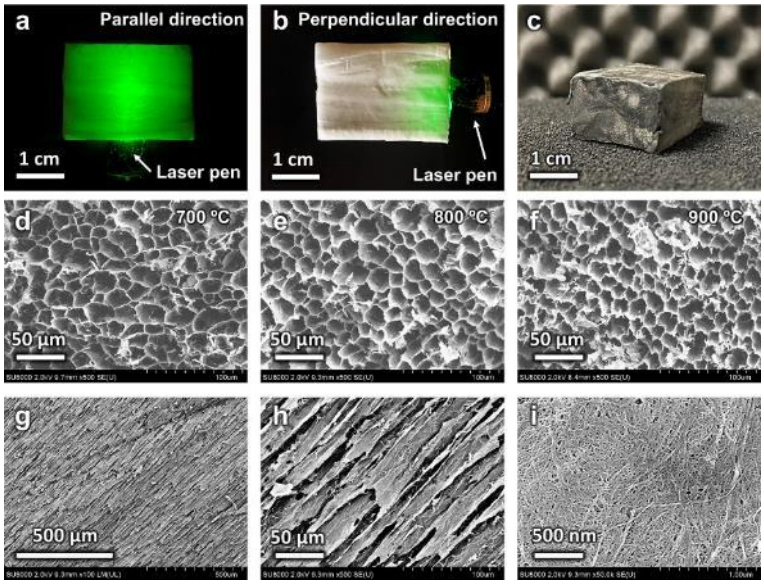


Fig. 1-3 Anisotropic honeycomb-like porous channels of chitin nanofiber-derived carbon honeycombs. Photographs of laser-penetration tests in (a) parallel and (b) perpendicular directions for chitin honeycomb, and (c) carbonized chitin honeycomb. FE-SEM images in parallel direction of honeycomb carbonized at (d) 700 °C, (e) 800 °C, and (f) 900 °C. (g-i) FE-SEM images in perpendicular direction of honeycomb carbonization at 800 °C.

Field-emission scanning electron microscopy (FE-SEM) observation of the chitin honeycomb in both directions verified that the honeycomb comprised adjacent honeycomb-like porous structures with straight channels (**Fig. 1-4**). Notably, the chitin honeycomb maintained its original cubic shape even after carbonization (Fig. 1-3c). FE-SEM analysis was performed to demonstrate the successful preservation of the anisotropic honeycomb-like porous structures in the resulting honeycomb (Fig. 1-3d-i). All the as-prepared carbon honeycombs had honeycomb-like porous structures with thin channel walls (Fig. 1-3d-f). The size of the honeycomb-like pores decreased slightly as the carbonization temperature increased from 700 °C to 900 °C, indicating an increase in shrinkage at higher temperatures [27]. In addition, highly ordered straight channels were clearly observed from the side view of the honeycomb (Fig. 1-3g and h), where a thin channel wall was formed by the

interconnected carbonized chitin nanofibers (Fig. 1-3i).

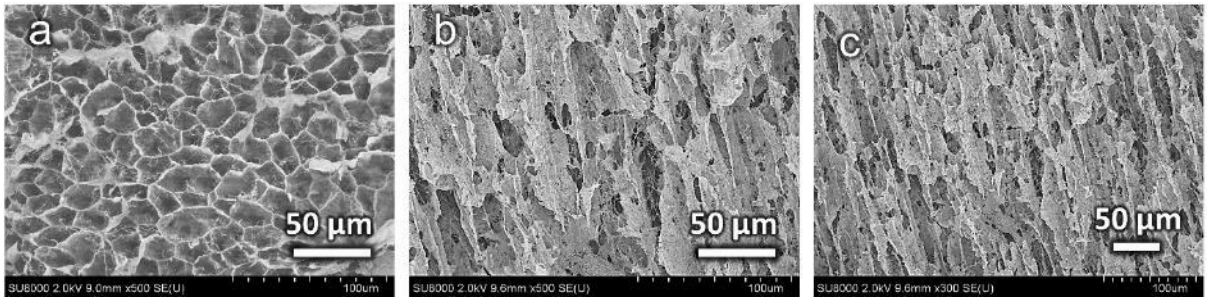


Fig. 1-4 SEM images of original chitin honeycomb with anisotropic porous channels observed in (a) parallel and (b and c) perpendicular directions to anisotropic porous channels.

In comparison, the nonunidirectional freeze-dried chitin nanofiber-derived-carbon honeycomb was composed of thin kinked layers and random porous structures (**Fig. 1-5**). These results indicate that unidirectional freeze drying enabled the formation of anisotropic honeycomb-like porous structures. Therefore, chitin nanofiber-derived carbon honeycombs with tailored anisotropic porous channels were successfully fabricated.

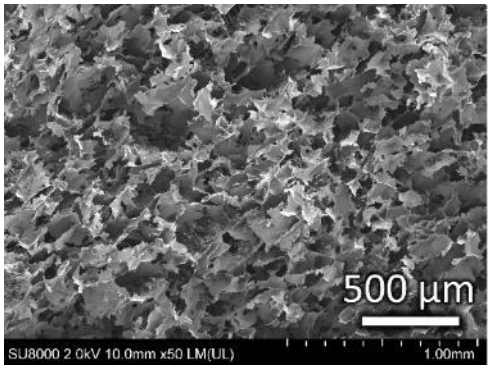


Fig. 1-5 SEM images of chitin honeycomb carbonized at 800 °C with random porous structures.

1.3.2 Anisotropic porous channels for optimizing microwave absorption

Fig. 1-6a-c illustrates the three distinct morphologies of the chitin nanofiber-derived carbon materials (anisotropic porous channels, random porous structures, and dense structures), which were prepared to investigate the potential of the anisotropic porous channels with regard to balancing the impedance matching and conductive loss of the honeycombs for effective microwave absorption. Impedance matching values closer to one imply that the input impedance of the absorber is close to that of air, which indicates nearly zero reflection of the incident microwave at the sample interfaces. This provides the highest possibility of the incident microwave being captured by the absorber [20]. The impedance matching performance of the anisotropic porous honeycomb, which was measured in the parallel direction to the anisotropic channels, was the closest to one at a thickness of 7.22 mm compared with that of other samples (Fig. 1-6d). Thus, the nearly full capture of the incident microwaves at 8.9 GHz could be achieved for carbon honeycombs tailored by anisotropic porous channels with an impedance-matched thickness (t_m) of 7.22 mm.

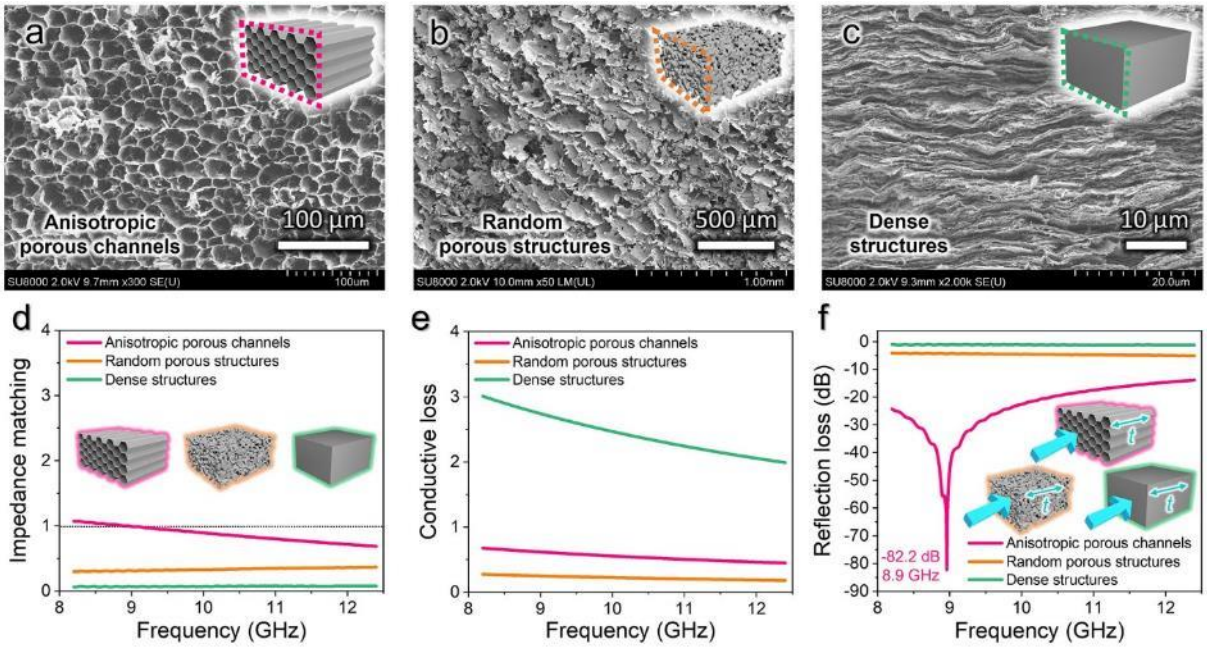


Fig. 1-6 Anisotropic porous channels for optimizing microwave absorption performance of chitin honeycomb carbonized at 800 °C. FE-SEM images of (a) anisotropic porous channels, (b) random porous structures, and (c) dense structures in chitin nanofibrous paper carbonized at 800 °C. (d) Impedance matching performance, (e) conductive loss, and (f) reflection loss of the chitin honeycomb with anisotropic or random porous structures, and the chitin nanofibrous paper with dense structures carbonized at 800 °C measured in the parallel direction. Thickness (*t*) of each sample: 7.22 mm.

The honeycomb with anisotropic porous channels had moderate conductive loss compared with that of the random porous and dense structures (Fig. 1-6e), which can be beneficial for absorbing the captured microwave. The dense carbon nanofibrous paper had the highest electrical conductivity of 1.37 S m^{-1} (**Fig. 1-7**) because its electron conduction pathways are compact, resulting in a poor impedance matching performance due to its excessive conductive loss (Fig. 1-6d and e). The honeycomb with the random porous structure had a significantly lower electrical conductivity of 0.13 S m^{-1} and conductive loss, because the electron conduction pathways would be drastically scattered. The honeycomb with anisotropic porous channels had

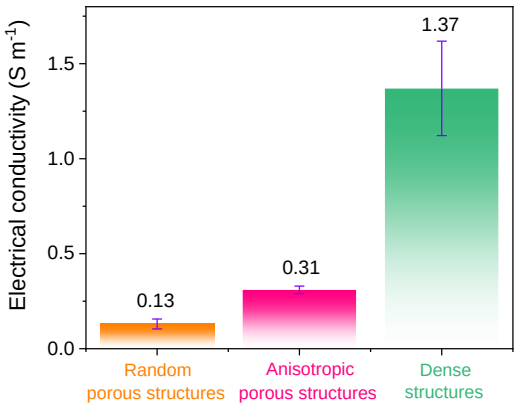


Fig. 1-7 Electrical conductivity of chitin honeycomb with random porous structure, anisotropic porous channels, and dense chitin nanofibrous paper carbonized at 800 °C.

moderate electrical conductivity of 0.31 S m^{-1} and conductive loss, possibly due to the formation of adequately scattered electron conduction pathways along with the thin walls of honeycomb-like channels. Consequently, the random porous chitin nanofiber-derived carbon honeycomb and dense carbon nanofibrous paper had poor microwave absorption intensities (less than -5.0 dB) (Fig. 1-6f). An enhanced microwave absorption performance of -82.2 dB at 8.9 GHz was obtained for the anisotropic porous chitin nanofiber-derived carbon honeycomb, which confirms its optimal impedance matching, conductive loss, and microwave absorption performance. Notably, the anisotropic porous chitin nanofiber-derived carbon honeycomb afforded effective microwave absorption intensities less than -10 dB over the entire X-band (8.0-12 GHz), which is used for various purposes such as radar, satellite communication, and wireless computer networks [31]. Moreover, benefiting from the anisotropic porous structures of this honeycomb, the best impedance matching region was tailored from low frequency to high frequency when the incident microwave radiates from the parallel to perpendicular direction (**Fig. 1-8a**) of the anisotropic porous channels. In the perpendicular direction, the anisotropic porous channel endows the carbon honeycomb with optimal conductive loss properties (Fig. 1-8b), optimal microwave absorption of -92.8 dB at 11.6 GHz, and a t_m of 6.61 mm (Fig. 1-8c). Such anisotropic microwave absorption performance originates from the optimal microstructure of this honeycomb, which enables balanced impedance matching and conductive loss performance, in addition to anisotropic permittivity due to the anisotropic porous channels (see **Fig. 1-9** for more details).

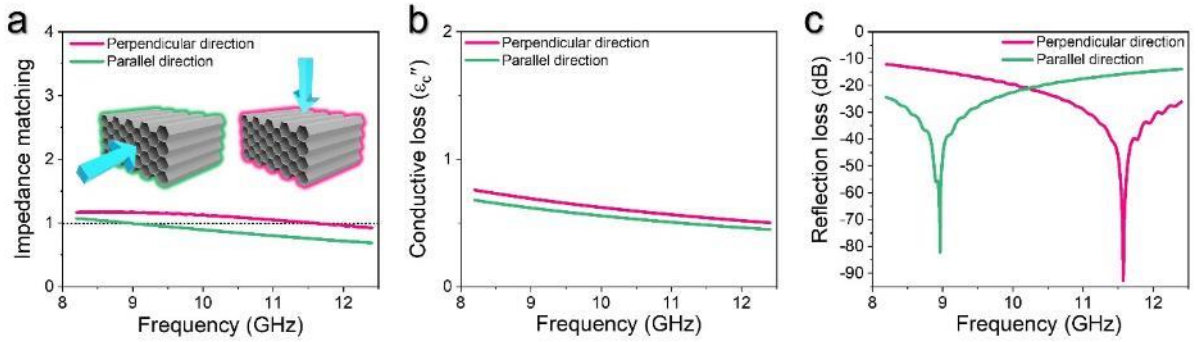


Fig. 1-8 (a) Impedance matching performance, (b) conductive loss, and (c) reflection loss of anisotropic chitin honeycombs carbonized at 800 °C measured in perpendicular (6.61 mm) and parallel (7.22 mm) directions.

According to the quarter-wavelength model, the impedance-matched frequency (f_m) at a specific thickness (t_m) is determined by the quarter-wavelength [32] of the incident microwaves in the absorber, as expressed by the following equation (Eq. 1.5):

$$f_m = \frac{nc}{4t_m\sqrt{|\mu_r\varepsilon_r|}} \quad (n=1, 3, 5\ldots\ldots) \tag{1.5}$$

where c is the velocity of light in free space (3×10^8 m s^{-1}), and ε_r and μ_r are the relatively complex permittivity and permeability, respectively.

Carbon honeycombs are all-dielectric materials without magnetic properties, where μ_r is typically considered to be one. The above equation can be defined as (Eq. 1.6)

$$f_m = \frac{nc}{4t_m\sqrt{|\varepsilon_r|}} \quad (n=1, 3, 5\ldots\ldots) \tag{1.6}$$

Thus, it is concluded that the microwave absorption frequency is determined by the thickness and permittivity of the absorber. The frequency decreases with an increase in the thickness and permittivity.

For the anisotropic microwave absorption phenomenon observed in the chitin honeycomb carbonized at 800 °C (Fig. 1-8), the quarter-wavelength model was studied according to Eqs. 1.5-1.6 (**Fig. 1-9**). The absorption frequency of the honeycombs at a specific thickness was determined by the quarter-wavelength of the incident microwaves, where the strongest absorption frequency decreased with increasing thickness and permittivity [32]. The honeycomb carbonized at 800 °C had a dielectric permittivity of approximately 2.2 when a strong microwave absorption peak was observed at 8.9 GHz with the incident microwaves parallel to the anisotropic porous channels (Fig. 1-9a). A permittivity value of approximately 1.7 with a strong microwave absorption peak occurring at 11.6 GHz was obtained after measurement in the perpendicular direction (Fig. 1-9b). The permittivity values of the honeycomb carbonized at 800 °C and evaluated in the parallel direction were larger than those in the perpendicular direction, and t_m in the parallel direction (7.22 mm) was larger than that in the perpendicular direction (6.61 mm). Because the impedance-matched frequency (f_m) is inversely proportional to permittivity and t_m, f_m in the parallel direction was lower than that in the perpendicular direction.

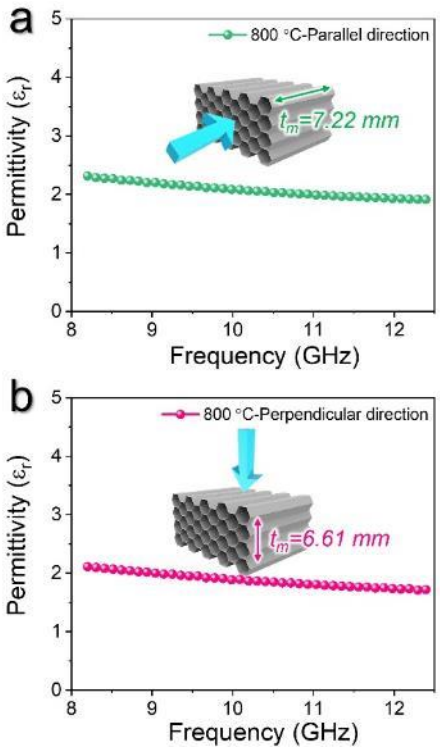


Fig. 1-9 Permittivity values for anisotropic chitin nanofiber-derived carbon honeycombs carbonized at 800 °C and measured in (a) parallel and (b) perpendicular directions.

1.3.3 Defective carbon structures of the honeycomb

To tailor the defective carbon structures, anisotropic chitin nanofiber-derived carbon

honeycombs were prepared at different carbonization temperatures (700-900 °C) and then evaluated using X-ray diffraction (XRD), Raman spectroscopy, and transmission electron microscopy (TEM). The XRD patterns of all the honeycombs had two small and broad diffraction peaks centered at $2\theta \approx 24.0°$ and 44.0° (**Fig. 1-10a**), which were assigned to the crystalline reflections (002) and the (10) band of graphite, respectively [33]. The (10) band originates from the smearing of intralayer orientation of the random graphitic carbon fragments and is eventually supposed to evolve into the (100) and the (101) peaks of graphite [34]. Although these two peaks were small, their intensity was slightly increasing with increasing carbonization temperatures, suggesting the formation of small graphitic carbon fragments. The downward drifting, i.e., high background intensity, of the XRD curves indicated that all the honeycombs contain a proportion of amorphous carbons [35]. Raman spectroscopy was performed to confirm the formation of graphitic carbon structures in the as-prepared carbon honeycombs. The characteristic G-band at ~1590 cm^{-1} and the D-band at ~1360 cm^{-1} indicate the presence of graphitic and defective carbon structures in the honeycombs, respectively [25,36] (Fig. 1-10b). The intensity ratio of D- and G-band peaks (I_D/I_G) increased with increasing carbonization temperature, suggesting that abundant structural defects can be formed at these carbonization temperatures [37]. These results were consistent with those of the XRD analyses.

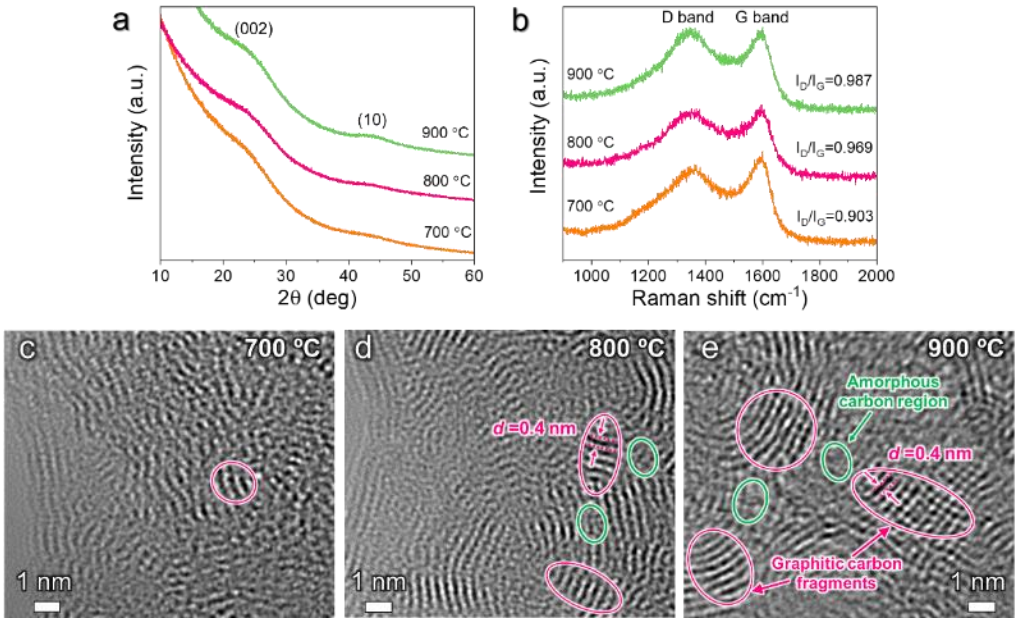


Fig. 1-10 Defective carbon structures of chitin nanofiber-derived carbon honeycombs. (a) XRD patterns and (b) Raman spectra of samples carbonized at different temperatures. High-resolution TEM images of honeycombs carbonized at (c) 700 °C, (d) 800 °C, and (e) 900 °C. Pink and green circles represent the graphitic carbon fragment and amorphous carbon region, respectively.

The detailed structures of the fabricated honeycombs were further revealed using TEM analysis. Nanofibrous structures were observed in all the carbonized samples in the low-resolution TEM images (**Fig. 1-11**), showing good correspondence with the thin honeycomb-like channel walls shown in Fig. 1-3i. The high-resolution TEM images show the amorphous and graphitic carbon structures of the carbonized honeycombs (Fig. 1-10c-e). For the honeycomb carbonized at 700 °C, fewer and smaller graphitic carbon fragments were observed than those observed for the honeycomb carbonized at 800 °C and 900 °C. The lattice fringes obtained from the honeycomb carbonized at 800 °C were parallel, with a *d*-spacing of 0.4 nm, demonstrating the formation of small graphitic carbon fragments[34]. Each fringe represents a single-layer graphitic carbon layer. Amorphous carbon regions were also observed between the small graphitic carbon fragments. Furthermore, the carbon honeycomb (900 °C) had larger graphitic carbon fragments (Fig. 1-10e) than those of the honeycomb carbonized at 800 °C, with well-resolved crystal lattice fringes, suggesting that the further growth of the graphitic crystals occurred with carbonization at higher temperature [38,39].

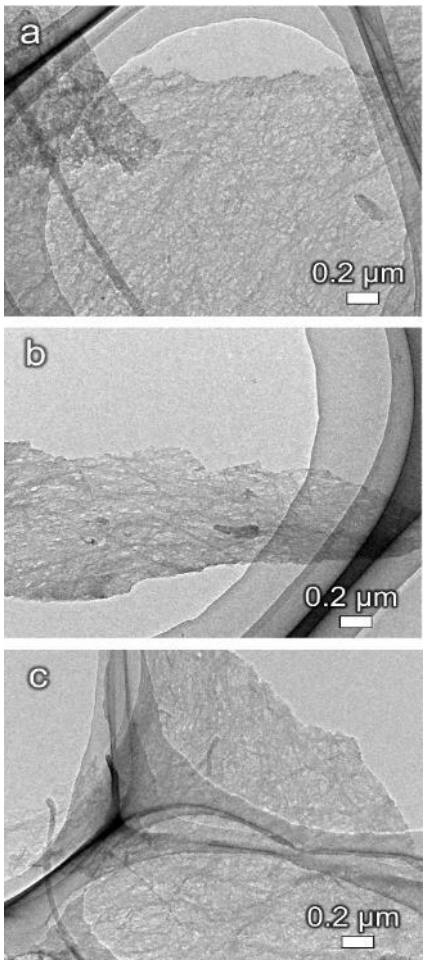


Fig. 1-11 Low-magnification TEM images of honeycomb-like channel walls of chitin nanofiber honeycombs carbonized at (a) 700 °C, (b) 800 °C, and (c) 900 °C.

Elemental and X-ray photoelectron spectroscopy (XPS) analyses were performed to study the chemical composition and molecular structure of the honeycombs. The elemental analyses suggested that the honeycomb contained C, O, N, and H. The C content in the carbonized chitin honeycomb increased from ~76.7 to ~82.3 wt% with increasing carbonization temperature, indicating that O, N, and H were gradually removed from the honeycomb during carbonization (**Fig. 1-12a**).

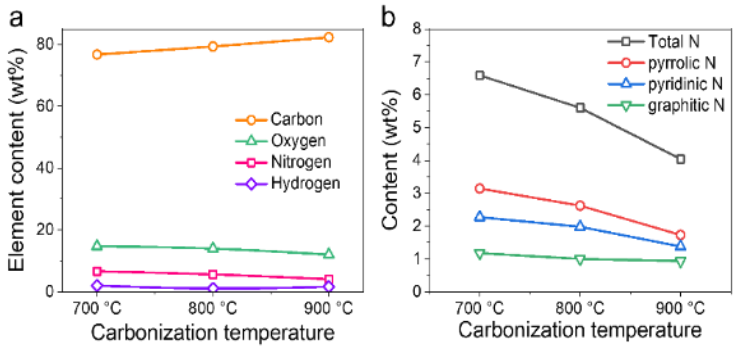


Fig. 1-12 (a) Elemental content of chitin nanofiber honeycombs as a function of carbonization temperature. (b) Normalized N content of the honeycombs carbonized at different carbonization temperature.

The N content of the honeycombs carbonized at 700, 800, and 900 °C were 6.59, 5.60, and 4.04 wt%, respectively. In **Fig. 1-13a**, the XPS wide surveys confirmed the presence of C, N, and O in the honeycombs with characteristic peaks at 285, 399, and 532 eV, respectively [40], verifying *in situ* N- and O-doping of the honeycombs. More bonding information was obtained from the narrow scans. The C 1s peak was deconvoluted into four peaks: C-C (284.2 eV), C-N (285.0 eV), C-O (285.7 eV), and C=O (288.3 eV) [41] (Fig. 1-13b). Among the N atoms, three peaks related to pyridinic N (398.4 eV), pyrrolic N (399.9 eV), and graphitic N (401.0 eV) [22,27] were identified (Fig. 1-13c). The pyrrolic N, pyridinic N, and graphitic N contents of the carbonized honeycombs were estimated from the area ratio of each peak and the total N content (Fig. 1-12a). With increasing carbonization temperatures from 700 to 900 °C, the pyrrolic N, pyridinic N, and graphitic N contents were gradually decreased from 3.14 to 1.72 wt%, from 2.27% to 1.37 wt%, and from 1.17 to 0.94 wt%, respectively (Fig. 1-12b). Based on the above structural and elemental analyses, we speculated the molecular structures of the honeycombs carbonized at different temperatures (Fig. 1-13d-f). While further analyses are required to clarify their molecular structures, these results suggest that the O-, N-doped features were partially maintained after high temperature carbonization, thus enabling the generation of defective carbon structures.

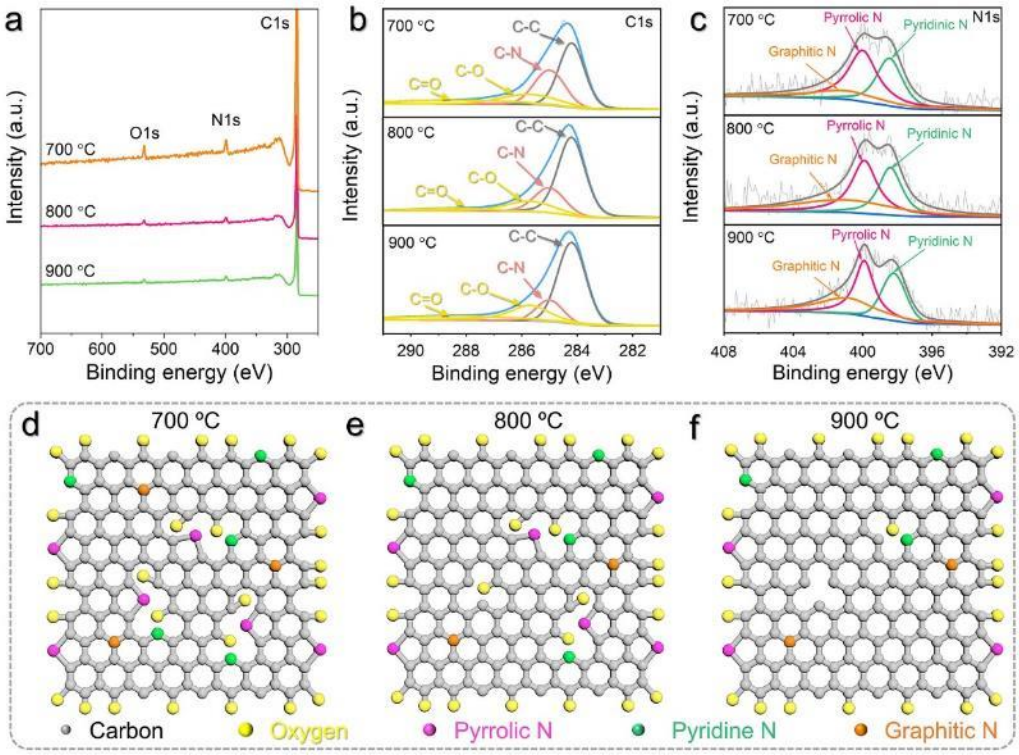


Fig. 1-13 Molecular structures of chitin nanofiber-derived carbon honeycombs. (a) Wide XPS spectra, (b) C 1s XPS spectra, (c) N 1s XPS spectra. Speculated molecular structures of honeycombs carbonized at (d) 700 °C, (e) 800 °C, and (f) 900 °C.

1.3.4 Defective carbon structures for promoting microwave absorption

To elucidate the effect of the defective carbon structures on the microwave absorption capacity of the anisotropic chitin nanofiber-derived carbon honeycombs, the polarization loss performance was examined as a function of the carbonization temperature. **Fig. 1-14a** shows that the honeycomb carbonized at 800 °C had higher polarization loss values than those carbonized at 700 °C and 900 °C, suggesting that the defective carbon structures formed at 800 °C can enhance the microwave absorption performance.

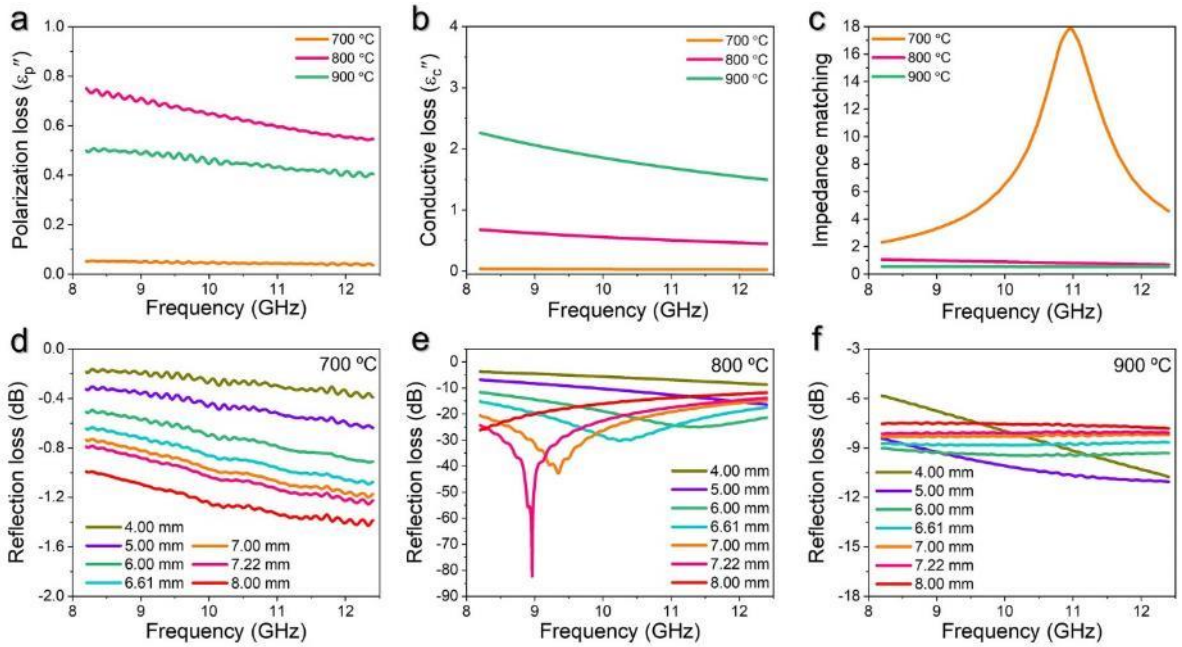


Fig. 1-14 Defect-dominated microwave absorption properties of the anisotropic chitin honeycombs carbonized at different temperatures. (a) Polarization loss, (b) conductive loss, and (c) impedance matching of honeycombs with incident microwave in parallel direction. Microwave absorption performance of honeycombs with different thicknesses carbonized at (d) 700 °C, (e) 800 °C, and (f) 900 °C measured in parallel direction.

To explain the polarization loss phenomenon, the relative complex permittivity of the carbonized honeycombs was measured in the X-band (8.2-12.4 GHz). The real (ε′) and imaginary (ε″) permittivity values of the carbonized honeycombs gradually decreased with increasing the frequency (**Fig. 1-15a-b**), indicating the typical dielectric polarization behavior [42]. The classic Debye relaxation analyses suggested that the honeycomb carbonized at 800 °C offer abundant dielectric polarization processes than the other carbonized samples, which are originating from dipole polarization relaxations in the vacancy defects and heteroatom-doping centers of the defective carbon structures [21] as well as interfacial polarization occurring at the heterointerfaces between graphitic carbon fragments and amorphous carbon regions [6,43] (Fig.

1-10d). Based on the above speculated molecular structure models (Fig. 1-13d-f), the polarization loss mechanisms for the honeycombs carbonized at different temperatures can be explained as follows. Abundant N- and O-doping and low graphitic carbon structures were formed in the honeycomb carbonized at 700 °C (Fig. 1-13d). It is difficult to induce and polarize dipoles between C and heteroatoms because of the low graphitic carbon structures. Although the honeycomb carbonized at 900 °C afforded the growth of graphitic carbon structures, it decreased the doped heteroatoms significantly (Fig. 1-13f), resulting in low dipole polarization. The honeycomb carbonized at 800 °C achieved the highest polarization loss, owing to its dipole polarization by balancing the growth of graphitic carbon structures and doping of heteroatoms (Fig. 1-13e), and its interfacial polarization by providing the heterointerfaces between graphitic carbon fragments and amorphous carbon regions [6,43] (Fig. 1-10d).

The real (ε′) and imaginary (ε″) permittivity values of the carbonized honeycombs gradually decreased with increasing the frequency (**Fig. 1-15a-b**), indicating the typical dielectric polarization behavior [42]. Based on the classical Debye relaxation theory, the relaxation process was analyzed using Cole–Cole semicircles [44], which were calculated by the following equations (Eqs. 1.7–1.9):

$$\varepsilon_r = \varepsilon' - j\varepsilon'' = \varepsilon_\infty + \frac{\varepsilon_S - \varepsilon_\infty}{1 + j2\pi f\tau} \quad (1.7)$$

$$\varepsilon' = \varepsilon_\infty + \frac{\varepsilon_S - \varepsilon_\infty}{1 + (j2\pi f\tau)^2} \quad (1.8)$$

$$\varepsilon'' = \frac{\omega\tau_0(\varepsilon_S - \varepsilon_\infty)}{1 + (j2\pi f\tau)^2} \quad (1.9)$$

where, j, f, τ, ε_S, and ε_∞ are the imaginary unit, frequency (GHz), relaxation time (s), static dielectric constant, and dielectric constant at an infinite frequency, respectively. Equations 1.8 and 1.9 were derived from Eq. 1.7, and the relationship between ε' and ε'' [45] was further deduced from Equations S4 and S5 (Eq. 1.10).

$$\left(\varepsilon' - \frac{\varepsilon_S + \varepsilon_\infty}{2}\right)^2 + (\varepsilon'')^2 = \left(\frac{\varepsilon_S - \varepsilon_\infty}{2}\right)^2 \quad (1.10)$$

From Eq. 1.10, the curves of ε′ and ε″ form a single semicircle, each of which contributes to one Debye relaxation process [12].

To clarify the enhancement in the polarization loss of the honeycomb carbonized at 800 °C, the classic Debye relaxation represented by Cole–Cole semicircles was performed. Usually, one Cole–Cole semicircle represents one polarization process [44]. The curves of the honeycomb carbonized at 800 °C had more Cole–Cole semicircles than the other carbonized samples (Fig. 1-15c-e), indicating abundant polarization processes in the former. These polarization loss processes originate from dipole polarization relaxations in the vacancy defects and heteroatom-

doping centers of the carbon-based molecular structures [21] (Fig. 1-13a). In addition, the distorted Cole–Cole semicircles were assigned to the Debye-like relaxation processes, such as interfacial polarization occurring at the hierarchical interfaces between graphitic carbon fragments and defective sites, which further enhance polarization loss [45].

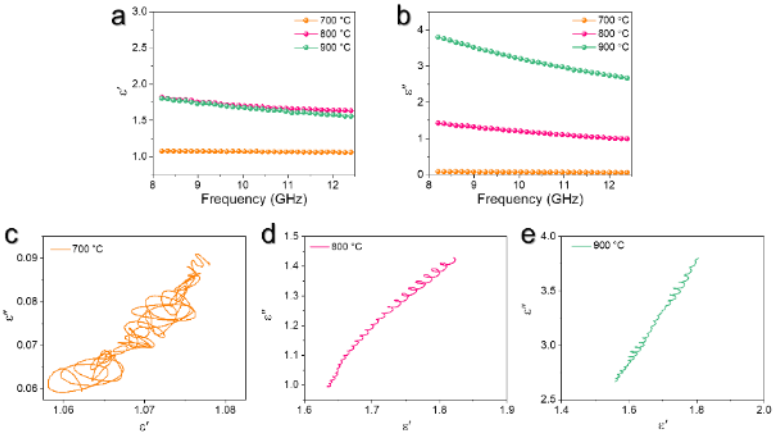


Fig. 1-15 (a) Real (ε′) and (b) imaginary (ε″) permittivity of the honeycomb carbonized at 700 °C, 800 °C, and 900 °C. Debye relaxation represented by Cole–Cole semicircles for chitin honeycombs carbonized at (c) 700 °C, (d) 800 °C, and (e) 900 °C.

Such defect engineering is also preferred to moderate the conductive loss performance of carbon honeycombs. Fig. 1-14b shows that moderate conductive loss was realized by the honeycomb carbonized at 800 °C, while that carbonized at 900 °C had a higher conductive loss because the heteroatoms were removed, and the more graphitic carbon structures were formed (Fig. 1-10e). It can be deduced that conductive loss instead of polarization loss is dominant for the sample carbonized at the higher temperature, which is negative for the impedance matching performance (Fig. 1-14c) and is triggered by the carbonization-dominant electrical conductivity (**Fig. 1-16**).

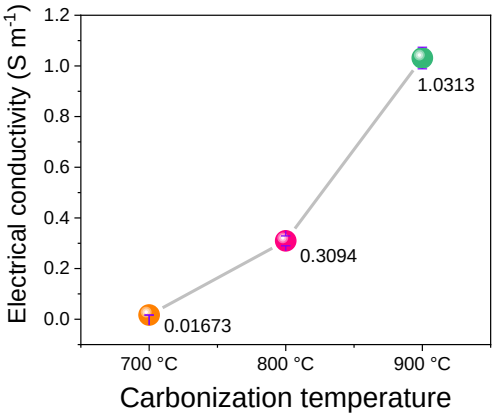


Fig. 1-16 Electrical conductivity of the chitin nanofiber-derived carbon honeycombs carbonized at 700 °C, 800 °C, and 900 °C measured in the parallel direction to the anisotropic porous channels.

By the combination of the highest polarization loss and moderate conductive loss, the anisotropic honeycomb carbonized at 800 °C can provide stronger microwave absorption performances than the honeycomb carbonized at 700 °C and 900 °C. Fig. 1-14d-f shows the reflection loss values that are calculated based on the transmission line theory. Although the honeycomb carbonized at 700 °C had abundant defective structures, the impedance matching performance (Fig. 1-14c) and conductive loss were poor (Fig. 1-14b) due to poor electrical conductivity (Fig. 1-16), making it a poor absorber of the incident microwave radiation, giving the minimum reflection loss value of -1.5 dB at 12.4 GHz at a thickness of 8.0 mm (Fig. 1-14d). The microwave absorption performance of the honeycomb carbonized at 900 °C was improved

with a minimum reflection loss value of -11.1 dB at 12.4 GHz at a thickness of 5.0 mm (Fig. 1-14f). However, it was difficult for the honeycomb carbonized at 900 °C to achieve strong microwave absorption due to the impedance mismatch (Fig. 1-14c) caused by the excessive conductive loss (Fig. 1-14b), and low polarization loss performance (Fig. 1-14a) caused by the excessive loss of heteroatoms. On the contrary, strong microwave absorption with a minimum reflection loss value of -82.2 dB at 8.9 GHz at a thickness of 7.22 mm was achieved by the honeycomb carbonized at 800 °C (Fig. 1-14e), due to its the highest polarization loss (Fig. 1-14a), moderate conductive loss (Fig. 1-14b), and excellent impedance matching (Fig. 1-14c). The honeycomb carbonized at 800 °C allowed stronger microwave absorption than the other carbonized samples with incident microwave even in perpendicular direction; a minimum reflection loss of -92.8 dB was realized at a frequency of 11.6 GHz and a thickness of 6.61 mm (**Fig. 1-17**).

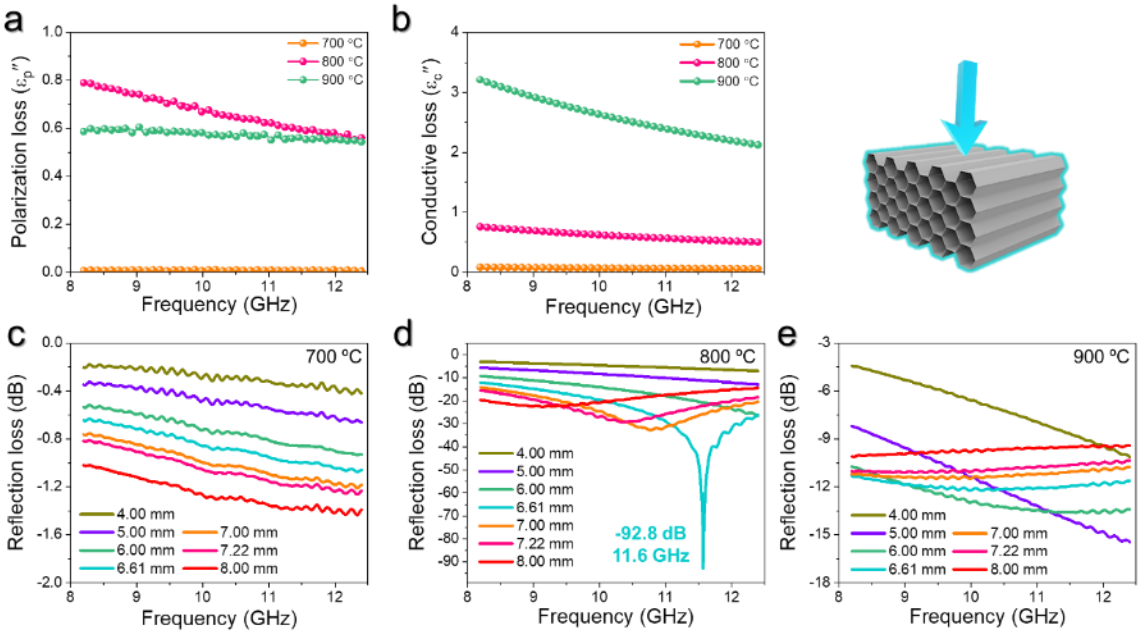


Fig. 1-17 (a) Polarization loss, (b) conductive loss, and microwave absorption performance of anisotropic carbon honeycombs carbonized at (c) 700 °C, (d) 800 °C, and (e) 900 °C and measured with the incident microwave in the perpendicular direction.

In the direction perpendicular to the anisotropic porous channels, the microwave absorption performances of the chitin honeycombs carbonized at 700 °C or 900 °C were the same as those in the parallel direction (**Fig. 1-17c and e**). This results from the imbalanced impedance matching and conductive loss performance. Furthermore, the polarization loss of the honeycomb carbonized at 700 °C was too low to polarize the induced electrons. For the honeycomb carbonized at 900 °C, the polarization loss was also weak due to the loss of

heteroatoms and the enhanced graphitic carbon structures formed at high temperature.

Owing to the same carbon-based molecular structure, both in the parallel and perpendicular direction of the honeycomb carbonized at 800 °C, the perpendicular direction had similar good impedance matching, moderate conductive loss, and higher polarization loss properties to the parallel direction. As a result, a strong microwave absorption was also achieved with a minimum RL of -92.8 dB at a thickness of 6.61 mm in the perpendicular direction to the anisotropic porous channels (**Fig. 1-17d**). In addition, for a thickness above 6.0 mm, the effective absorption bandwidth (frequency range for RL values below -10 dB) [8] in both the parallel and perpendicular directions cover the entire applied X-band frequency; in this case, more than 90.0% of the incident microwave can be attenuated by the absorber.

1.3.5 Putative mechanism of strong microwave absorption by the honeycomb with anisotropic porous channels and defective carbon structures

As described above, the anisotropic porous channels allow for the effective microwave capture by balancing the trade-off between impedance matching with air and conductive loss, while the defective carbon structures achieve effective absorption of the captured microwave by providing high polarization loss (i.e., interfacial and dipole polarization) and moderate conductive loss. The detailed mechanism of the observed anisotropic and strong microwave absorption by the honeycombs is summarized as follows. First, the best impedance matching both in the parallel and perpendicular directions allows for effective microwave capture by enhancing the transmission and scattering of microwaves within the developed honeycomb with tailored anisotropic porous channels (**Fig. 1-18a**). Second, the tailored honeycomb-like porous channels provide anisotropic in-plane and out-of-plane permittivity with scattered electron conduction pathways across their thin walls, giving a moderate and highly efficient conductive loss capability for capturing and absorbing microwaves both in the parallel and perpendicular directions (Fig. 1-18b), where the microwave energy can effectively transform into heat or other forms of energy and dissipate [46]. Third, the tailored defective carbon structures allow for effective microwave absorption by increasing polarization loss, which also contributes to the dissipation of microwave. The increasing polarization loss is generated by the interfacial polarization at the heterointerfaces between graphitic carbon fragments and amorphous carbon regions [6,43] (Fig. 1-18c), as well as the dipole polarization by the tailored N- and O-doping [21] (Fig. 1-18d). The N- and O-doped carbon structures (i.e., N-C and O-C bonding) can facilitate the accumulation of dipoles between N or O, which has relatively high electronegativity than C, and adjacent C under alternating microwave field [47,48], leading to the effective microwave absorption by increasing polarization loss. Thus, the honeycomb with the tailored anisotropic

porous channels and defective carbon structures achieves excellent impedance matching, moderate conductive loss, and high polarization loss, thereby affording anisotropic and strong microwave absorption performances. Our honeycomb had superior microwave absorption ability to state-of-the-art carbon-based absorbers, such as nanocarbon [42], nanocarbon-based composites [49,50,51], carbon/metal composites [52,53], carbonized synthetic polymer [20], and biomass-derived carbons (such as waxberry- [54], shaddock peel- [55], wheat straw- [56], wheat flour- [57], lignocellulosic nanofiber- [58], cotton- [59], and wood-derived carbons [60]) (**Table 1**), suggesting that our strategy is promising to realize strong microwave absorption.

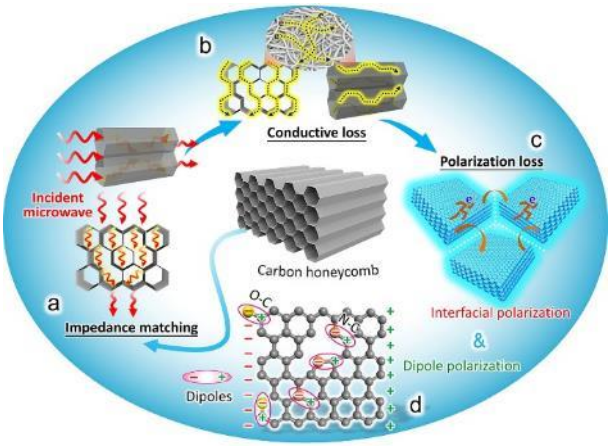


Fig. 1-18 Possible mechanism of strong microwave absorption for the chitin nanofiber-derived carbon honeycomb with the tailored anisotropic porous channels and defective carbon structures.

Table 1-1 Typical carbon-based microwave absorbers and their X-band absorption performance.

Sample name	Minimum reflection loss [dB]	Absorption bandwidth [GHz][a)]	Refs.
Graphene/carbon nanotube aerogel	-15.1	4.2	49
Carbonized waxberry	-16.0	4.2	54
Carbon nanotubes film	-24.58	~2.1	42
Cellulose nanofibers/carbon nanotubes aerogel	-27.0	4.2	50
Shaddock-peel-based carbon aerogel	-29.5	~2.4	55
Wheat-straw-derived carbon foam	-37.0	3.9	56
MXene/polyimide-based carbon aerogel	-45.4	4.2	51
FeCo/C-wood carbon aerogel	-47.6	~3.2	52
Graphite-like carbon/CeO_2 aerogel	-50.36	3.83	53
Wheat-flour-derived nanocarbon	-51.0	~2.8	57
Lignocellulosic-nanofiber-derived graphitic carbon	-51.0	4.2	58
Cotton-derived carbon/Co@carbon	-60.0	~1.8	59
Synthetic-polymer-derived carbon aerogel	-61.7	~3.2	20
Wood-based porous carbon	-68.3	4.2	60
Chitin nanofiber-derived carbon honeycomb	-92.8	4.2	**This work**

[a)] Absorption bandwidth: the frequency range for effective microwave absorption (the minimum reflection loss values less than -10 dB).

1.4 Conclusion

The tailoring of anisotropic porous and defective carbon structures of chitin nanofiber-derived carbon honeycombs was demonstrated as a rational approach to optimize the complex functions, i.e., impedance matching with air, conductive loss, and polarization loss, in a single carbon material, promoting strong microwave absorption. The anisotropic porous channels were tailored by the unidirectional freeze drying of chitin nanofiber/water suspensions to provide good impedance matching with air, and moderate conductive loss. Furthermore, N- and O-doped defective carbon structures, which were optimized after temperature-controlled carbonization, can provide high polarization loss and moderate conductive loss. The as-tailored chitin nanofiber-derived honeycomb, carbonized at 800 °C, had a stronger microwave absorption of -92.8 dB than state-of-the-art carbon-based microwave absorbers, such as the wood-based porous carbon of -68.3 dB. As chitin is one of the most abundant and renewable bioresources on Earth, these findings indicate a new avenue for the development of high-performance and sustainable microwave absorption materials. This strategy also provides a good opportunity for the versatile functional design of bio-nanofiber-derived carbon materials for diverse applications.

1.5 References

1 F. Shahzad, M. Alhabeb, C. B. Hatter, B. Anasori, S. M. Hong, C. M. Koo and Y. Gogotsi, *Science*, 2016, **353**, 1137–1140.

2 G. Wang, Y. Zhao, Y. Zhang, M. Zhou and G. Ji, *Nano-Micro Lett.*, 2022, **14**, 1–14.

3 W. Yang, J. Sun, W. Fu, Y. Dong, Y. Fu and Y. Zhu, *Carbon*, 2022, **194**, 114–126.

4 F. Wang, W. Gu, J. Chen, Y. Wu, M. Zhou, S. Tang, X. Cao, P. Zhang and G. Ji, *Nano Res.*, 2022, **15**, 3720–3728.

5 C. Li, X. Qi, X. Gong, Y. Chen, R. Xie and W. Zhong, *Nano Res.*, 2022, 15, 6761–6771.

6 X. X. Wang, B. Wen, W. Q. Cao and M. S. Cao, *Carbon*, 2021, **184**, 136–145.

7 I. V. Anoshkin, J. Campion, D. V. Lioubtchenko and J. Oberhammer, *ACS Appl. Mater. Interfaces*, 2018, **10**, 19806–19811.

8 G. Gou, F. Meng, H. Wang, W. Wei and Z. Zhou, *Nano Res.*, 2019, **12**, 1423–1429.

9 Y. Zhang, Y. Huang, T. Zhang, H. Chang, P. Xiao, H. Chen, Z. Huang and Y. Chen, *Adv. Mater.*, 2015, **27**, 2049–2053.

10 Y. Zhao, L. Hao, S. Tan, H. Li, J. Zheng and G. Ji, *Small Sci.*, 2022, **2**, 2100077.

11 A. Iqbal, F. Shahzad, K. Hantanasirisakul, M. K. Kim, J. Kwon, J. Hong, H. Kim, D. Kim, Y. Gogotsi and C. M. Koo, *Science*, 2020, **369**, 446–450.

12 M. Qin, L. Zhang and H. Wu, *Adv. Sci.*, 2022, **9**, 2105553.
13 Z. Jiang, H. Si, X. Chen, H. Liu, L. Zhang, Y. Zhang, C. Gong and J. Zhang, *Compos. Commun.*, 2020, **22**, 100503.
14 W. Yang, X. Yang, Y. Dong, Y. Zhu and Y. Fu, *Appl. Surf. Sci.*, 2021, **564**, 150437.
15 X. Li, L. Yu, Y. Dong, Y. Zhu, Y. Fu and F. Fu, *Chem. Eng. J.*, 2020, **379**, 122393.
16 T. Wang, G. Chen, L. Zhang and H. Wu, *J. Colloid Interface Sci.*, 2021, **595**, 1–5.
17 X. Li, X. Yin, C. Song, M. Han, H. Xu, W. Duan, L. Cheng and L. Zhang, *Adv. Funct. Mater.*, 2018, **28**, 1803938.
18 H. Zhao, Y. Cheng, W. Liu, L. Yang, B. Zhang, L. P. Wang, G. Ji and Z. J. Xu, *Nano-Micro Lett.*, 2019, **11**, 1–17.
19 M. Qin, L. Zhang, X. Zhao and H. Wu, *Adv. Funct. Mater.*, 2021, **31**, 2103436.
20 P. Liu, S. Gao, F. Zhou, Z. Meng, Y. Huang and Y. Wang, *Carbon*, 2020, **169**, 276–287.
21 M. Qin, L. Zhang, X. Zhao and H. Wu, *Adv. Sci.*, 2021, **8**, 2004640.
22 C. Hu and L. Dai, *Adv. Mater.*, 2019, **31**, 1804672.
23 D. Hulicova-Jurcakova, M. Kodama, S. Shiraishi, H. Hatori, Z. H. Zhu and G. Q. Lu, *Adv. Funct. Mater.*, 2009, **19**, 1800–1809.
24 Z. Xu, Y. Du, D. Liu, Y. Wang, W. Ma, Y. Wang, P. Xu and X. Han, *ACS Appl. Mater. Interfaces*, 2019, **11**, 4268–4277.
25 B. Ding, S. Huang, Y. Duan and J. Zhang, *ACS Sustain. Chem. Eng.*, 2018, **6**, 177–185.
26 M. Borghei, J. Lehtonen, L. Liu and O. J. Rojas, *Adv. Mater.*, 2018, **30**, 1703691.
27 L. Zhu, Y. Huang, Y. Morishita, K. Uetani, M. Nogi and H. Koga, *J. Mater. Chem. C*, 2021, **9**, 4444–4452.
28 S. S. Kim, S. B. Jo, K. I. Gueon, K. K. Choi, J. M. Kim and K. S. Churn, *IEEE Trans. Magn.*, 1991, **27**, 5462–5464.
29 X. Li, L. Yu, L. Yu, Y. Dong, Y. Zhu and Y. Fu, *Chem. Eng. J.*, 2018, **352**, 745–755.
30 Z. Chen, H. Zhuo, Y. Hu, H. Lai, L. Liu, L. Zhong and X. Peng, *Adv. Funct. Mater.*, 2020, **30**, 1910292.
31 J. B. Kim, S. K. Lee and C. G. Kim, *Compos. Sci. Technol.*, 2008, **68**, 2909–2916.
32 J. Zhou, F. Guo, J. Luo, G. Hao, G. Liu, Y. Hu, G. Zhang, H. Guo, H. Zhou and W. Jiang, *J. Mater. Chem. C*, 2022, **10**, 1470–1478.
33 J. Biscoe and B. E. Warren, *J. Appl. Phys.*, 1942, **13**, 364–371.
34 K. Tanaka, M. Ueda, T. Koike, T. Yamabe and S. Yata, *Synth. Met.*, 1988, **25**, 265–275.
35 L. Lu, V. Sahajwalla, C. Kong and D. Harris, *Carbon*, 2001, **39**, 1821–1833.
36 L. Bokobza, J. L. Bruneel and M. Couzi, *Chem. Phys. Lett.*, 2013, **590**, 153–159.

37 M. S. Cao, X. X. Wang, W. Q. Cao and J. Yuan, *Adv. Mater.*, 2020, **32**, 1907156.

38 K. Jurkiewicz, M. Pawlyta and A. Burian, *C - J. Carbon Res.*, 2018, **4**, 68.

39 H. Koga, K. Nagashima, K. Suematsu, T. Takahashi, L. Zhu, D. Fukushima, Y. Huang, R. Nakagawa, J. Liu, K. Uetani, M. Nogi, T. Yanagida and Y. Nishina, *ACS Nano*.

40 L. Gao, D. Ying, T. Shen, Y. Zheng, J. Cai, D. Wang and L. Zhang, *ACS Sustain. Chem. Eng.*, 2020, **8**, 10881–10891.

41 R. Hao, Y. Yang, D. Yu, L. Guo and S. Yang, *Nano Energy*, 2018, **45**, 220–228.

42 H. Sun, R. Che, Yang, J. Deng, L. Qiu and H. Peng, *Adv. Mater.*, 2014, **26**, 8120–8125.

43 W. Liu, S. Tan, Z. Yang and G. Ji, *Carbon*, 2018, **138**, 143–153.

44 X. Yan, X. Huang, Y. Chen, Y. Liu, L. Xia, T. Zhang, H. Lin, D. Jia, B. Zhong, G. Wen and Y. Zhou, *Carbon*, 2021, **174**, 662–672.

45 H. Wang, F. Meng, F. Huang, C. Jing, Y. Li, W. Wei and Z. Zhou, *ACS Appl. Mater. Interfaces*, 2019, **11**, 12142–12153.

46 H. Lv, Z. Yang, B. Liu, G. Wu, Z. Lou, B. Fei and R. Wu, *Nat. Commun.*, 2021, **12**, 834.

47 F. Wang, W. Gu, G. Wang and G. Ji, *J. Mater. Sci. Technol.*, 2022, **105**, 92–100.

48 Z. Zhang, G. H. Wang, W. Gu, Y. Zhao, S. Tang and G. Ji, *J. Colloid Interface Sci.*, 2022, **605**, 193–203.

49 Q. Zhang, Z. Du, M. Hou, Z. Ding, X. Huang, A. Chen, Y. Ma, S. Lu and X. Z. Tang, *Carbon*, 2022, **188**, 442–452.

50 H. Xu, X. Yin, M. Li, X. Li, X. Li, X. Dang, L. Zhang and L. Cheng, *ACS Appl. Mater. Interfaces*, 2019, **11**, 22628–22636.

51 J. Liu, H. Bin Zhang, X. Xie, Y. Liu and Z. Z. Yu, *Small*, 2018, **14**, 1802479.

52 Y. Xiong, L. Xu, C. Yang, Q. Sun and X. Xu, *J. Mater. Chem. A*, 2020, **8**, 18863–18871.

53 S. Gao, G. S. Wang, L. Guo and S. H. Yu, *Small*, 2020, **16**, 1906668.

54 X. Sun, M. Yang, S. Yang, S. Wang, W. Yin, R. Che and Y. Li, *Small*, 2019, **15**, 1902974.

55 W. Gu, J. Sheng, Q. Huang, J. Chen and G. Ji, *Nano-Micro Lett.*, 2021, **13**, 1–14.

56 M. A. Aslam, W. Ding, S. ur Rehman, A. Hassan, Y. Bian, Q. Liu and Z. Sheng, *Appl. Surf. Sci.*, 2021, **543**, 148785.

57 H. Zhao, H. Lv, G. Ji and Y. Du, *ACS Sustain. Chem. Eng.*, 2018, **6**, 15850–15857.

58 Z. Lou, Q. Wang, U. I. Kara, R. S. Mamtani, X. Zhou, H. Bian, Z. Yang, Y. Li, H. Lv, S. Adera and X. Wang, *Nano-Micro Lett.*, 2022, **14**, 1–16.

59 H. Zhao, Y. Cheng, J. Ma, G. Ji and Y. Du, *Chem. Eng. J.*, 2018, **339**, 432–441.

60 J. Xi, E. Zhou, Y. Liu, W. Gao, J. Ying, and C. Gao, *Carbon*, 2017, **124**, 492–498.

Chapter 2. Frequency-tunable and absorption/transmission-switchable microwave absorber based on a chitin-nanofiber-derived elastic carbon honeycomb

2.1 Introduction

Electromagnetic waves are used for wireless transmission of information [1]. Excessive use of electromagnetic waves can interfere with the operation of precision instruments and induce adverse effects on human health [2]. Microwave absorbers have been intensively developed to reduce electromagnetic pollution [3]. Because the frequency range of electromagnetic waves used for wireless communication is expanding, it is highly desirable to develop a microwave absorber that can smartly tune its absorption frequency and absorption/transmission properties to meet the specific application requirements and/or real-time environmental changes [4]. Sufficient impedance matching between the microwave absorber and air is essential to suppress reflection and enhance absorption [5]. To switch between absorption and transmission, the dielectric loss tangent of the microwave absorber should be reportedly tuned [6] because moderate or low dielectric loss tangent can result in microwave absorption or transmission, respectively [7], while a high dielectric loss results in microwave reflection [8].

Ideally, absorption/transmission switching and frequency-tunable absorption should be reversibly achieved using a single microwave absorber. Carbon-aerogel-based microwave absorbers have attracted considerable attention owing to their light weight [9], chemical stability [10], and versatile applications [11]. As a pioneering example, switching from microwave transmission to absorption was recently reported using a carbon black nanoparticle/wood-derived lamellar carbon aerogel [6]. The carbon aerogel exhibited microwave transmission in its original state because of its low dielectric loss tangent. Owing to the elasticity of the carbon aerogel, its dielectric loss tangent could be tuned from low to moderate levels by mechanical compression, enabling a switching from transmission to absorption [6]. To the best of our knowledge, frequency-tunable absorption using a single carbon aerogel remains challenging. To overcome this challenge, the carbon aerogel should reversibly change its thickness to modulate its impedance-matched frequency according to the well-established quarter-wavelength theory [12] while retaining its moderate dielectric loss tangent. Despite such theoretical predictions, the dynamic adjustment of the thickness and dielectric loss tangent has seldom been achieved.

In our previous study, a chitin nanofiber-derived carbon honeycomb with anisotropic honeycomb-like porous channels and N- and O-doped defective carbon structures were fabricated, providing a strong microwave absorption performance owing to its good impedance

matching and moderate dielectric loss tangent [13]. In this study, the elastic properties of the chitin nanofiber-derived carbon honeycomb microwave absorber were elaborated and applied to achieve absorption-frequency tuning and further absorption/transmission switching (**Fig. 2-1**). The chitin nanofiber-derived carbon honeycomb exhibited good elasticity in the direction perpendicular to its anisotropic porous channels. Compressing the carbon honeycomb could reduce its thickness while maintaining its good impedance matching and moderate dielectric loss tangent, tuning its maximum absorption frequency in the X-band (8.2–12.4 GHz), which is used for various applications in radar, satellite communication, and wireless computer networks [14]. Further compression of the carbon honeycomb causes impedance mismatch and significantly decreases its dielectric loss tangent, switching it from microwave absorption to transmission. Such frequency-tunable and absorption/transmission-switchable feature is reversible and maintained even after 60,000 cycles of compression and recovery, proving smart and robust microwave absorption using a single carbon honeycomb.

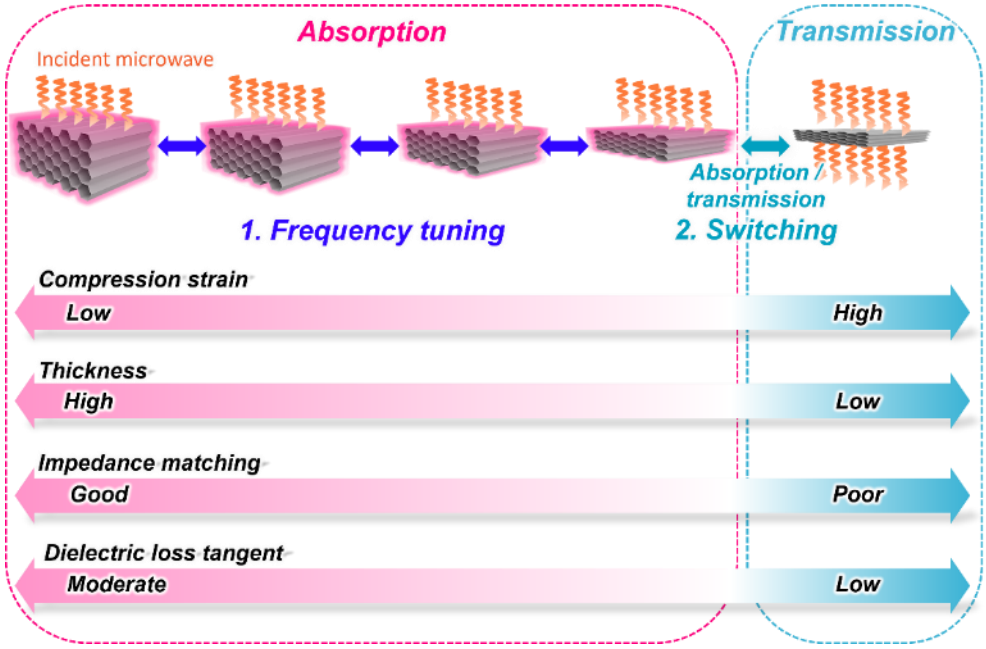


Fig. 2-1 Schematic of the strategy to tune the absorption frequency and switch from absorption to transmission of the chitin nanofiber-derived elastic carbon honeycomb with anisotropic porous channels by compressing it.

2.2 Experimental section

2.2.1 Materials

A chitin nanofiber/water suspension (BiNFi-s chitin, SFo-20002, **Fig. 2-3**) was obtained from Sugino Machine Ltd. (Toyama, Japan). Acrylic plates (thickness = 1 mm) were purchased from Acrysunday Co. Ltd. (Osaka, Japan). Conductive copper foil adhesive tape (No. 8701-00) was

purchased from Maxell Sliontec Ltd. (Kanagawa, Japan).

2.2.2 Fabrication of chitin nanofiber-derived carbon honeycomb

Chitin nanofiber-derived carbon honeycombs were prepared by unidirectional ice templating, freeze-drying, and subsequent carbonization, according to our previous report [13]. Briefly, a chitin nanofiber/water suspension (1.0 wt.%, 24 mL) was first defoamed by a centrifugal vacuum apparatus (ARV-930TWIN, Thinky Corp., Tokyo, Japan) at 1,400 rpm for 5 min at room temperature. The resulting suspension was then poured into a handmade acrylic box (40 mm width × 30 mm length × 20 mm depth), where an inner wall (40 mm width × 20 mm depth) was pre-attached using Cu foil adhesive tape. Subsequently, a chitin nanofiber/water suspension-containing acrylic box (with the Cu side) was attached to a liquid N_2-containing cubic open steel box for unidirectional ice templating. After the chitin nanofiber/water suspension was fully frozen, freeze-drying was performed for 60 h to prepare the chitin honeycomb (EYELA FDU-2200, Tokyo Rikakikai Co., Ltd., Tokyo, Japan). Finally, the obtained chitin honeycomb was carbonized under a N_2 atmosphere in a temperature-programmable muffle furnace (KDF75, Denken-Highdental Co., Ltd., Kyoto, Japan). The temperature was controlled as follows: (1) an increase from room temperature to 500 °C at a heating rate of 2 °C min^{-1} and maintained for 2 h; (2) an increase to 700, 800, or 900 °C at a heating rate of 5 °C min^{-1} and maintained for 1 h; (3) cooling at 2 °C min^{-1} to room temperature.

2.2.3 Evaluation of elastic properties of a chitin nanofiber-derived carbon honeycomb

The elastic properties of the chitin nanofiber-derived carbon honeycombs were evaluated using a compression testing equipment with a 500-N load cell (EZ-SX, Shimadzu Co., Ltd., Osaka, Japan). The cuboidal carbon honeycomb was loaded between the two compression stages and the top stage was responsible for applying the uniaxial compression force and releasing the carbon honeycomb. The loading direction was perpendicular to the anisotropic porous channels of the carbon honeycomb. All hysteresis curves with maximum strains of 20, 40, 60, and 80% were obtained at a stroke rate of 10 mm min^{-1}. For the compression fatigue resistance measurement during 60,000 cycles of 80% compression and recovery, continuous cyclic compression for the carbon honeycomb was performed with a compression frequency of 0.4 Hz by using a Desktop Model Endurance Testing Machine (DLDM111LHB, YUASA System Co., Ltd., Okayama, Japan). The stress retention was calculated as the percentage ratio of the maximum stress value in each cycle to that in the first cycle [15]. The energy loss coefficient was calculated by the percentage ratio of energy loss to the energy storage during cyclic compression, which is represented by the following equation [16]:

$$\text{Energy loss coefficient} = \frac{U''}{U'} \times 100\% \quad (2.1)$$

where U'' and U' represent the energy loss and storage in each compression cycle, respectively, which were obtained from the integral area of the stress–strain curve.

2.2.4 Evaluation of microwave absorption performance, impedance matching, and dielectric loss tangent of a chitin nanofiber-derived carbon honeycomb

The experimental setup is shown in **Fig. 2-2a**. The chitin nanofiber-derived carbon honeycombs were cut into cuboidal shapes (23.5 mm width × 10.5 mm length × 6.9 mm thickness) and set into a microwave test fixture (23.5 mm width × 10.5 mm length ×9.7 mm thickness). The thickness of the carbon honeycomb was tuned inside the test fixture through mechanical compression in the direction perpendicular to the anisotropic porous channels by sandwiching two microwave-transparent acrylic plates (**Fig. 2-2b,** 23.5 mm width × 10.5 mm length × 1.0 mm thickness). The thickness of the compressed carbon honeycomb was estimated by considering the depth of the test fixture (9.7 mm), the free space, and the thickness of the acrylic plates (1.0 mm). The electromagnetic parameters of the compressed carbon honeycomb at strains of 0, 20, 40, 60, and 80% (thickness: 6.90, 5.52, 4.14, 2.76, and 1.38 mm, respectively), including the complex dielectric permittivity (ε' and ε'') and magnetic permeability (μ' and μ'') versus frequency, were measured using a vector network analyzer (E5071C, Agilent Technologies, Inc., California, USA) with an X-band waveguide test chamber (WR-90, KeyCom Corp, Tokyo, Japan), while the incident microwave radiated from the perpendicular direction to the anisotropic porous channels of the carbon honeycomb. The microwave absorption performance was evaluated using the reflection loss (RL) values, which were calculated based on the transmission line theory using the following equations (**Equations 2.2** and **2.3**) [17,18]:

$$RL\ (dB) = 20 \log_{10} \left| \frac{Z_{in}-1}{Z_{in}+1} \right| \quad (2.2)$$

$$Z_{in} = \sqrt{\frac{\mu_r}{\varepsilon_r}} \tanh \left[j \left(\frac{2\pi f d}{c} \right) \sqrt{\mu_r \varepsilon_r} \right] \quad (2.3)$$

where Z_{in} is the input impedance, ε_r and μ_r are the dielectric permittivity ($\varepsilon_r=\varepsilon'+j\varepsilon''$) and magnetic permeability ($\mu_r=\mu'+j\mu''$) of the carbon honeycomb, respectively, j accounts for the imaginary unit, f (GHz) is the frequency of the electromagnetic wave, d (m) is the thickness of the carbon honeycomb, and c is the velocity of light (3×10^8 m s^{-1}). The RL values of the compressed carbon honeycomb were calculated at strains of 0, 20, 40, 60, and 80% (thickness: 6.90, 5.52, 4.14, 2.76, and 1.38 mm, respectively). The impedance matching values ($|Z_{in}–1|$) of

the carbon honeycomb were calculated using the modulus of Z_{in}–1 [19,20]. Dielectric loss tangent values were calculated by dividing the imaginary part to the real part of complex permittivity ($\varepsilon''/\varepsilon'$) [21].

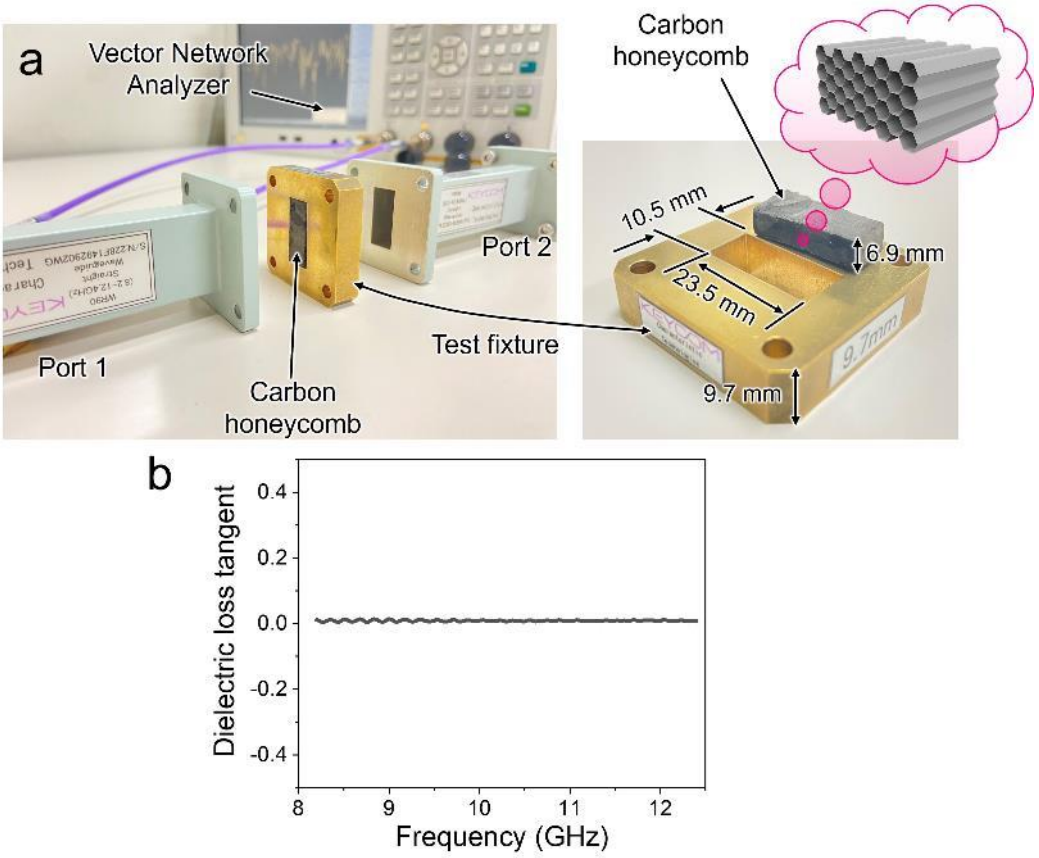


Fig. 2-2 (a) Waveguide measurement setups over the frequency range of 8.2–12.4 GHz (X-band) and (b) dielectric loss tangent of an acrylic plate.

2.2.5 Evaluation of capacitance and electrical conductivity of a chitin nanofiber-derived carbon honeycomb under AC

While the incident microwave was radiated along the direction perpendicular to the anisotropic porous channels of the carbon honeycomb, its AC capacitance and AC electrical conductivity along this direction versus frequency were calculated by the following equations (**Equations 2.4** [22] and **2.5** [23]):

$$C = \frac{\varepsilon_0 \varepsilon_r A}{d} \tag{2.4}$$

$$\sigma_{AC} = 2\pi f \varepsilon_0 \varepsilon'' \tag{2.5}$$

where C (F) is the AC capacitance, ε_0 (F m^{-1}) is the dielectric constant of vacuum, ε_r is the dielectric permittivity (ε_r=ε'+$j\varepsilon''$), A (m^2) and d (m) are the area and thickness of the carbon honeycomb, respectively, σ_{AC} (S m^{-1}) is the AC electrical conductivity, f (GHz) is the frequency

of the electromagnetic wave, and ε'' is the imaginary part of the complex dielectric permittivity of the carbon honeycomb.

2.2.6 Characterization

The morphologies of the carbon honeycombs parallel and perpendicular to their porous channels were observed by a field-emission scanning electron microscope (FE-SEM) at an acceleration voltage of 2 kV (SU-8000, Hitachi High-Tech Science Corp., Tokyo, Japan). FE-SEM images were obtained at compression strains of 0, 20, 40, 60, and 80% by compressing the carbon honeycomb between two conductive Cu foil adhesive tapes. Prior to FE-SEM observation, the carbon honeycomb was subjected to platinum sputtering at 20 mA for 10 s (ION SPUTTER, E-1045, Hitachi High-Tech Science Corp., Tokyo, Japan).

2.3 Results and discussion

2.3.1 Fabrication and elastic properties of chitin nanofiber-derived carbon honeycomb

In this study, commercial chitin nanofibers were used for the fabrication of carbon honeycombs. The nanofibrous structures of the chitin nanofibers were confirmed by FE-SEM observation (**Fig. 2-3a and b**). Molecular structures of the chitin nanofibers were analyzed by FT-IR spectroscopy (KJP-05120S, PerkinElmer Japan Co. Ltd., Kanagawa, Japan); the chitin nanofibers showed peaks at 1,660 and 1,620 cm^{-1} corresponding to the amide I region and at 1,560 cm^{-1} corresponding to the amide II region (**Fig. 2-3c**), which are the characteristic of α-chitin [24].

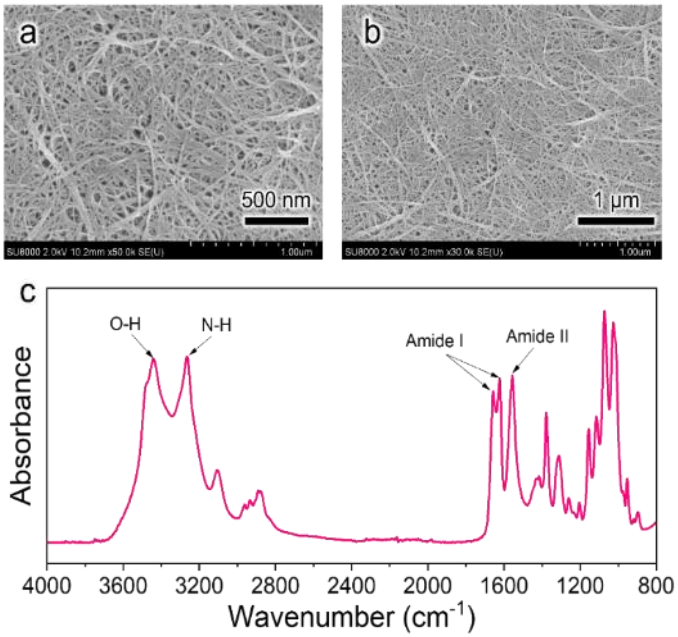


Fig. 2-3 (a, b) Field-emission scanning electron microscope (FE-SEM) images and (c) Fourier-transform infrared (FT-IR)/attenuated total reflection spectrum of the chitin nanofibers.

To realize absorption-frequency tuning and absorption/transmission switching by mechanical compression, a chitin nanofiber-derived carbon honeycomb was fabricated based on the workflow shown in **Fig. 2-4a.** Starting from the crab-shell-derived chitin nanofiber/water suspension, the carbon honeycomb was prepared *via* unidirectional ice templating, freeze-drying, and subsequent carbonization at 800 °C, according to our previous report [13]. The as-

fabricated carbon honeycomb possessed anisotropic honeycomb-like porous channels (**Fig. 2-4b-e**) with thin channel walls consisting of nanofiber networks (inset of **Fig. 2-4e**) derived from a unidirectionally grown ice template [25]. The carbon honeycomb was free-standing with a very low density (approximately 7.5 mg cm^{-3}).

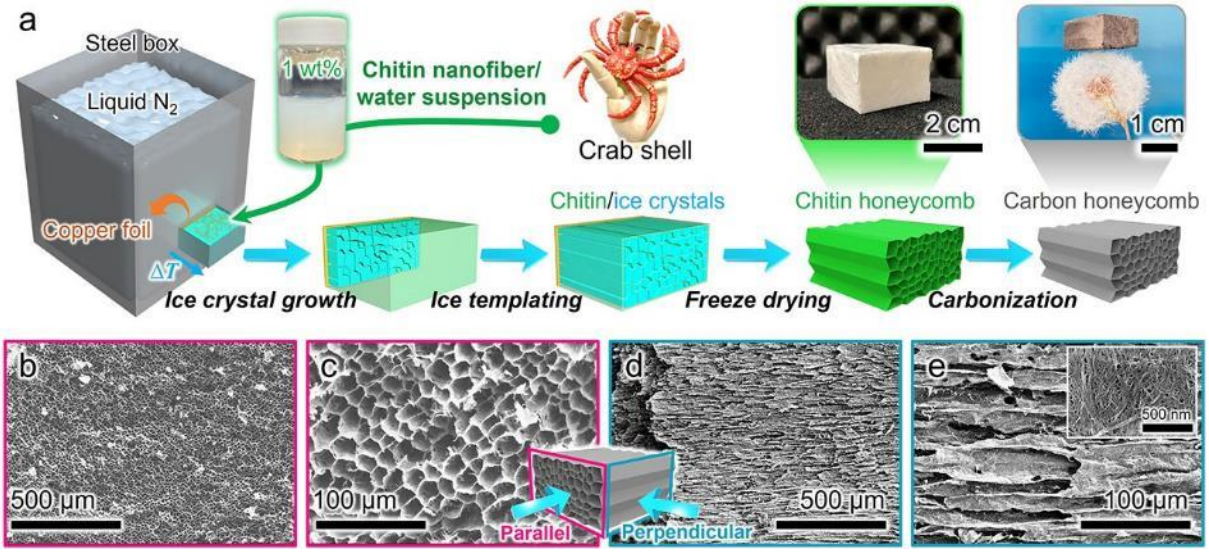


Fig. 2-4 Preparation and morphology of the chitin nanofiber-derived carbon honeycomb. (a) Schematic of the preparation. FE-SEM images of the carbon honeycomb in (b, c) parallel and (d, e) perpendicular direction of the anisotropic honeycomb-like porous channels. Carbonization temperature: 800 °C.

As shown in **Fig. 2-5a**, the carbon honeycomb could be compressed to 80% strain in the direction perpendicular to the anisotropic porous channels, and it returned to its original state after unloading. To further understand the mechanical properties of the carbon honeycomb, the stress–strain curves of the carbon honeycomb during compression loading and unloading were recorded upon successive cyclic compression at strains ranging from 0 to 20, 40, 60, and 80% (**Fig. 2-5b**). The stress–strain curves of the carbon honeycomb were consistent at each cyclic compression. At a strain of 80%, the stress was approximately 50 kPa. It remained above 0 until the strain reached 0% during the unloading process, indicating complete recovery [26]. These results indicated that the carbon honeycomb deformed elastically in the direction perpendicular to the anisotropic porous channels up to a compression strain of 80%.

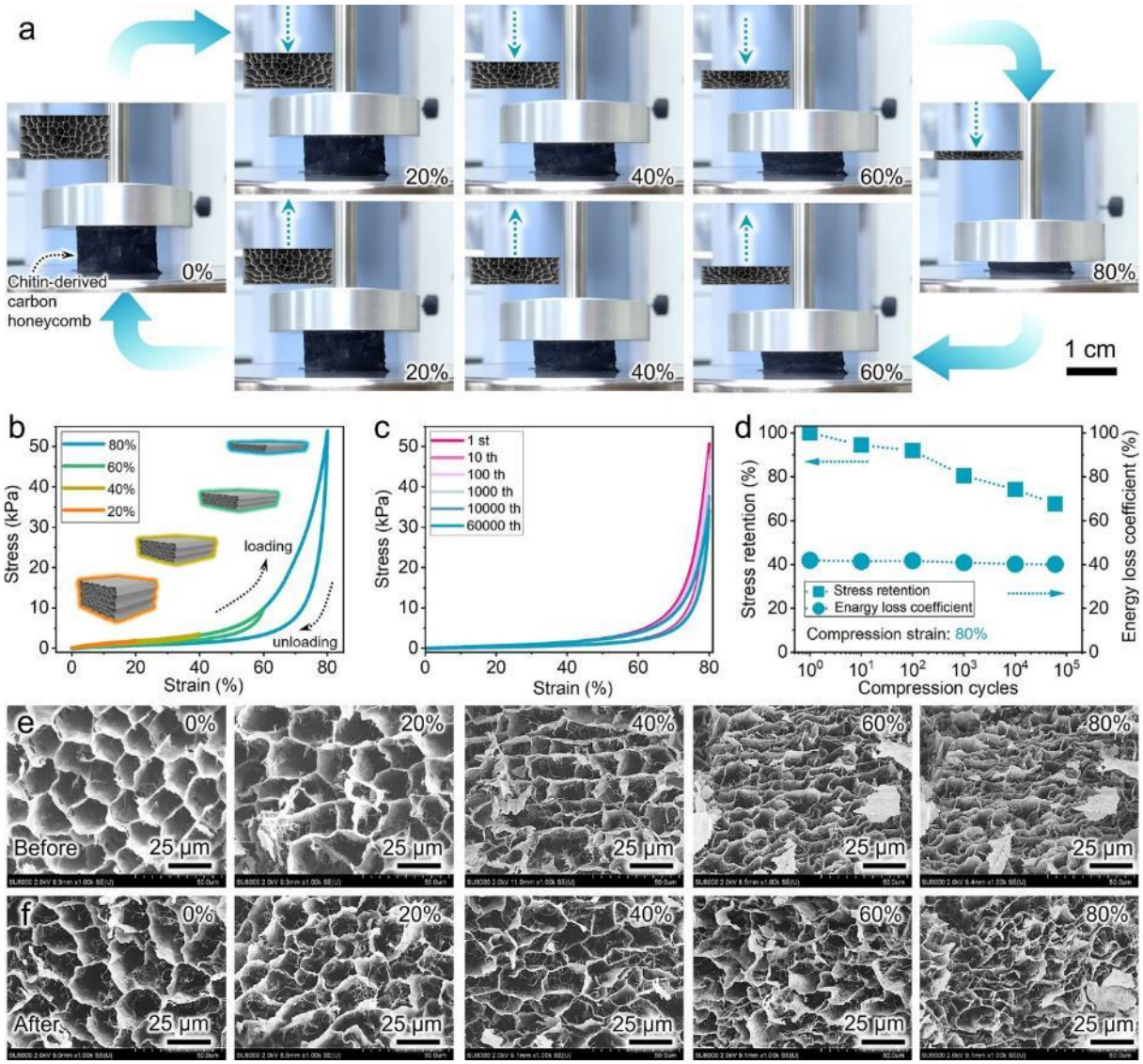


Fig. 2-5 Elastic properties and compression fatigue resistance in the direction perpendicular to the anisotropic porous channels of the chitin nanofiber-derived carbon honeycomb. (a) Optical images and (b) stress–strain curves of the carbon honeycomb during compression loading and unloading with strains of 0 to 20, 40, 60, and 80%. (c) Stress–strain curves and (d) stress retention and energy loss coefficient of the carbon honeycomb during 60,000 cycles of compression and recovery at a strain of 80%. Cross-section FE-SEM images in parallel direction of the carbon honeycomb at compression strains of 0, 20, 40, 60, and 80% (e) before and (f) after 60,000 cycles of compression and recovery at a strain of 80%. Carbonization temperature: 800 °C.

To evaluate the compression fatigue resistance, the carbon honeycomb was subjected to a cyclic compression with a loading strain of 80%. The elastic properties were maintained even after 60,000 cycles of compression and recovery (**Fig. 2-5c**). Although the compression stress

at a strain of 80% decreased to approximately 70%, its energy loss coefficient (the ratio of the energy dissipated within the material to the compression energy [27]) remained almost unchanged (**Fig. 2-5d**). These results indicated that the compression fatigue-resistance of the carbon honeycomb was sufficient for at least 60,000 cycles of compression and recovery. It has been reported that graphene [28,29] and MXene aerogels [30] with anisotropic porous channels also deform elastically upon compression perpendicular to the porous channels. In agreement with this, our chitin nanofiber-derived carbon honeycomb had an anisotropic porous channel structure (**Fig. 2-4b-e**), and it could be compressed in the direction perpendicular to that of the channels without obvious fracture at strains ranging from 20 to 80% (**Fig. 2-5e**) even after 60,000 cycles of compression and recovery at a strain of 80% (**Fig. 2-5f**).

Such elastic behavior was, however, not observed when it was compressed along the direction parallel to the anisotropic porous channels (**Fig. 2-6a**). On the other hand, the chitin honeycomb without carbonization did not deform elastically in either direction (**Fig. 2-6b and c**). The chitin nanofiber-derived carbon honeycomb collapsed its morphology upon compression in the direction parallel to the anisotropic porous channels (Fig. 2-6a). The chitin honeycomb without carbonization showed obvious plastic deformation in either compression direction, indicating no elastic properties (Fig. 2-6b and c). Thus, the carbon honeycomb was elastic only in the direction perpendicular to the anisotropic porous channels (Fig. 2-5).

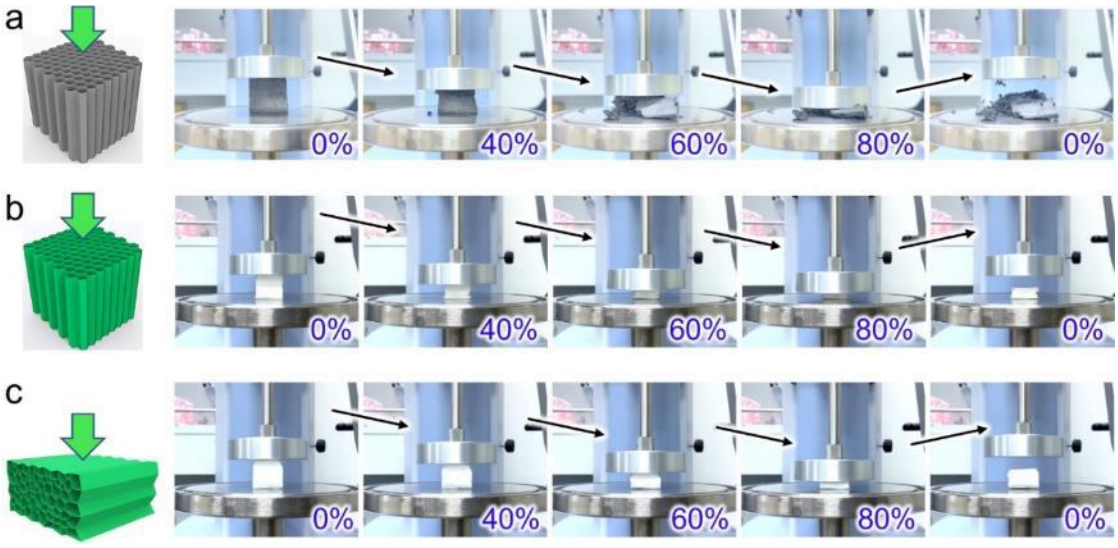


Fig. 2-6 (a) Optical images of the chitin nanofiber-derived carbon honeycomb under strain ranging from 0 to 80% during compression loading and unloading in the direction parallel to the anisotropic porous channels. Carbonization temperature: 800 °C. Optical images of the chitin honeycomb under strain ranging from 0 to 80% during compression loading and unloading in the directions (b) parallel and (c) perpendicular to the anisotropic porous channels.

2.3.2. Frequency-tunable microwave absorption by chitin nanofiber-derived elastic carbon honeycomb

The microwave absorption performance of the carbon honeycomb in the X-band (8.2−12.4 GHz) was evaluated at different compression strains in the direction perpendicular to the anisotropic porous channels while irradiating along the compression direction. As shown in **Fig. 2-7a**, the uncompressed carbon honeycomb had a minimum RL (*i.e.*, maximum microwave absorption) of approximately −40 dB at a frequency of 10.4 GHz, which was similar to those of other carbon-based elastic aerogels such as graphene and MXene aerogels reported previously (**Table 2-1**). This minimum RL could be maintained by compressing the carbon honeycomb from 0 to 20, 40, and 60% strains, with the maximum absorption frequency changing from 10.4 to 11.0, 11.5, and 12.1 GHz, respectively. Thus, the carbon honeycomb upon compression from 0 to 60% strain could achieve frequency-tunable absorption in the X-band.

Table 2-1 Typical carbon-based elastic microwave absorbers and their X-band absorption performance at a compression strain of 0%.

	Minimum reflection loss [dB]	Absorption bandwidth in the X-band [GHz][a)]	Thickness [mm]	Refs.
Graphene aerogel	−16.59	ca. 0.5	6.87	[31]
Reduced graphene oxide aerogel	−26.86	ca. 4.0	5.0	[32]
MXene aerogel	−29.0	ca. 1.8	4.0	[33]
Chitin nanofiber-derived carbon honeycomb	−41.3	4.2	6.9	This work

[a] Absorption bandwidth: the bandwidth for effective microwave absorption (the minimum reflection loss values less than –10 dB).

The mechanism of frequency-tunable absorption is discussed next. The observed maximum absorption frequencies (10.4, 11.0, 11.5, and 12.1 GHz) at compression strains of 0, 20, 40, and 60% (respectively) were consistent with the impedance-matched frequencies, wherein the impedance matching values ($|Z_{in}-1|$) were close to zero (**Fig. 2-7b**). In the impedance-matched frequency range, absorption is the most effective while reflection usually is suppressed [19,34]. According to the quarter-wavelength theory [12], the impedance-matched frequency tends to increase with decreasing the thickness and dielectric permittivity of the microwave absorber.

Upon compressing the elastic carbon honeycomb from 0 to 60%, its thickness reduced and dielectric permittivity increased, indicating that thickness reduction plays an important role in increasing the impedance-matched frequency (maximum absorption frequency) of the carbon honeycomb (see **Fig. 2-8** for more details).

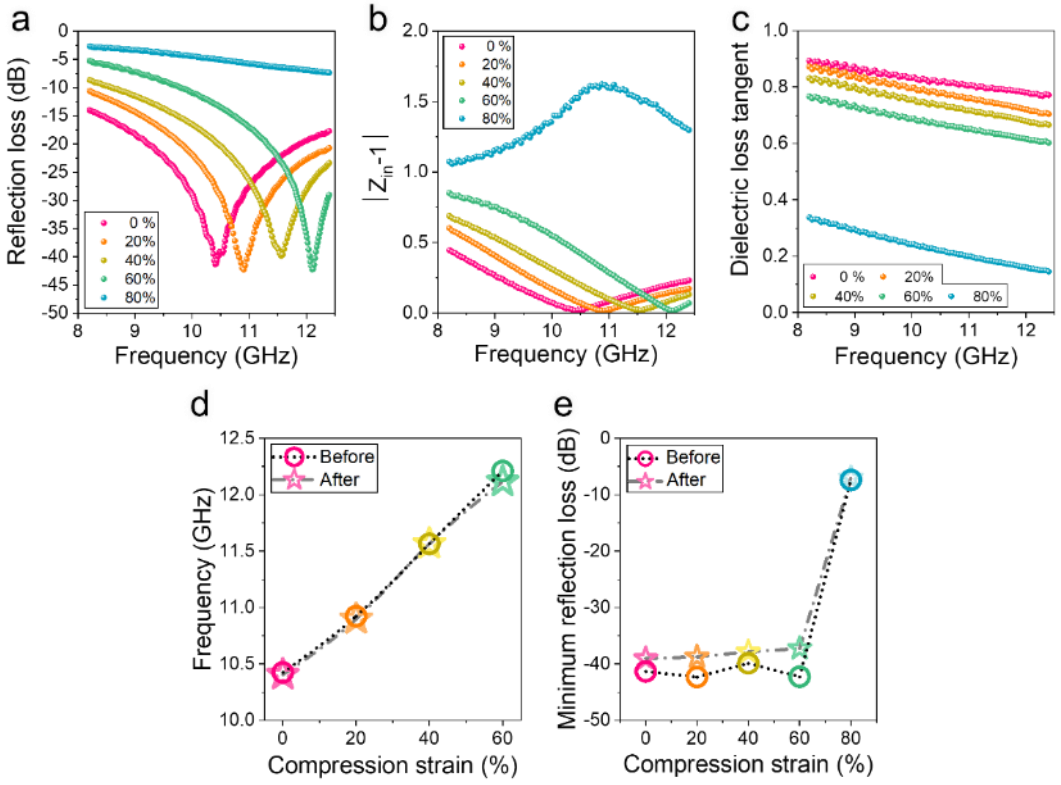


Fig. 2-7 Frequency-tunable and absorption/transmission-switchable microwave absorption performance of the chitin nanofiber-derived carbon honeycomb upon compression in the perpendicular direction to the anisotropic porous channel. (a) Reflection loss (RL), (b) impedance matching value ($|Z_{in}-1|$), and (c) dielectric loss tangent versus frequency at the compression strain of 0, 20, 40, 60, and 80%. (d) Frequency at the minimum RL of the carbon honeycomb at different compression strains, and (e) minimum RL of the carbon honeycomb at different compression strains before and after 60,000 cycles of compression and recovery at a strain of 80%. For calculation of the RL, thicknesses of the carbon honeycombs were 6.90, 5.52, 4.14, 2.76, and 1.38 mm at compression strains of 0, 20, 40, 60, and 80%, respectively. Carbonization temperature: 800 °C.

The impedance-matched frequency (f_m) at a specific thickness (t_m) is determined by quarter-wavelength theory, as expressed by the following equation (**Equation 2.6**) [18]:

$$f_m = \frac{nc}{4t_m\sqrt{|\mu_r\varepsilon_r|}} \quad (n = 1, 3, 5\ldots\ldots) \tag{2.6}$$

where c is the speed of light (3×10^8 m s^{-1}), ε_r and μ_r are the dielectric permittivity and magnetic

permeability, respectively, f_m (GHz) is the impedance-matched frequency, and t_m is the thickness (mm) of the microwave absorber.

Because carbon materials are generally non-magnetic [35], the $\mu_r = 1$ was considered for the chitin nanofiber-derived carbon honeycomb [36]. Therefore, **Equation 2.6** can be simplified as **Equation 2.7** [37]:

$$f_m = \frac{nc}{4t_m\sqrt{|\varepsilon_r|}} \quad (n=1, 3, 5\ldots\ldots) \qquad (2.7)$$

Thus, the impedance-matched frequency (f_m, GHz) is determined by the thickness and dielectric permittivity of the carbon honeycomb. The impedance-matched frequency tends to increase with decreasing thickness (t_m, mm) and modulus of dielectric permittivity ($\sqrt{|\varepsilon_r|}$).

The impedance-matched frequency of the carbon honeycomb increased with increasing compression strain (**Fig. 2-7b**). To reveal the dominant factor governing the impedance-matched frequency (*i.e.,* absorption-frequency) tuning, the change in the values of $\sqrt{|\varepsilon_r|}$ and t_m from $\sqrt{|\varepsilon_{r0\%}|}$ and $t_{m0\%}$, respectively, were calculated at different compression strains. As shown in **Fig. 2-8**, t_m (mm) decreased and $\sqrt{|\varepsilon_r|}$ increased with increasing compression strain. Because the impedance-matched frequency tends to increase with decreasing thickness and modulus of dielectric permittivity, the reduced thickness was the major contributing factor to the compression-tuned absorption frequency of the carbon honeycomb.

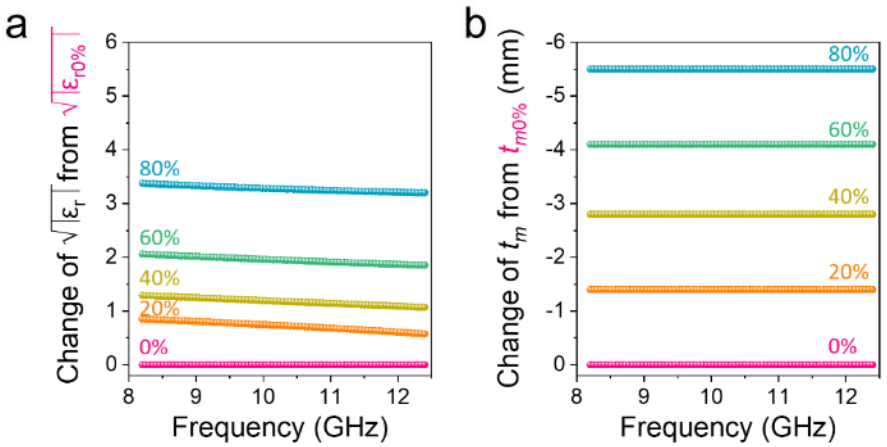


Fig. 2-8 Changes in (a) dielectric permittivity (ε_r) and (b) thickness (t_m) from original dielectric permittivity ($\varepsilon_{r0\%}$) and thickness ($t_{m0\%}$) of chitin nanofiber-derived carbon honeycomb upon its compression at strains from 20 to 80%. The thicknesses were 6.90, 5.52, 4.14, 2.76, and 1.38 mm at the compression strains of 0, 20, 40, 60, and 80%, respectively. Carbonization temperature: 800 °C.

The dielectric loss tangent, which comprises conductive and polarization losses, is also key parameter for the conversion of microwave to heat or other forms of energy, thus affecting the

microwave absorption performance[13,38,39,40,41]. The excessive, moderate, and low dielectric loss tangent is reportedly related to the reflection, absorption, and transmission of microwaves, respectively [3,42,43]. Although the dielectric loss tangent of the carbon honeycomb gradually decreased with increasing compression strain from 0 to 60% (**Fig. 2-7c**), its value could be maintained at a moderate level for microwave absorption at the impedance-matched frequency (**Fig. 2-7a**). Thus, the carbon honeycomb achieved frequency-tunable microwave absorption by reducing its thickness upon compression while maintaining good impedance matching and moderate dielectric loss tangent (**Fig. 2-9a**).

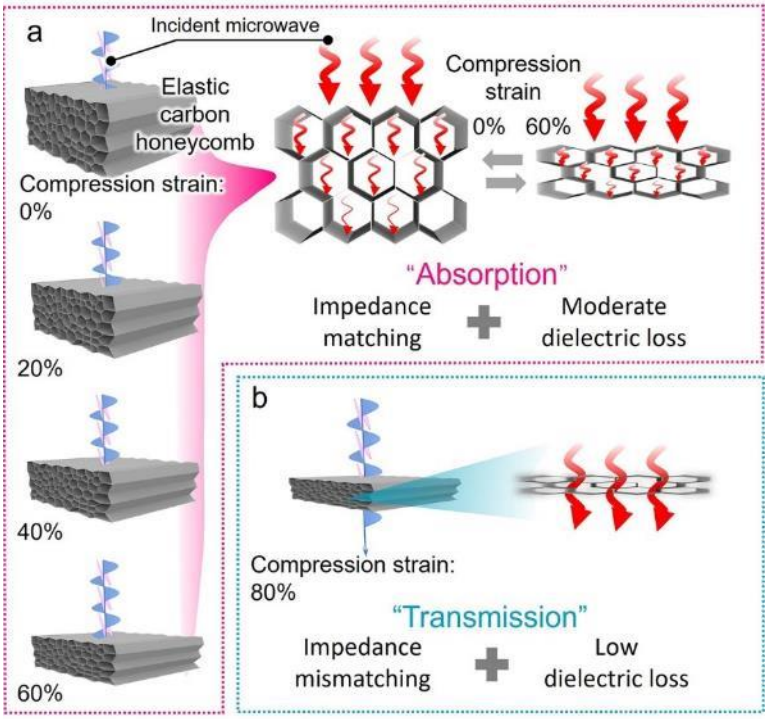


Fig. 2-9 Schematics showing microwave (a) absorption and (b) transmission mechanisms by the chitin nanofiber-derived carbon honeycomb upon compression from 0 to 60% and from 60 to 80%, respectively.

Frequency-tunable microwave absorption should be conducted reversibly and repeatedly to satisfy specific application requirements and/or real-time environmental changes. As shown in **Fig. 2-7d** and **e**, the frequencies at the minimum reflection (*i.e.*, the maximum absorption frequencies) and the minimum RL values of the carbon honeycomb at compression strains of 0, 20, 40, and 60% remained almost unchanged even after 60,000 cycles of compression and recovery at a strain of 80%. This indicated that the frequency-tunable microwave absorption ability of the carbon honeycomb was reversible and repeatable. Such robust frequency-tunable absorption of the carbon honeycomb is related to its high compression fatigue resistance (**Fig.**

2-5c-f), which retained the impedance matching and dielectric loss tangent even after 60,000 cycles of compression and recovery (**Fig. 2-10**).

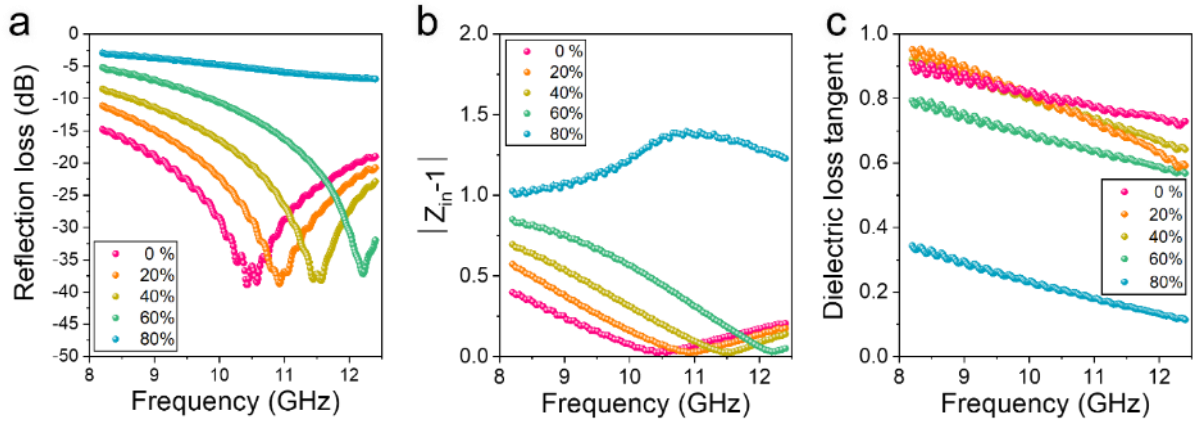


Fig. 2-10 (a) Reflection loss, (b) impedance matching value ($|Z_{in}-1|$), and (c) dielectric loss tangent versus frequency of the chitin nanofiber-derived carbon honeycomb at different compression strains after 60,000 cycles of compression and recovery. For calculation of the reflection loss, thicknesses of the carbon honeycomb were 6.90, 5.52, 4.14, 2.76, and 1.38 mm at compression strains of 0, 20, 40, 60, and 80%, respectively. Carbonization temperature: 800 °C.

2.3.3 Absorption/transmission-switchable microwave absorption by chitin nanofiber-derived elastic carbon honeycomb

As shown in **Fig. 2-7a**, further compression of the carbon honeycomb from 60 to 80% strain resulted in poor microwave absorption performance (RL: more than −10 dB) over the entire X-band. To elaborate the poor microwave absorption of the carbon honeycomb at a compression strain of 80%, its reflection, transmission, and absorption coefficient values were calculated, based on the logarithmic ratio of incident power to transmission power [44,45,46,47] (**Fig. 2-11**).

Based on the electromagnetic shielding theory, the reflection (R), transmission (T), and absorption (A) coefficient values were calculated from the *S* parameters according to the following equations (Equation 2.8–2.10 [44,46]):

$$R = {s_{11}}^2 \quad (2.8)$$

$$T = {s_{21}}^2 \quad (2.9)$$

$$A = 1 - R - T \quad (2.10)$$

where S_{11} represents the reflection loss of port 1 in the equivalent two-port vector network analyzer, and S_{21} represents the insertion loss of the signal from port 1 to port 2.

The carbon honeycomb showed very low reflection coefficient, regardless of its compression

strains (**Fig. 2-11a**). The absorption coefficient was higher than the transmission coefficient at compression strains of 0–60%, while the transmission coefficient was higher than the absorption coefficient at a compression strain of 80% (**Fig. 2-11b and c**). In other words, microwave absorption is dominant at compression strains of 0–60%, while microwave transmission is dominant at a compression strain of 80%. These results indicated that the carbon honeycomb can switch from absorption to transmission when the compression strain increased from 60 to 80%. At a compression strain of 80%, the carbon honeycomb showed very low reflection coefficient (**Fig. 2-11a**), while its transmission coefficient was higher than its absorption coefficient (**Fig. 2-11b and c**).

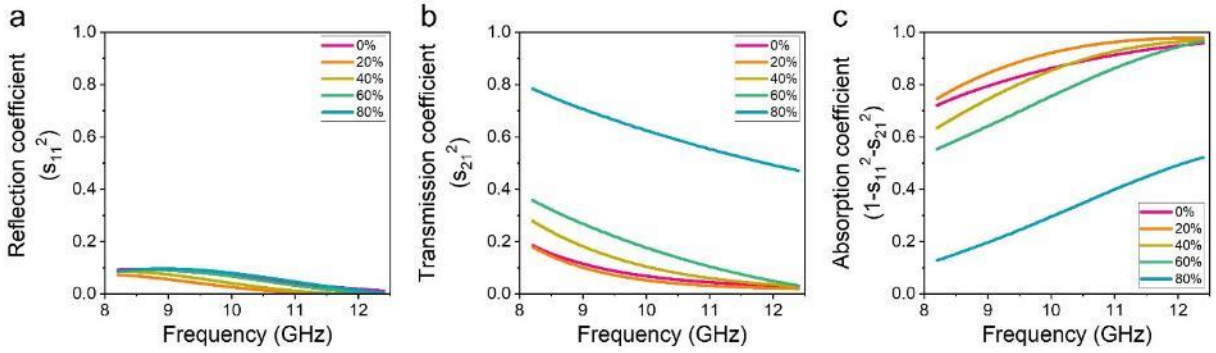


Fig. 2-11 (a) Reflection, (b) transmission, and (c) absorption coefficient values of the chitin nanofiber-derived carbon honeycomb at different compression strains.

These results indicated that the carbon honeycomb could allow microwave transmission at a compression strain of 80%. Moreover, the impedance matching value ($|Z_{in}–1|$) of the carbon honeycomb increased (**Fig. 2-7b**) and its dielectric loss tangent drastically decreased (**Fig. 2-7c**). Such impedance mismatch leads to either microwave transmission or reflection [3,48] , while low dielectric loss tangent is reportedly related to microwave transmission [43,34,49]. Thus, the carbon honeycomb switched from microwave absorption to transmission in the X-band upon compressing it to 80% strain possibly by causing impedance mismatch and changing its dielectric loss tangent from moderate to low levels (**Fig. 2-9b**). The minimum RL values at compression strains of 60 and 80% remained almost unchanged even after 60,000 cycles of compression and recovery (**Fig. 2-7e**, see also **Fig. 2-10**), indicating that the absorption/transmission switching was reversible and repeatable.

As described above, the carbon honeycomb switched from microwave absorption to transmission upon compressing it to 80% strain, while drastically decreasing its dielectric loss tangent. Because the dielectric loss tangent is expressed as the imaginary part (ε'') divided by the real part (ε') of the complex dielectric permittivity [50], changes in ε' and ε'' of the carbon

honeycomb upon compression were analyzed to discuss the switching mechanism. The ε' and ε'' of the carbon honeycomb increased in a similar way at compression strains from 0 to 60%. In contrast, the ε' showed a much higher increase than ε'' upon further compressing the honeycomb to 80% (**Fig. 2-12a and b**), drastically decreasing its dielectric loss tangent (**Fig. 2-7c**). Theoretically, ε' and ε'' increase with capacitance and electrical conductivity, respectively [51,52]. Therefore, the drastic decrease in dielectric loss tangent ($\varepsilon''/\varepsilon'$) of the carbon honeycomb was dominated by the increase in the capacitance rather than the electrical conductivity, although both the capacitance and electrical conductivity increased upon compression from 60 to 80% strain (**Fig. 2-12c and d**). This significant increase in the capacitance was mainly due to the increase in its dielectric permittivity as less air remained within the carbon honeycomb at a high compression strain, especially at 80%.

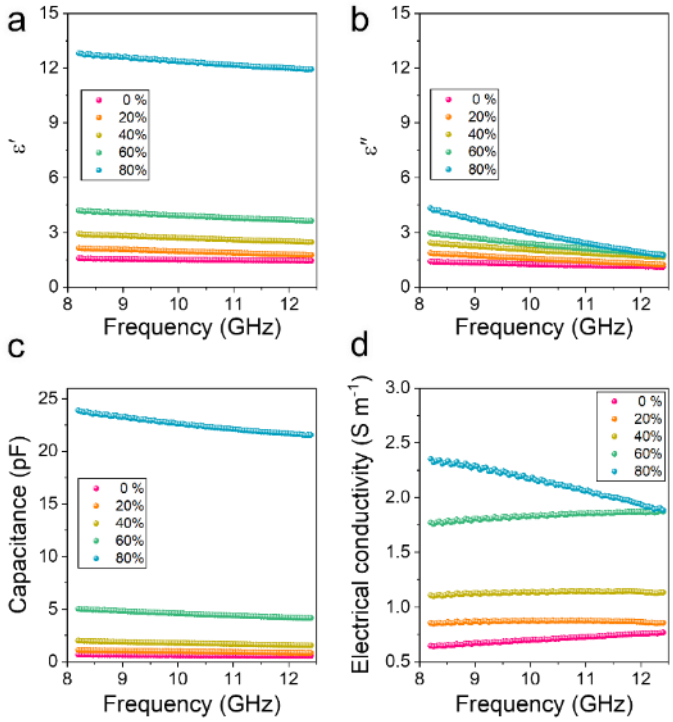


Fig. 2-12 Change in complex dielectric permittivity, capacitance, and electrical conductivity of the chitin nanofiber-derived carbon honeycomb upon compression in the perpendicular direction to the anisotropic porous channel. (a) Real part (ε'), (b) imaginary part (ε'') of the complex dielectric permittivity, and (c) capacitance and (d) electrical conductivity under alternating current (AC) versus frequency at different compression strains. These values were measured in the same direction as the compression. Carbonization temperature: 800 °C.

To realize absorption/transmission switching and absorption-frequency tuning by compression, it is also important to properly tune the impedance matching and dielectric loss

tangent of the uncompressed carbon honeycomb. In our previous study, the carbonization temperature for the carbon honeycombs was controlled to tailor their N- and O-doped defective carbon structures, which largely affected their impedance matching and dielectric loss tangent, and thus microwave absorption performance (**Fig. 2-13 and 2-14**).

The chitin honeycombs carbonized at 700, 800, and 900 °C had the N- and O-doped defective carbon structures [13]. In this study, the XPS spectra of the carbon honeycombs were recorded with a JPS-9010 photoelectron spectrometer (JEOL Ltd, Tokyo, Japan) using monochromatic Al Ka (1486.6 eV) radiation as the excitation source. The HR-TEM images of the carbon honeycombs were obtained using a JEM-ARM200F instrument (JEOL, Ltd., Tokyo, Japan). The wide XPS spectra confirmed the presence of C, O, and N in the carbon honeycombs (**Fig. 2-13a**). The C 1s XPS spectra were deconvoluted into five peaks: C–C or C=C (284.6 eV), C=N (285.8 eV), C–O (286.1 eV), C–N (287.4 eV), and C=O (287.8 eV) [53] (**Fig. 2-13b**). The N 1s XPS spectra indicated the formation of pyridinic N (398.4 eV), pyrrolic N (399.9 eV), and graphitic N (401.0 eV) [54] (**Fig. 2-13c**). The growth of the graphitic carbon domains within the chitin nanofiber-derived carbon honeycomb with increasing carbonization temperatures (**Fig. 2-13d-f**) was due to the gradual removal of N, O, and H [13].

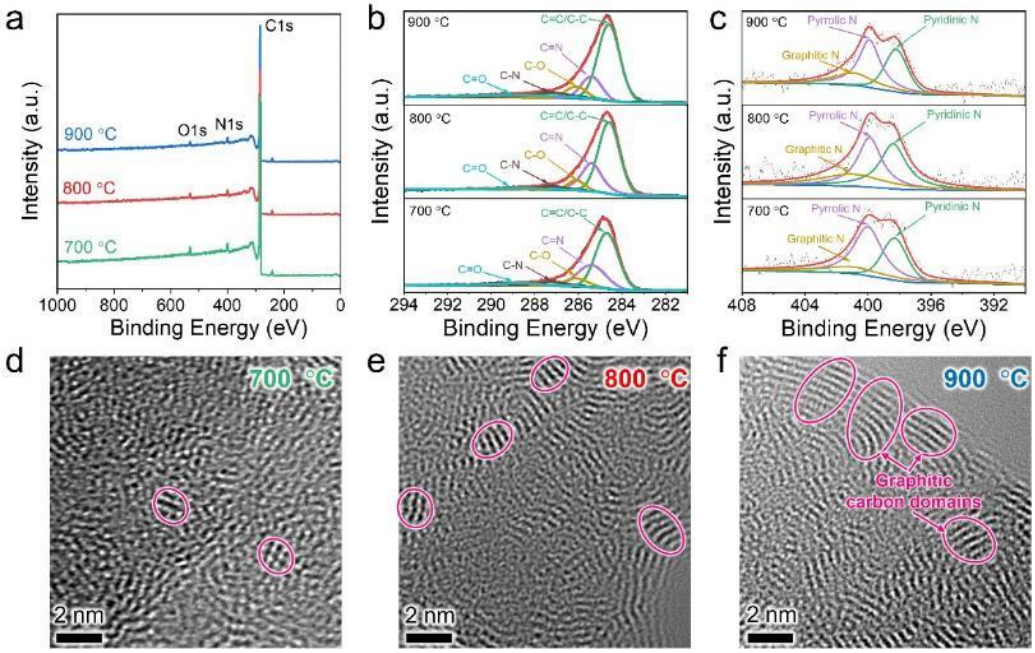


Fig. 2-13 (a) Wide X-ray photoelectron spectroscopy (XPS) spectra, (b) C 1s XPS spectra, (c) N 1s XPS spectra of the chitin honeycombs carbonized at 700, 800, and 900 °C, and high-resolution transmission electron microscopy (HR-TEM) images of the chitin honeycombs carbonized at (d) 700 °C, (e) 800 °C, and (f) 900 °C. Pink circles represent the graphitic carbon domain region.

The graphitic carbon domains within the chitin nanofiber-derived carbon honeycomb were gradually grown at increasing carbonization temperatures (Fig. 2-13d-f), thereby increasing its electrical conductivity (**Fig. 2-14a**). The chitin honeycomb carbonized at 700 °C showed relatively low electrical conductivity (Fig. 2-14a), resulting in its impedance mismatching and low dielectric loss and thus poor microwave absorption (**Fig. 2-14b-d**). The chitin honeycomb carbonized at 900 °C showed relatively high electrical conductivity (Fig. 2-14a), resulting in its impedance mismatching and excessive dielectric loss and thus poor microwave absorption (Fig. 2-14b-d). By contrast, the chitin honeycomb carbonized at 800 °C showed moderate electrical conductivity (Fig. 2-14a), providing its impedance matching and moderate dielectric loss and, thus, effective microwave absorption (Fig. 2-14b-d). Thus, the chitin honeycomb carbonized at 800 °C had the optimized defective carbon structure for strong microwave absorption.

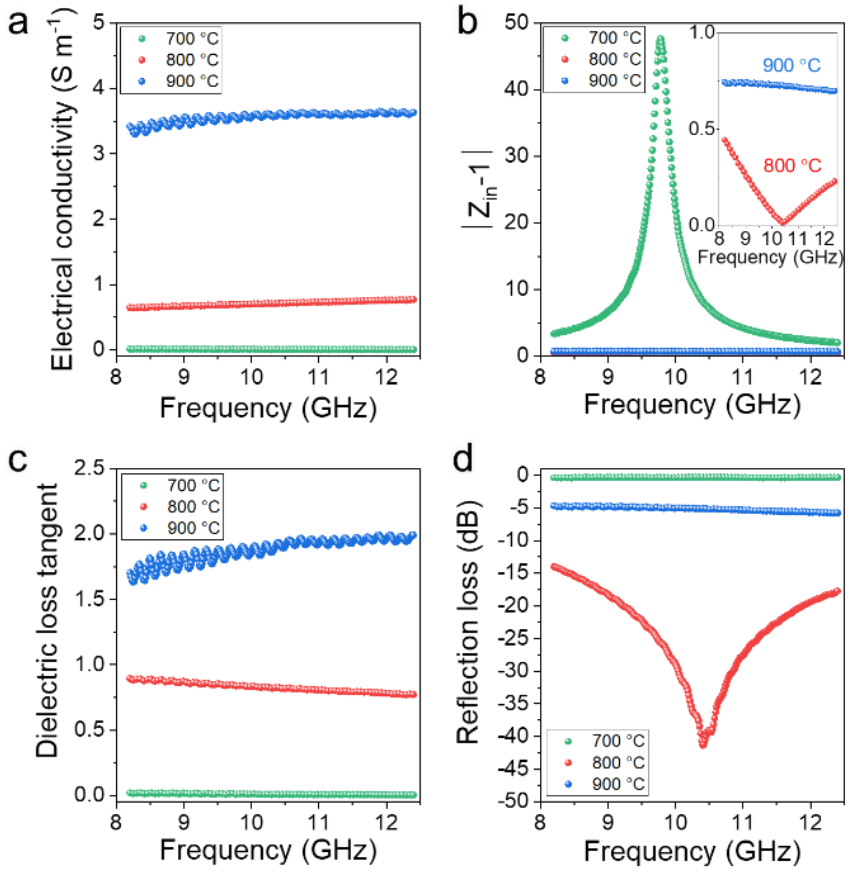


Fig. 2-14 (a) AC electrical conductivity, (b) impedance matching value ($|Z_{in}-1|$), (c) dielectric loss tangent, and (d) reflection loss versus frequency of the chitin nanofiber-derived carbon honeycombs without compression. Carbonization temperatures: 700, 800, and 900 °C.

The carbon honeycomb carbonized at 800 °C had the optimized defective carbon structures, providing good impedance matching, moderate dielectric loss tangent, and strong microwave

absorption [13]. This carbon honeycomb showed frequency-tunable microwave absorption upon compression from 0 to 60% strain and absorption/transmission switching at 80% strain. On the other hand, the carbon honeycombs carbonized at 700 °C and 900 °C showed sufficient elastic properties to allow mechanical compression up to 80% strain. Regardless of the compression strain, poor microwave absorption performance was observed for the carbon honeycomb carbonized at 700 °C because of its impedance mismatch and low dielectric loss properties (**Fig. 2-15a-c**). The carbon honeycomb carbonized at 900 °C also showed poor microwave absorption performance because it exhibited impedance mismatch and excessive dielectric loss properties (**Fig. 2-15d-f**). These results indicated that the initial impedance matching and dielectric loss tangent of the carbon honeycomb should be set at a good level and a moderate level, respectively. Only then, subsequent compression could allow tuning of the maximum-absorption frequency and switching from the absorption to transmission.

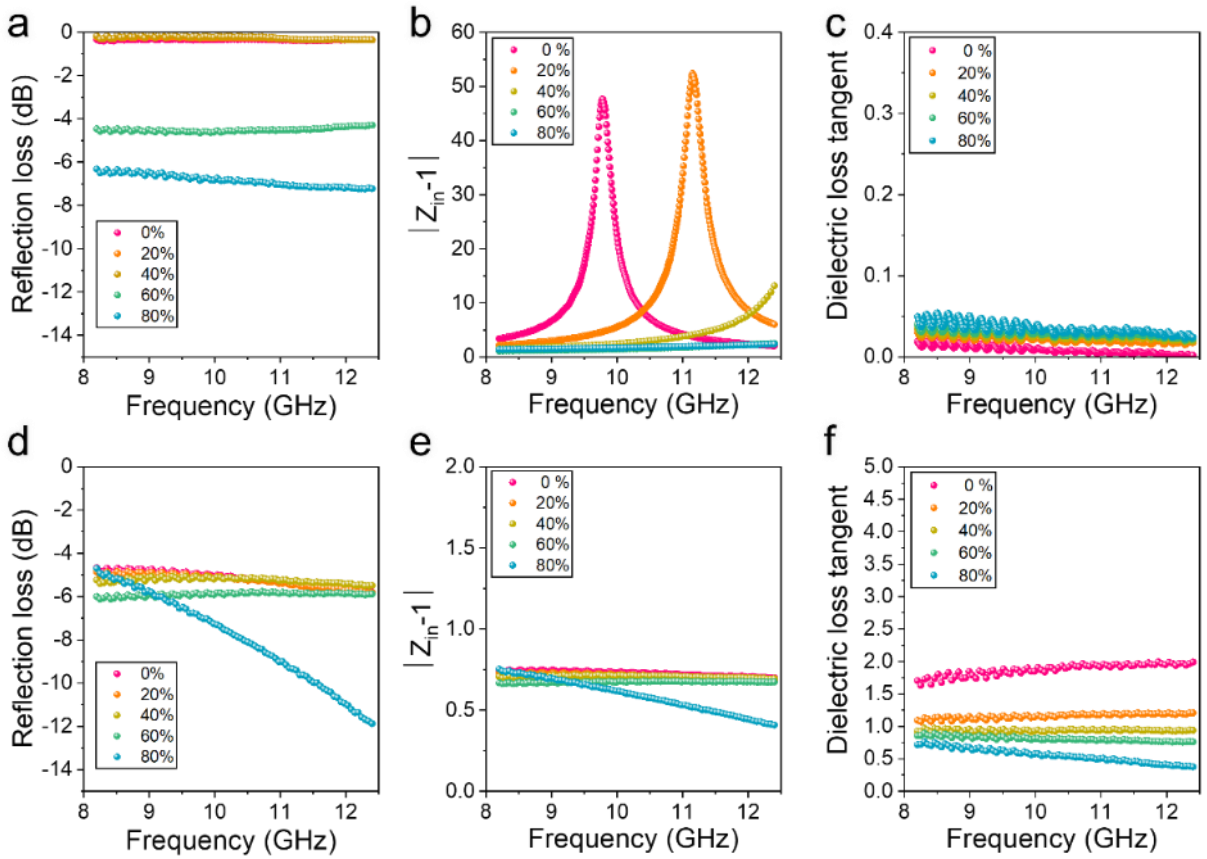


Fig. 2-15 Microwave absorption performances of chitin nanofiber-derived carbon honeycombs carbonized at 700 and 900 °C. (a, d) Reflection loss, (b, e) impedance matching ($|Z_{in}-1|$), and (c, f) dielectric loss tangent versus frequency at different compressions. Carbonization temperatures: (a−c) 700 and (d−f) 900 °C. For calculation of the reflection loss, thicknesses of each carbon honeycomb were 6.90, 5.52, 4.14, 2.76, and 1.38 mm at compression strains of 0, 20, 40, 60, and 80%, respectively.

The elastic carbon black nanoparticles/wood-derived lamellar carbon honeycomb with low dielectric loss tangent reported previously [6] switched from microwave transmission to absorption upon compression by an increase in the electrical conductivity and ε''. On the other hand, our elastic chitin nanofiber-derived carbon honeycomb with moderate dielectric loss tangent could tune the maximum-absorption frequency by reducing its thickness and maintaining its moderate dielectric loss tangent, while it could switch from absorption to transmission upon further compression by the predominant increase in the capacitance and ε'. The absorption bandwidth in the X-band of the chitin nanofiber-derived carbon honeycomb was 4.2 (8.2–12.4 GHz), 4.2 (8.2–12.4 GHz), 3.8 (8.6–12.4 GHz), 2.6 (9.8–12.4 GHz), and 0 GHz at compression strains of 0, 20, 40, 60, and 80%, respectively (**Table 2-2**). Moreover, the chitin nanofiber-derived carbon honeycomb showed poor microwave reflection regardless of its compression strains (**Fig. 2-11**). These results suggest that the microwave absorption properties of the carbon honeycomb can be tuned by compression to transmit required frequencies and absorb unwanted frequencies in the X-band (see Table 2-2 for more details). As chitin is one of the most abundant and renewable biomass materials on Earth, our strategy opens a door for the development of smart and sustainable microwave absorbers.

Table 2-2 Absorption frequency range and absorption bandwidth of the chitin nanofiber-derived carbon honeycomb at compression strains of 0–80%.

Compression strain [%]	Absorption frequency range [GHz][a)]	Absorption bandwidth [GHz][b)]
0	8.2–12.4	4.2
20	8.2–12.4	4.2
40	8.6–12.4	3.8
60	9.8–12.4	2.6
80	–	0

[a] Absorption frequency range: the frequency range for effective microwave absorption (the minimum reflection loss values less than –10 dB).
[b] Absorption bandwidth: the bandwidth for effective microwave absorption (the minimum reflection loss values less than –10 dB).

The X-band (8.2–12.4 GHz) makes a significant contribution to various civilian wireless services, such as satellite communications (8.0–8.5 GHz) [55], fishery marine radar communications (9.1–9.7 GHz) [56], and many precision electrons paramagnetic resonance spectrometers (near 9.8 GHz) [57]. The absorption bandwidth in the X-band of the carbon honeycomb was 4.2 (8.2–12.4 GHz), 4.2 (8.2–12.4 GHz), 3.8 (8.6–12.4 GHz), 2.6 (9.8–12.4

GHz), and 0 GHz at compression strains of 0, 20, 40, 60, and 80%, respectively (Table 2-2). Moreover, the carbon honeycomb showed poor microwave reflection regardless of its compression strains (**Fig. 2-11**). Therefore, the carbon honeycomb can tune its microwave absorption properties by its compression degree to transmit required frequencies and absorb unwanted frequencies, in accordance with the abovementioned specific application requirements and/or real-time situations and environmental changes.

2.4 Conclusion

Herein, frequency-tunable microwave absorption and switchable microwave absorption or transmission were successfully demonstrated using a single chitin nanofiber-derived carbon honeycomb. The carbon honeycomb with honeycomb-like anisotropic porous channels has good elastic properties and high compression fatigue resistance, allowing mechanical compression and recovery in the direction perpendicular to the porous channels. The uncompressed carbon honeycomb showed a maximum microwave absorption of approximately −40 dB at 10.4 GHz, owing to its good impedance matching and moderate dielectric loss tangent. The thickness, impedance matching, and dielectric loss tangent of the carbon honeycomb could be tuned by compressing it along the direction perpendicular to the anisotropic porous channels. When the compression strain was varied from 0 to 20, 40, and 60%, the maximum-absorption frequency was observed to vary from 10.4 to 11.0, 11.5, 12.1 GHz, respectively, because the thickness of the carbon honeycomb was reduced, and its good impedance matching and moderate dielectric loss tangent were maintained. Furthermore, the carbon honeycomb could switch from absorption to transmission when the compression strain increased from 60 to 80% by causing impedance mismatch and changing its dielectric loss tangent from moderate to low levels. Thus, the carbon honeycomb achieved frequency-tunable and absorption/transmission-switchable microwave absorption, suggesting its potential applicability as a smart microwave absorber in the X-band. The key to the smart microwave absorption was through the use of the elastic carbon honeycomb with good impedance matching and moderate dielectric loss tangent and tuning its thickness, impedance matching, and dielectric loss tangent by controlling the compression. This smart microwave absorption was reversible and repeatable over at least 60,000 cycles of compression and recovery. This study paves the way for the design of a smart and robust microwave absorber that can reversibly tune its properties on demand.

2.5 References

1 T. D. Ponnimbaduge Perera, D. N. K. Jayakody, S. K. Sharma, S. Chatzinotas and J. Li, *IEEE Commun. Surv. Tutorials*, 2018, **20**, 264–302.

2 F. Shahzad, M. Alhabeb, C. B. Hatter, B. Anasori, S. M. Hong, C. M. Koo and Y. Gogotsi, *Science*, 2016, **353**, 1137–1140.

3 F. Meng, H. Wang, F. Huang, Y. Guo, Z. Wang, D. Hui and Z. Zhou, *Compos. Part B Eng.*, 2018, **137**, 260–277.

4 Z. Cheng, R. Wang, Y. Cao, Z. Cai, Z. Zhang and Y. Huang, *Adv. Funct. Mater.*, 2022, **32**, 2205160.

5 F. Ye, Q. Song, Z. Zhang, W. Li, S. Zhang, X. Yin, Y. Zhou, H. Tao, Y. Liu, L. Cheng, L. Zhang and H. Li, *Adv. Funct. Mater.*, 2018, **28**, 1707205.

6 X. Liu, Y. Li, X. Sun, W. Tang, G. Deng, Y. Liu, Z. Song, Y. Yu, R. Yu, L. Dai and J. Shui, *Matter*, 2021, **4**, 1735–1747.

7 Y. Tang, W. Dong, L. Tang, Y. K. Zhang, J. Kong and J. Gu, *Compos. Commun.*, 2018, **8**, 36–41.

8 N. Yousefi, X. Sun, X. Lin, X. Shen, J. Jia, B. Zhang, B. Tang, M. Chan and J. K. Kim, *Adv. Mater.*, 2014, **26**, 5480–5487.

9 Y. Xia, W. Gao and C. Gao, *Adv. Funct. Mater.*, 2022, **32**, 2204591.

10 X. Zeng, X. Cheng, R. Yu and G. D. Stucky, *Carbon*, 2020, **168**, 606–623.

11 F. Ruiz-Perez, S. M. López-Estrada, R. V. Tolentino-Hernández and F. Caballero-Briones, *J. Sci. Adv. Mater. Devices*, 2022, **7**, 100454.

12 Y. Liu, Y. Liu and M. G. B. Drew, *Phys. Scr.*, 2022, **97**, 015806.

13 X. Li, L. Zhu, T. Kasuga, M. Nogi and H. Koga, *Chem. Eng. J.*, 2022, **450**, 137943.

14 J. B. Kim, S. K. Lee and C. G. Kim, *Compos. Sci. Technol.*, 2008, **68**, 2909–2916.

15 X. Peng, K. Wu, Y. Hu, H. Zhuo, Z. Chen, S. Jing, Q. Liu, C. Liu and L. Zhong, *J. Mater. Chem. A*, 2018, **6**, 23550–23559.

16 Y. Si, J. Yu, X. Tang, J. Ge and B. Ding, *Nat. Commun.*, 2014, **5**, 5802.

17 S. S. Kim, S. B. Jo, K. I. Gueon, K. K. Choi, J. M. Kim and K. S. Churn, *IEEE Trans. Magn.*, 1991, **27**, 5462–5464.

18 Y. Naito and K. Suetake, *IEEE Trans. Microw. Theory Tech.*, 1971, **19**, 65–72.

19 H. Xu, X. Yin, M. Zhu, M. Han, Z. Hou, X. Li, L. Zhang and L. Cheng, *ACS Appl. Mater. Interfaces*, 2017, **9**, 6332–6341.

20 C. Tian, Y. Du, P. Xu, R. Qiang, Y. Wang, D. Ding, J. Xue, J. Ma, H. Zhao and X. Han, *ACS Appl. Mater. Interfaces*, 2015, **7**, 20090–20099.

21 X. Li, L. Yu, L. Yu, Y. Dong, Q. Gao, Q. Yang, W. Yang, Y. Zhu and Y. Fu, *Chem. Eng. J.*, 2018, **352**, 745–755.
22 J. Huang, B. G. Sumpter and V. Meunier, *Angew. Chem. Int. Ed.*, 2008, **47**, 520–524.
23 A. K. Jonscher, *Nature*, 1977, **267**, 673–679.
24 J. D. Goodrich and W. T. Winter, *Biomacromolecules*, 2007, **8**, 252–257.
25 S. Deville, E. Saiz, R. K. Nalla and A. P. Tomsia, *Science*, 2006, **311**, 515–518.
26 K. H. Kim, Y. Oh and M. F. Islam, *Nat. Nanotechnol.*, 2012, **7**, 562–566.
27 T. A. Schaedler, A. J. Jacobsen, A. Torrents, A. E. Sorensen, J. Lian, J. R. Greer, L. Valdevit and W. B. Carter, *Science*, 2011, **334**, 962–965.
28 L. Qiu, J. Z. Liu, S. L. Y. Chang, Y. Wu and D. Li, *Nat. Commun.*, 2012, **3**, 1241.
29 C. Li, M. Ding, B. Zhang, X. Qiao and C. Y. Liu, *Nanoscale*, 2018, **10**, 18291–18299.
30 L. Liang, Q. Li, X. Yan, Y. Feng, Y. Wang, H. Bin Zhang, X. Zhou, C. Liu, C. Shen and X. Xie, *ACS Nano*, 2021, **15**, 6622–6632.
31 Z. Wang, R. Wei, J. Gu, H. Liu, C. Liu, C. Luo, J. Kong, Q. Shao, N. Wang, Z. Guo and X. Liu, *Carbon*, 2018, **139**, 1126–1135.
32 X. Huang, G. Yu, Y. Zhang, M. Zhang and G. Shao, *Chem. Eng. J.*, 2021, **426**, 131894.
33 Y. Dai, X. Wu, Z. Liu, H. Bin Zhang and Z. Z. Yu, *Compos. Part B Eng.*, 2020, **200**, 108263.
34 C. M. Watts, X. Liu and W. J. Padilla, *Adv. Mater.*, 2012, **24**, OP98–OP120.
35 D. D. L. Chung, *Carbon*, 2001, **39**, 279–285.
36 W. Liu, J. Pan, G. Ji, X. Liang, Y. Cheng, B. Quan and Y. Du, *Dalt. Trans.*, 2017, **46**, 3700–3709.
37 J. Zhou, F. Guo, J. Luo, G. Hao, G. Liu, Y. Hu, G. Zhang, H. Guo, H. Zhou and W. Jiang, *J. Mater. Chem. C*, 2022, **10**, 1470–1478.
38 F. Pan, L. Cai, Y. Shi, Y. Dong, X. Zhu, J. Cheng, H. Jiang, X. Wang, Y. Jiang and W. Lu, *Nano-Micro Lett.*, 2022, **14**, 1–18.
39 F. Pan, Y. Rao, D. Batalu, L. Cai, Y. Dong, X. Zhu, Y. Shi, Z. Shi, Y. Liu and W. Lu, *Nano-Micro Lett.*, 2022, **14**, 1–17.
40 L. Cai, F. Pan, X. Zhu, Y. Dong, Y. Shi, Z. Xiang, J. Cheng, H. Jiang, Z. Shi and W. Lu, *Chem. Eng. J.*, 2022, **434**, 133865.
41 J. Cheng, H. Jiang, L. Cai, F. Pan, Y. Shi, X. Wang, X. Zhang, S. Lu, Y. Yang, L. Li, Z. Xiu, J. Wang, H. Guo and W. Lu, *Chem. Eng. J.*, 2023, **457**, 141208.
42 I. Choi, J. G. Kim, D. G. Lee and I. S. Seo, *Compos. Sci. Technol.*, 2011, **71**, 1632–1638.
43 Y. Yang, L. Xia, T. Zhang, B. Shi, L. Huang, B. Zhong, X. Zhang, H. Wang, J. Zhang

and G. Wen, *Chem. Eng. J.*, 2018, **352**, 510–518.

44 Y. Xie, S. Liu, K. Huang, B. Chen, P. Shi, Z. Chen, B. Liu, K. Liu, Z. Wu, K. Chen, Y. Qi and Z. Liu, *Adv. Mater.*, 2022, **34**, 2202982.

45 P. Yi, H. Zou, Y. Yu, X. Li, Z. Li, G. Deng, C. Chen, M. Fang, J. He, X. Sun, X. Liu, J. Shui and R. Yu, *ACS Nano*, 2022, **16**, 14490–14502.

46 Y. Yu, P. Yi, W. Xu, X. Sun, G. Deng, X. Liu, J. Shui and R. Yu, *Nano-Micro Lett.*, 2022, **14**, 1–15.

47 L. Jinjin, Z. Yue, L. Xufeng, C. Chunyan, Z. Haihan, Y. Peng, L. Xiaofang and Y. Ronghai, *Nano Res.*, 2023, **16**, 1764–1772.

48 F. Meng, H. Wang, W. Wei, Z. Chen, T. Li, C. Li, Y. Xuan and Z. Zhou, *Nano Res.*, 2018, **11**, 2894.

49 G. Ma, Y. Zeng, X. Yang, Y. Liu and Y. Duan, *J. Mater. Sci. Mater. Electron.*, 2020, **31**, 8627–8636.

50 C. P. Neo and V. K. Varadan, *IEEE Trans. Electromagn. Compat.*, 2004, **46**, 102–106.

51 X. X. Wang, M. Zhang, J. C. Shu, B. Wen, W. Q. Cao and M. S. Cao, *Carbon*, 2021, **184**, 136–145.

52 X. Qian, Y. Zhang, Z. Wu, R. Zhang, X. Li, M. Wang and R. Che, *Small*, 2021, **17**, 2100283.

53 H. Yu, L. Shang, T. Bian, R. Shi, G. I. N. Waterhouse, Y. Zhao, C. Zhou, L. Z. Wu, C. H. Tung and T. Zhang, *Adv. Mater.*, 2016, **28**, 5080–5086.

54 H. Bin Yang, J. Miao, S. F. Hung, J. Chen, H. B. Tao, X. Wang, L. Zhang, R. Chen, J. Gao, H. M. Chen, L. Dai and B. Liu, *Sci. Adv.*, 2016, **2**, 1–12.

55 E. Y. Jung, J. W. Lee, T. K. Lee and W. K. Lee, *IEEE Trans. Antennas Propag.*, 2012, **60**, 3632–3639.

56 F. Y. Kuo and R. B. Hwang, *IEEE Trans. Antennas Propag.*, 2014, **62**, 2331–2337.

57 I. V. Alenkina, M. I. Oshtrakh, Z. Klencsár, E. Kuzmann, A. V. Chukin and V. A. Semionkin, *Spectrochim. Acta - Part A Mol. Biomol. Spectrosc.*, 2014, **130**, 24–36.

Chapter 3. Super-compressible, elastic, and robust chitin nanofiber-derived carbon honeycomb and its pressure sensing properties over an ultrawide temperature range

3.1 Introduction

Elastic carbon aerogels are considered ideal candidates for applications such as triboelectric nanogenerators,[1] flexible energy storage,[2,3] and pressure sensors[4] owing to their light weight, large specific surface area, high thermal stability, and high electrical conductivity. Compressibility, elasticity, and fatigue resistance are the three key factors that determine the performance and applications of elastic carbon aerogels.[5,6] Owing to the highly porous structure of carbon aerogels, their high compressibility has been previously demonstrated.[7] However, recovery to their original height and stress upon cyclic compression has been rarely achieved owing to the brittleness of random carbon networks.[8] Therefore, achieving an elastic carbon aerogel with super-elasticity and fatigue resistance upon large cyclic compression strain is highly demanded for broadening the practical applications, which include elastic cushioning systems for vehicles and shoes to minimize mechanical shock, and wide-range pressure sensors for wearable electronics.

Tailoring of the carbon precursor, carbonization conditions, and microstructure has been exploited to fabricate elastic carbon aerogels. Fossil-derived one-dimensional, two-dimensional, and related carbon materials such as carbon nanotubes (CNTs),[9] graphene,[7] and CNTs/graphene composite aerogels[5] notably comprised continuous and crosslinked stacked networks as soft and flexible cell walls, preventing buckling and/or fracture upon cyclic compression. The replacement of these fossil-derived carbons with thermally or hydrothermally carbonized biomass (polysaccharides,[10] lignin,[11] and protein[12]) offers a remarkable strategy for fabricating sustainable carbon aerogels. Nonetheless, carbonization causes severe weight loss and volume shrinkage of the biomass-derived precursors, resulting in lower elasticity and fatigue resistance of the carbonized biomass aerogels compared to fossil-derived carbon aerogels.[13] To address this problem, Peng et al. developed a cellulose nanofiber/lignin-derived composite carbon aerogel;[11] the lignin acted as a “glue” that prevented the high volume and shape shrinkage of the cellulose nanofiber, thus realizing an enhancement in elasticity and fatigue resistance of 30,000 cycles at 50% compression strain. Nevertheless, despite this development, there remains a demand for further investigation of biomass-derived precursors and their carbonization conditions to develop carbonized biomass aerogels with super-elasticity and fatigue resistance under severe compression strains.

The rational design of microstructures is another attractive research avenue for developing

elastic carbon aerogels.[14] Specifically, anisotropic microstructure designs such as cellular-like,[15] lamellar-like,[16] wood-like,[17] and honeycomb-like[3] anisotropic microstructures could maximize the elasticity and fatigue resistance of the aerogels in the direction perpendicular to the anisotropic microstructures. Inspired by natural honeycombs and their anisotropic microstructures,[18] it has been verified that honeycomb-structured aerogels exhibited apparent densities similar to those of typical aerogels,[19] but were structurally robust because the cell walls were closely connected and formed a "Steiner tree" geometry.[20] This could efficiently dissipate mechanical strength and guide the deformation, thus avoiding locally large deformation and structural failure.[21] For example, Ding et al. developed an elastic composite carbon aerogel with anisotropic "Steiner tree" microstructures based on carbonized konjac glucomannan and SiO_2 nanofibers.[13] Notably, the thermally stable and mechanically robust SiO_2 nanofibrous networks within the microstructures could be defoamed flexibly to dissipate mechanical strength and avoid the stress concentration, thereby imparting the composite carbon aerogel with super cyclable compressibility.[13] However, the rational design of anisotropic microstructures with nanofibrous networks in carbonized biomass aerogels remains a challenge, because bio-nanofibers frequently suffer from severe collapse of their original morphologies upon carbonization.[22]

Cellulose and chitin nanofibers are the two most abundant bio-nanofibers on earth. While cellulose nanofibers inevitably collapse their original morphologies during high-temperature carbonization, chitin nanofibers reportedly exhibit higher morphological stability than cellulose nanofibers against carbonization.[22,23] Therefore, chitin nanofiber has the potential to be an ideal precursor for the fabrication of carbonized biomass aerogels with well-designed microstructures with nanofibrous networks. Although chitin nanofiber-derived carbons have previously been reported,[24,25,26] their fabrication processes and the conditions required to boost their elastic properties have not yet been systematically explored. Thus, we propose that chitin nanofiber-derived carbon tailored with honeycomb-like anisotropic microstructures and nanofibrous networks, if realized, could achieve super-elasticity and fatigue resistance under large cyclic compression.

In this study, a chitin nanofiber-derived carbon aerogel with honeycomb-like anisotropic microstructures and nanofibrous networks (denoted as chitin nanofiber-derived carbon honeycomb) was fabricated from a chitin nanofiber/water suspension *via* unidirectional freeze-drying and subsequent carbonization. The chitin nanofiber concentration and carbonization temperature were optimized to impart the chitin nanofiber-derived carbon honeycomb with super-compressibility, super-elasticity, and robustness. The optimized carbon honeycomb

exhibited excellent elasticity as well as fatigue resistance even at 90% compression strain. The elasticity of the carbon honeycomb was maintained even when exposed to flame and liquid nitrogen, owing to its high thermal and mechanical stability. Owing to these features, the carbon honeycomb offered high pressure sensitivity over an ultrawide range of working pressures and temperatures.

3.2 Experimental section

3.2.1 Fabrication of the chitin nanofiber-derived carbon honeycombs

Based on our previous report,[42] chitin nanofiber-derived carbon honeycombs were fabricated *via* unidirectional ice-templating, freeze-drying, and subsequent carbonization (**Fig. 3-1a**). In brief, chitin nanofiber/water suspensions (24 mL, BiNFi-s chitin, SFo-20002, Sugino Machine, Ltd., Namerikawa, Japan) with controlled chitin nanofiber concentrations (0.6, 0.8, 1.0, and 1.2 wt.%) were defoamed using a centrifugal vacuum apparatus (ARV-930TWIN, Thinky Corp., Tokyo, Japan) at 1400 rpm at 25 °C for 5 min. The as-defoamed suspensions were then poured into boxes (length = 40 mm, width = 30 mm, depth = 20 mm) made of acrylic plates (thickness = 1.0 mm; AcrySunday Co. Ltd., Osaka, Japan); in each box, an inner wall (length = 40 mm, thickness = 20 mm) was pre-attached using adhesive Cu foil (No. 8701-00, Maxell Sliontec Ltd., Kanagawa, Japan). Subsequently, the chitin nanofiber/water suspension-filled acrylic boxes (with the Cu side) were attached to a liquid nitrogen-filled open steel box for unidirectional ice-templating, followed by freeze drying below −90 °C and 5.0 Pa for 60 h using a freeze dryer (EYELA FDU-2200, Tokyo Rikakikai Co. Ltd., Tokyo, Japan). The resulting chitin nanofiber-derived honeycombs were carbonized in a temperature-programmable muffle furnace (KDF75, Denken Highdental Co., Ltd. Kyoto, Japan) in three stages: (1) the honeycombs were heated from 25 to 500 °C at a heating rate of 2 °C min^{-1}, and the temperature was maintained for 2 h; (2) the temperature was increased to the target carbonization temperature (600, 700, 800, 900, or 1000 °C) at a heating rate of 5 °C min^{-1} and maintained for 1 h; (3) the carbonized honeycombs were cooled to 25 °C at 2 °C min^{-1}. Carbonization was performed in a nitrogen atmosphere.

3.2.2 Evaluation of the elastic properties of chitin nanofiber-derived carbon honeycombs

The elastic properties of the chitin nanofiber-derived carbon honeycombs were evaluated using a compression testing apparatus equipped with a 500-N load cell (EZ-SX, Shimadzu Co. Ltd., Osaka, Japan). The carbon honeycomb was first cut into a cuboidal shape (typical size: length = 15 mm, width = 15 mm, thickness = 10 mm) and set between the two compression

stages; the top stage was moved to apply and release uniaxial compression force on the carbon honeycomb. The loading and unloading directions were perpendicular to the anisotropic channels of the carbon honeycombs. Hysteresis curves with maximum strains of 40, 60, 70, 80, and 90% were measured at a stroke rate of 10 mm min^{-1} at 25 °C. Elastic property measurements at ultra-high and ultra-low temperatures were also performed by exposing the carbon honeycombs to a butane blowlamp flame (approximately 1000 °C; Shinfuji Burner Co. Ltd. Aichi, Japan) and liquid nitrogen (approximately −196 °C), respectively. For the measurement of fatigue resistance during 10,000 cycles of 60%, 70%, 80%, and 90% compression and release, continuous cyclic compression was performed on the carbon honeycomb with a compression frequency of 0.4 Hz using a Desktop Model Endurance Testing Machine (DLDM111LHB, YUASA System Co. Ltd. Okayama, Japan). The stress and height retention values of the carbon honeycombs were calculated by dividing the stress and height at each cycle by those of the original state.

3.2.3 Evaluation of the pressure sensing performance of chitin nanofiber-derived carbon honeycombs

A carbon honeycomb-based pressure sensor was fabricated as follows. The carbon honeycomb was first cut into a cuboid (typical size: length = 15 mm, width = 15 mm, thickness = 10 mm) and sandwiched between two Cu foil electrodes that were pre-adhered to a glass plate (thickness = 1 mm; Matsunami Glass Ind., Ltd., Osaka, Japan). The pressure-sensing performance of the carbon honeycomb was evaluated using a universal compression testing machine (MCT-1150, AND Co., Ltd., Tokyo, Japan) and an electrochemical workstation (ModuLab XM, Solartron Analytical, AMETEK Advanced Measurement Technology Inc., Berkshire, UK) at an applied voltage of 1 V. The pressure-sensing performances of the sensor at ultrahigh and ultralow temperatures were measured while exposing the carbon honeycombs to an alcohol lamp flame (approximately 600 °C; Maruemu Corp., Osaka, Japan) and liquid nitrogen (approximately –196 °C), respectively.

The relative current change ($\Delta I/I_0$) upon applying pressures was calculated using **Equation 3.1**.

$$\Delta I/I_0 = (I - I_0)/I_0 \quad (3.1)$$

where I_0 (mA) is the initial current without pressure and I (mA) is the current at the applied pressure. The pressure sensitivity (S, kPa^{-1}) was calculated using **Equation 3.2**:

$$S = \delta(\Delta I/I_0)/\delta P \quad (3.2)$$

where $\delta(\Delta I/I_0)$ is the change in $\Delta I/I_0$, and δP (kPa) is the change in the applied pressure.

3.2.4 Characterization

The morphologies of the carbon honeycombs were observed using an FE-SEM machine (SU-8000, Hitachi High-Tech Science Corp., Tokyo, Japan) at an acceleration voltage of 2 kV. Prior to FE-SEM observation, the carbon honeycombs were subjected to platinum sputtering at 20 mA for 10 s (ION SPUTTER, E-1045, Hitachi High-Tech Science Corp. Tokyo, Japan). The thicknesses of the channel walls of the carbon honeycombs were measured from the FE-SEM images using ImageJ software (USA). Elemental analysis was performed using an organic trace element analysis device (JM10, J-Science Lab Co., Ltd., Kyoto, Japan). FT-IR spectra were obtained using a KJP-05120S instrument (PerkinElmer Japan Co. Ltd., Kanagawa, Japan). The temperature was measured using a temperature meter (MT-309, MotherTool Co., Ltd. Nagano, Japan) with a wide-range temperature probe (Saveris T3, TESTO, SE & Co. KGaA, Titisee-Neustadt, Germany).

3.3 Results and discussion

3.3.1 Preparation and morphology of the chitin nanofiber-derived carbon honeycombs

To realize chitin nanofiber-derived carbon with nanofibrous networks and anisotropic microstructures similar to those of a honeycomb, a fabrication strategy is proposed based on the workflow illustrated in **Fig. 3-1a**. Starting from a chitin nanofiber/water suspension, the carbon honeycomb was fabricated *via* unidirectional ice-templating, freeze drying, and subsequent carbonization. Chitin nanofiber/water suspensions with concentrations of 0.6, 0.8, 1.0, and 1.2 wt.% were prepared to tune the honeycomb microstructures. Owing to the unidirectional temperature

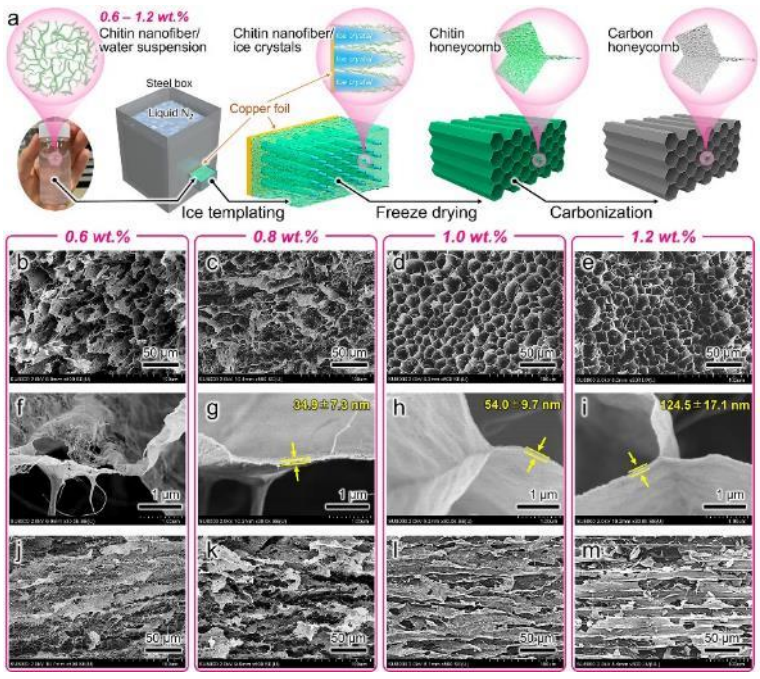


Fig. 3-1 Fabrication and morphology of the chitin nanofiber-derived carbon honeycombs. (a) Schematic of the preparation. FE-SEM images in the (b–i) parallel and (j–k) perpendicular directions of the anisotropic porous channels of the carbon honeycombs prepared at chitin nanofiber concentrations of (b, f, j) 0.6, (c, g, k) 0.8, (d, h, l) 1.0, and (e, i, m) 1.2 wt.%. Carbonization temperature: 900 °C.

gradient, the prism-shaped ice crystals grew vertically on the Cu foil and adjacent to one another. The adjacent ice crystals compel the chitin nanofiber to form a continuous nanofibrous network as the honeycomb channel walls. After eliminating the prism-shaped ice crystals by freeze-drying and carbonization, anisotropic honeycomb channels were obtained.

Field emission scanning electron microscopy (FE-SEM) was performed to investigate the anisotropic honeycomb channels and channel walls. As shown in **Fig. 3-1b–c**, at chitin nanofiber concentrations lower than 0.8 wt.%, the carbon honeycomb shows disorderly porous structures, implying that anisotropic honeycomb channels are hardly formed at low chitin nanofiber concentrations. Upon increasing the chitin nanofiber concentration to 1.0 wt.%, anisotropic honeycomb channels are formed successfully (**Fig. 3-1d–e**). Notably, the honeycomb channel walls are composed of nanofibrous networks. It can be observed from the high magnification FE-SEM images (**Fig. 3-1f–i**) that when the chitin nanofiber concentration is 0.6 wt.%, numerous in-plane pores are formed within the nanofibrous networks (**Fig. 3-1f**). With an increase in concentration from 0.8 to 1.2 wt.%, the nanofibrous networks become densely stacked, with the stacking thickness increasing from 34.9 to 124.5 nm (**Fig. 3-1g–i**); the detailed thickness distribution is summarized in **Fig. 3-2**. In addition, highly ordered straight channels are observed in the side view of the carbon honeycomb (**Fig. 3-1j–m**), indicating the successful formation of anisotropic honeycomb channels. Therefore, it was found that the microstructures varied with the chitin nanofiber concentration. A concentration of more than 1.0 wt.% is necessary for fabricating anisotropic honeycomb channels and nanofibrous network channel walls.

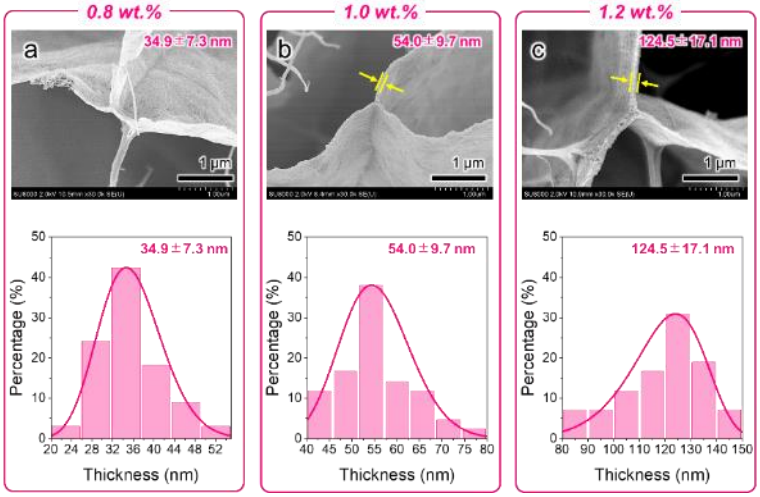


Fig. 3-2 FE-SEM images and channel-wall thickness distribution of chitin nanofiber-derived carbon honeycombs prepared at varied chitin nanofiber concentrations of (a) 0.8, (b) 1.0, and (c) 1.2 wt.% and a carbonization temperature of 900 °C.

3.3.2 Elastic properties of the chitin nanofiber-derived carbon honeycombs prepared at different chitin nanofiber concentrations

To demonstrate the superiority of the designed anisotropic honeycomb channels and channel walls, the elastic properties of carbon honeycombs prepared at different chitin nanofiber

concentrations and a carbonization temperature of 900 °C are evaluated under successive cyclic compression up to 80% strain (**Fig. 3-3a**). Notably, the chitin honeycomb that did not undergo carbonization does not deform elastically. The carbon honeycomb fabricated at a concentration lower than 0.8 wt.% exhibits remarkable plastic deformation (**Fig. 3-4a–b**) with a maximum stress of less than 20.0 kPa (**Fig. 3-3b**) and a height retention of less than 91% (**Fig. 3-3c**) after 10 compression cycles. This indicates that the carbon honeycombs without anisotropic honeycomb channels (Fig. 3-1b–c) and sufficiently connected channel walls (Fig. 3-1j–k) are too brittle to resist compression.

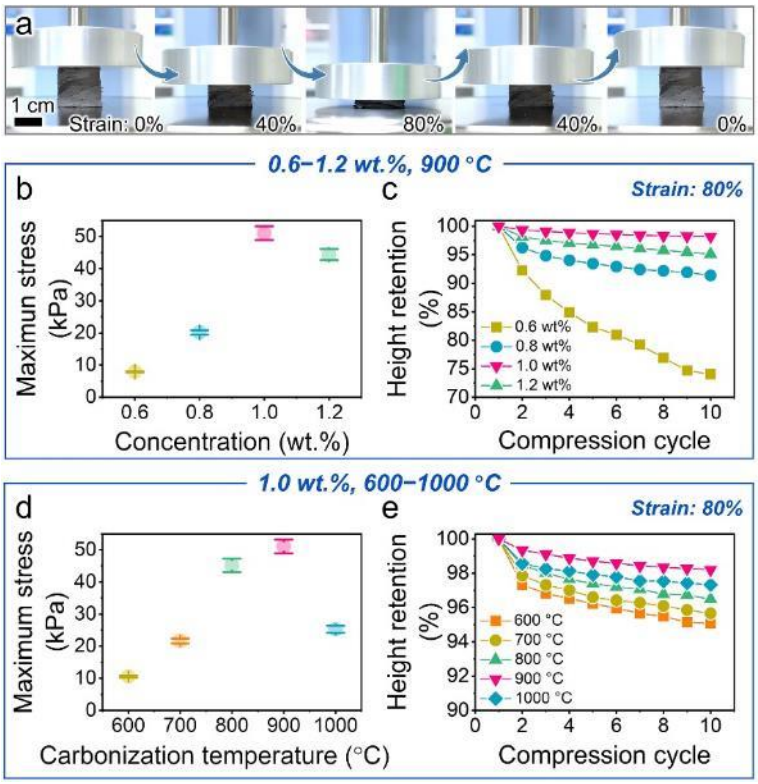


Fig. 3-3 Elastic properties of the chitin nanofiber-derived carbon honeycombs. (a) Optical images of the carbon honeycomb under strain ranging from 0 to 80% during compression loading and unloading. (b) Maximum stress and (c) height retention versus compression cycle of the carbon honeycombs prepared at varied chitin nanofiber concentrations of 0.6, 0.8, 1.0, and 1.2 wt.%, and a carbonization temperature of 900 °C. (d) Maximum stress and (e) height retention versus compression cycle of the carbon honeycombs prepared at a chitin nanofiber concentration of 1.0 wt.% and varied carbonization temperatures of 600, 700, 800, 900, and 1000 °C.

In contrast, the carbon honeycomb with 1.0 wt.% chitin nanofiber concentration exhibits an enhanced maximum stress of 51.0 kPa and height retention of 98.2% (Fig. 3-3b–c), which indicates that the anisotropic honeycomb channels, which have wall thicknesses of approximately 54.0 ± 9.7 nm (Fig. 3-1h), are robust but flexible to resist the compression and recover completely (**Fig. 3-4c**). The carbon honeycomb with 1.2 wt.% chitin nanofiber concentration also shows a high-stress value, similar to that of the carbon honeycomb at 1.0 wt.%, owing to the formation of anisotropic honeycomb channels. However, its retention decreases to 95.1% (Fig. 3-3c), and brittle breakage occurs during cyclic compression (**Fig. 3-4d**). This is because the thick channel walls (thickness = 124.5 ± 17.1 nm) (Fig. 3-1i) with densely stacked carbon nanofibers suffer higher stress concentration, resulting in fragile breakage and poor elasticity.[11] Thus, elastic properties are realized for chitin nanofiber-derived

carbon honeycomb tailored by tuning the anisotropic honeycomb channels and channel wall thicknesses by using a chitin nanofiber concentration of 1.0 wt.%.

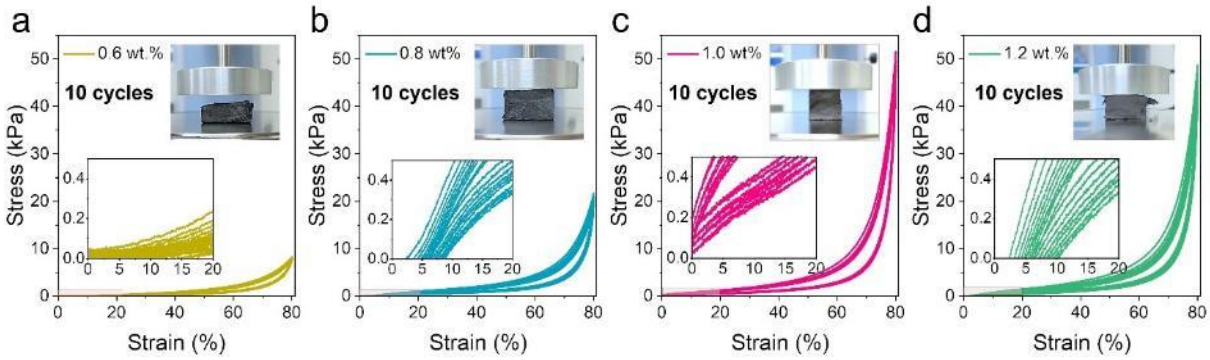


Fig. 3-4 Stress–strain curves during compression loading and unloading at a strain of 80% for chitin nanofiber-derived carbon honeycombs prepared at chitin nanofiber concentrations of (a) 0.6, (b) 0.8, (c) 1.0, and (d) 1.2 wt.% and a carbonization temperature of 900 °C.

3.3.3 Elastic properties of the chitin nanofiber-derived carbon honeycombs prepared at different carbonization temperatures

Based on a chitin nanofiber concentration of 1.0 wt.%, the effect of the carbonization temperature was further investigated to tailor the honeycomb channel walls and carbon-based

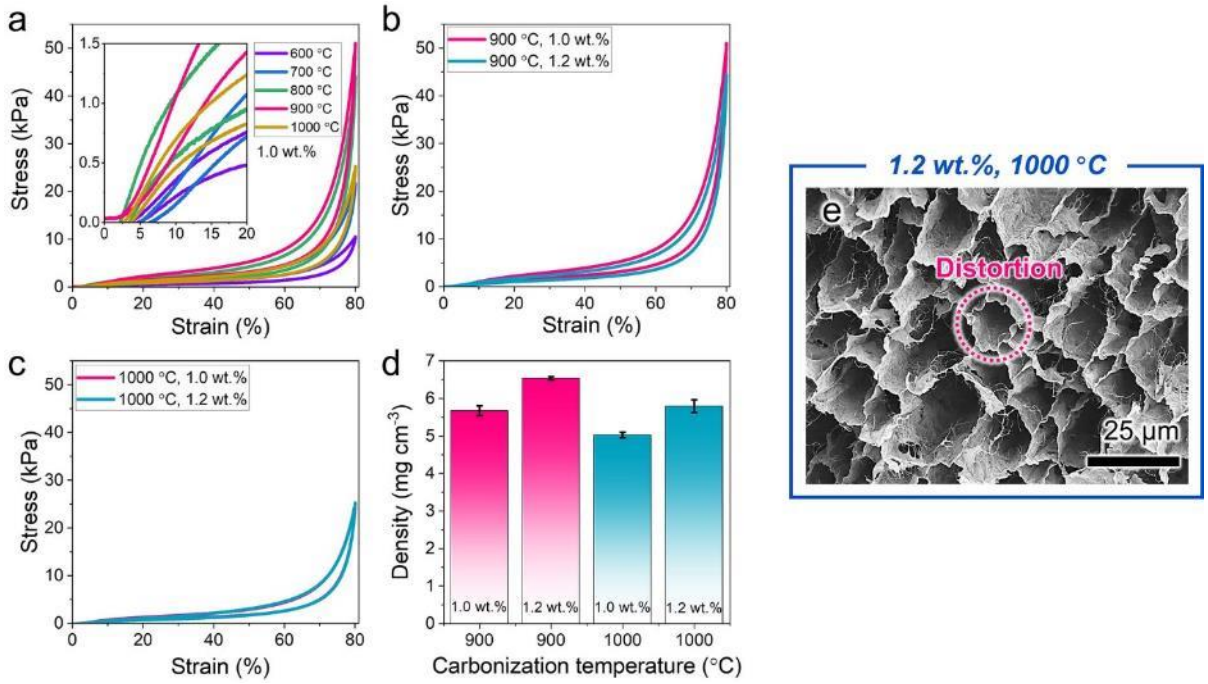


Fig. 3-5 Stress–strain curves during compression loading and unloading at a strain of 80% for chitin nanofiber-derived carbon honeycombs prepared at: (a) a chitin nanofiber concentration of 1.0 wt.% and varied carbonization temperatures of 600, 700, 800, 900, and 1000 °C, (b) varied chitin nanofiber concentrations of 1.0 and 1.2 wt.% and a carbonization temperature of 900 °C,

and (c) varied chitin nanofiber concentrations of 1.0 and 1.2 wt.% and a carbonization temperature of 1000 °C. (d) Density of the carbon honeycombs prepared at varied chitin nanofiber concentrations of 1.0 and 1.2 wt.% and varied carbonization temperatures of 900 and 1000 °C. (e) An FE-SEM image of the carbon honeycomb prepared at a chitin nanofiber concentration of 1.2 wt.% and a carbonization temperature of 1000 °C.

molecular structures, which can optimize the elasticity of the carbon honeycomb. As shown in Fig. 3-3d–e, the carbon honeycomb carbonized at 900 °C exhibits the highest stress and height retention after 10 compression cycles at 80% strain. The stress remains above 0 kPa until the strain reaches 0% in the unloading process (**Fig. 3-5a**), indicating a complete recovery.[5] The carbon honeycombs carbonized at temperatures lower than 800 °C exhibit low maximum stress and height retention, where the stress is reduced to 0 kPa before the strain returns to 0% after 10 cycles of compression (Fig. 3-5a), representing the poor elasticity and permanent plastic deformation at low carbonization temperatures. At a carbonization temperature of 1000 °C, the stress on the carbon honeycomb decreases significantly (Fig. 3-3d and 3-5c).

The elasticity of the chitin nanofiber-derived carbon honeycombs upon carbonization can be understood by analyzing its honeycomb channel walls and their thicknesses, and carbon-based molecular structures. As shown in **Fig. 3-6a** and **Fig. 3-7**, when the chitin nanofiber concentration is 1.0 wt.%, the obtained honeycomb channel-wall thicknesses are approximately 68.9 ± 8.1, 65.2 ± 5.8, 61.2 ± 9.6, 54.0 ± 9.7, and 49.3 ± 8.6 nm at carbonization

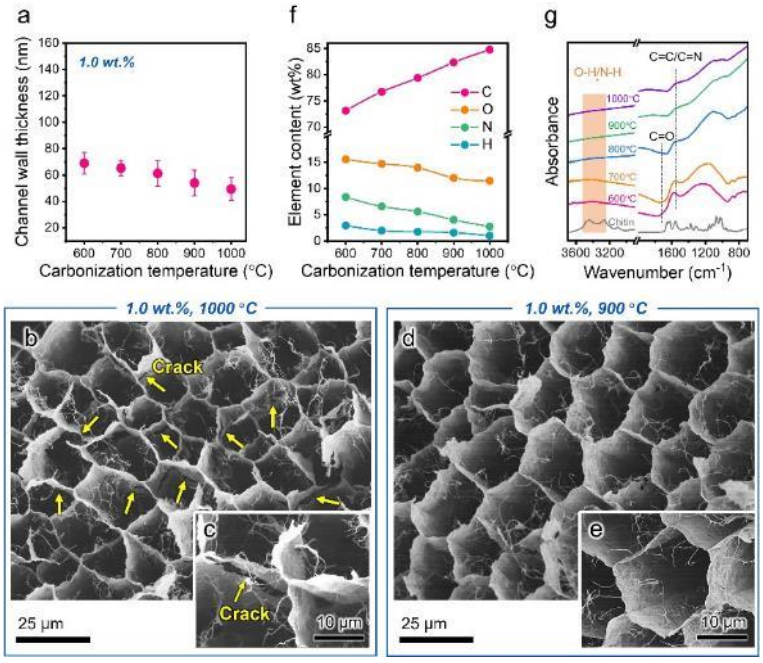


Fig. 3-6 Honeycomb channel walls and their thickness, and carbon-based molecular structure characterization for the chitin nanofiber-derived carbon honeycombs. (a) Channel wall thickness of the chitin nanofiber-derived carbon honeycombs as a function of carbonization temperature. FE-SEM images of the chitin nanofiber-derived carbon honeycombs prepared at a chitin nanofiber concentration of 1.0 wt.% and varied carbonization temperatures of (b–c) 1000 °C and (d–e) 900 °C. (f) Elemental content and (g) FT-IR spectra of the chitin nanofiber-derived carbon honeycombs prepared at a chitin nanofiber concentration of 1.0 wt.% and varied carbonization temperatures from 600 to 1000 °C.

temperatures of 600, 700, 800, 900, and 1000 °C, respectively, implying that a gradual decrease in thickness might be a factor for the increase in elasticity with increasing carbonization temperature.[11] However, the honeycomb carbonized at 1000 °C showed lower elasticity than that carbonized at 900 °C (Fig. 3-3d–e and 3-5b–c). This is possibly due to the weight loss that occurs upon carbonization at 1000 °C, owing to which the density is only 5.0 mg cm^{-3} (Fig. 3-5d), causing the honeycomb channel walls to crack (**Fig. 3-6b–c**) after carbonization, thus resulting in weakened elasticity. In contrast, such cracks are not observed in the honeycomb carbonized at 900 °C (**Fig. 3-6d–e**), showing good elasticity. These results suggest that a carbonization temperature of 900 °C is preferred for the production of elastic carbon honeycombs based on chitin nanofiber, as a higher carbonization temperature of 1000 °C results in lower density of the carbon honeycomb. The chitin nanofiber-derived honeycomb carbonized at 1000 °C with 1.2 wt.% chitin nanofiber concentration has a similar density of 5.79 mg cm^{-3} to that of the honeycomb carbonized at 900 °C with 1.0 wt.% chitin nanofiber concentration (5.72 mg cm^{-3}) (Fig. 3-5d). However, the honeycomb channel walls carbonized at 1000 °C are distorted (Fig. 3-5e), which would also result in poor elasticity upon compression (Fig. 3-5c).

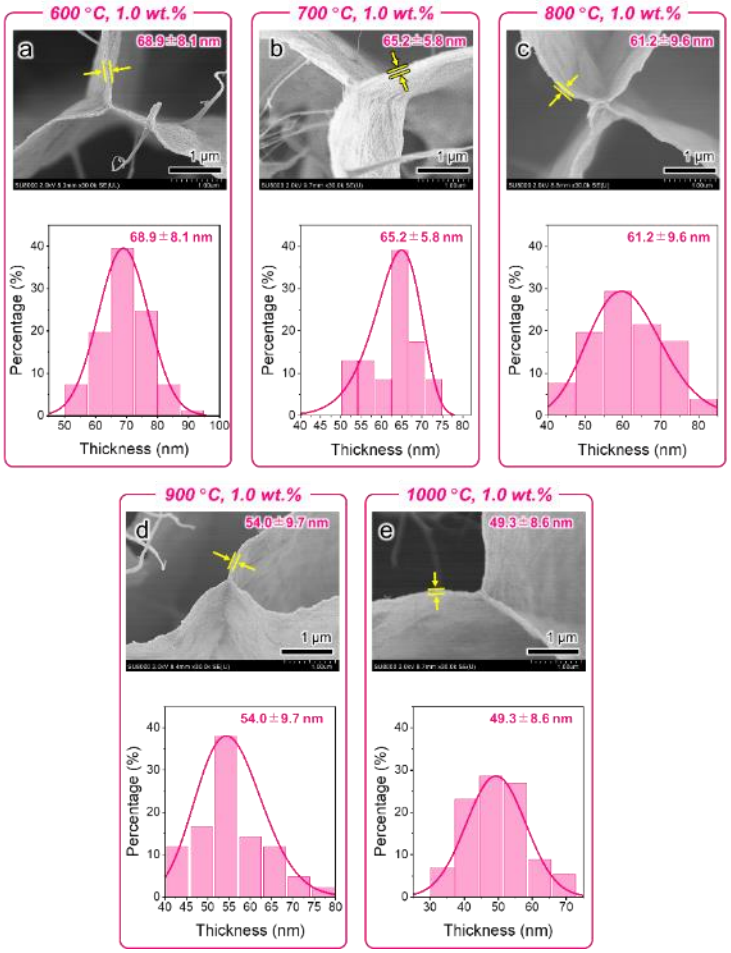


Fig. 3-7 FE-SEM images and channel wall thickness distribution of chitin nanofiber-derived

carbon honeycombs prepared at a chitin nanofiber concentration of 1.0 wt.% and varied carbonization temperatures of (a) 600, (b) 700, (c) 800, (d) 900, and (e) 1000 °C.

For the carbon-based molecular structures, elemental analysis suggests that the C content increases from 73.15 to 84.75 wt.% with increasing carbonization temperature from 600 to 1000 °C, while the O, N, and H contents gradually decrease from 15.54 to 11.47 wt.%, 8.36 to 2.77 wt.%, and 2.95 to 1.01 wt.%, respectively, indicating that O, N, and H are gradually removed from the carbon honeycomb (**Fig. 3-6f**). The Fourier-transform infrared (FT-IR) spectra show that the O−H and N−H characteristic peaks gradually decrease with increasing carbonization temperatures from 600 to 1000 °C (**Fig. 3-6g**), similar to the tendency for the enhancement of elasticity from 600 to 900 °C. Due to the gradual removal of the H, N, and O elements, the hydrogen bonding provided by O−H and N−H was significantly weakened after carbonization.[27] This implies that the weak hydrogen-bonding interactions between the carbonized chitin nanofiber play an important role in enhancing the elasticity of the carbon honeycomb, as reported for cellulose nanofiber materials.[28,29] Despite the hydrogen bonding interactions between the carbonized chitin nanofiber being weak, the honeycomb carbonized at 1000 °C shows low elasticity, due to the formation of cracks within its thin channel walls by the occurrence of sever weight loss.

Therefore, it is reasonable to conclude that the chitin nanofiber-derived carbon honeycomb with 1.0 wt.% chitin nanofiber concentration and 900 °C carbonization temperature has excellent elasticity owing to the desirable anisotropic honeycomb channels with fewer cracks and weak hydrogen-bonding interactions between carbonized chitin nanofibers. The anisotropic honeycomb channels are mechanically robust, providing a structure with high compressibility and good recovery. The weak hydrogen-bonding interactions between the carbonized chitin nanofiber effectively mitigate the stickiness of the carbon honeycomb, thus dissipating the compression stress concentration and guiding the deformation of the microstructures to avoid structural failure during compression and recovery.

3.3.4 Fatigue resistance of the chitin nanofiber-derived carbon honeycombs

The optimized elastic carbon honeycomb was subjected to compression–release cycles at compression strains starting from 60% to test its fatigue resistance. As shown in **Fig. 3-8a**, the carbon honeycomb shows almost overlapping strain–stress curves at a maximum strain of 60%, confirming its elasticity over 10,000 cycles of compression. Notably, stress and height retentions of 95% and 97.5%, respectively, are achieved by the elastic carbon honeycomb after 10,000 cycles of compression at 60% strain (**Fig. 3-8e–f**), indicating negligible changes in

elasticity. After compression for 10,000 cycles at strain levels of 70% and 80% (**Fig. 3-8b–c**), the carbon honeycomb maintains over 91% of the maximum stress and 96% of the maximum height (Fig. 3-8e–f). These results illustrate that the carbon honeycomb reported herein can tolerate large elastic deformations (within 80% strain) without undergoing damage or structural collapse. Moreover, even under a more severe compression strain of 90% over 10,000 cycles (**Fig. 3-8d**), the carbon honeycomb exhibits stress and height retentions of up to 87% and 94%, respectively; the height reduction occurs mainly in the earlier cycles, and the structure becomes relatively stable in the subsequent cycles (Fig. 3-8f). As summarized in **Fig. 3-8g**, the carbonization of chitin nanofiber-based anisotropic honeycomb channels is a promising strategy for fabricating carbon honeycombs that, under large compression strains, can exhibit super-elasticity comparable to that of state-of-the-art carbon aerogels derived from mechanically robust sources such as fossil-derived carbons,[7,15,30,31,32] MXenes,[33] and biomass-derived composites.[11,13,14,34,35,36] Comparing the results of the previous works with those of the present study, it can be seen that the maximum compressions of the former are mostly within the limit of 80% strain, and the resulting stress and height retention are less than 75% and 93%, respectively. The higher values of the present study confirm that the tailored chitin nanofiber-derived carbon honeycombs have high fatigue resistance under large compression strains.

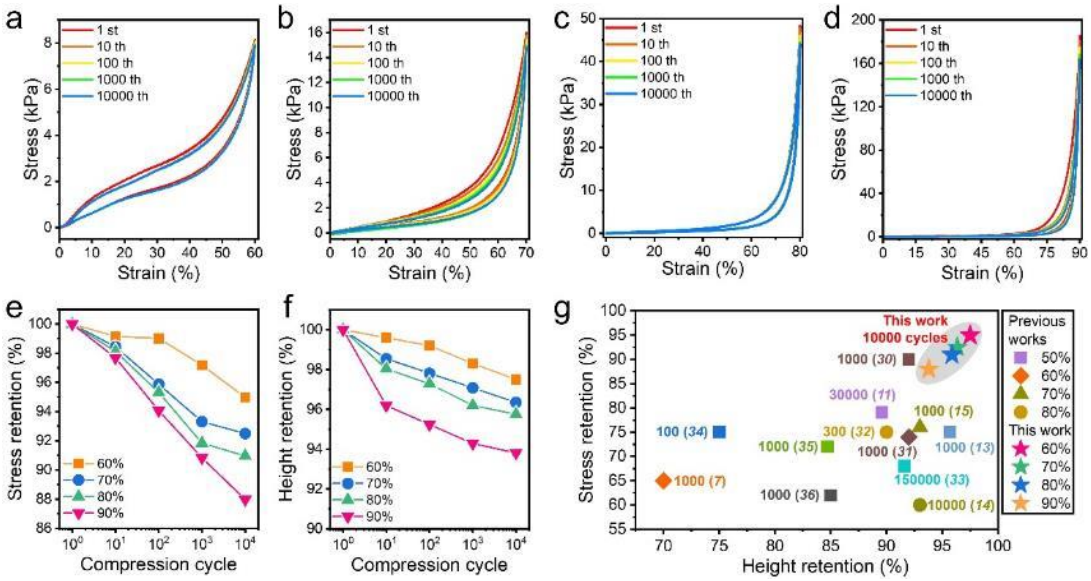


Fig. 3-8 Fatigue resistance of the carbon honeycomb prepared at a chitin nanofiber concentration of 1.0 wt.% and a carbonization temperature of 900 °C. Stress–strain curves of the carbon honeycombs during compression loading and unloading at (a) 60, (b) 70, (c) 80, and (d) 90% strain for 10,000 cycles of compression. (e) Stress and (f) height retention during 10,000 cycles of compression at 60, 70, 80, and 90% strain. (g) Comparison of stress and height retention of chitin nanofiber-derived elastic carbon honeycomb with previously reported carbon

materials. Compression cycle numbers are included beside the corresponding dots in the chart. Numbers in parentheses refer to relevant references. The percentages shown in the legend represent the relevant compression strain for each study.

3.3.5 Application of the chitin nanofiber-derived carbon honeycombs in pressure sensing

The excellent compressibility, elasticity, and fatigue resistance of the chitin nanofiber-derived carbon honeycomb at 90% strain makes it a promising candidate for application in flexible electronics such as pressure sensors. As shown in **Fig. 3-9a**, the real-time LED brightness achieved by the elastic carbon honeycombs changes with the compression strain, indicating that the electrical conductivity of the carbon honeycombs changes sensitively with compression. **Fig. 3-9b** shows the real-time current responses of the carbon honeycombs for six cycles at compression strains of 20, 40, 60, and 90%. Each peak corresponds to one cycle of compression and release. The current increases considerably during compression and decreases rapidly during release, indicating the rapid current response of the elastic carbon honeycombs under compression. Furthermore, the maximum current intensity increases continuously with increasing pressure, demonstrating the potential applicability of the carbon honeycomb for pressure sensing.

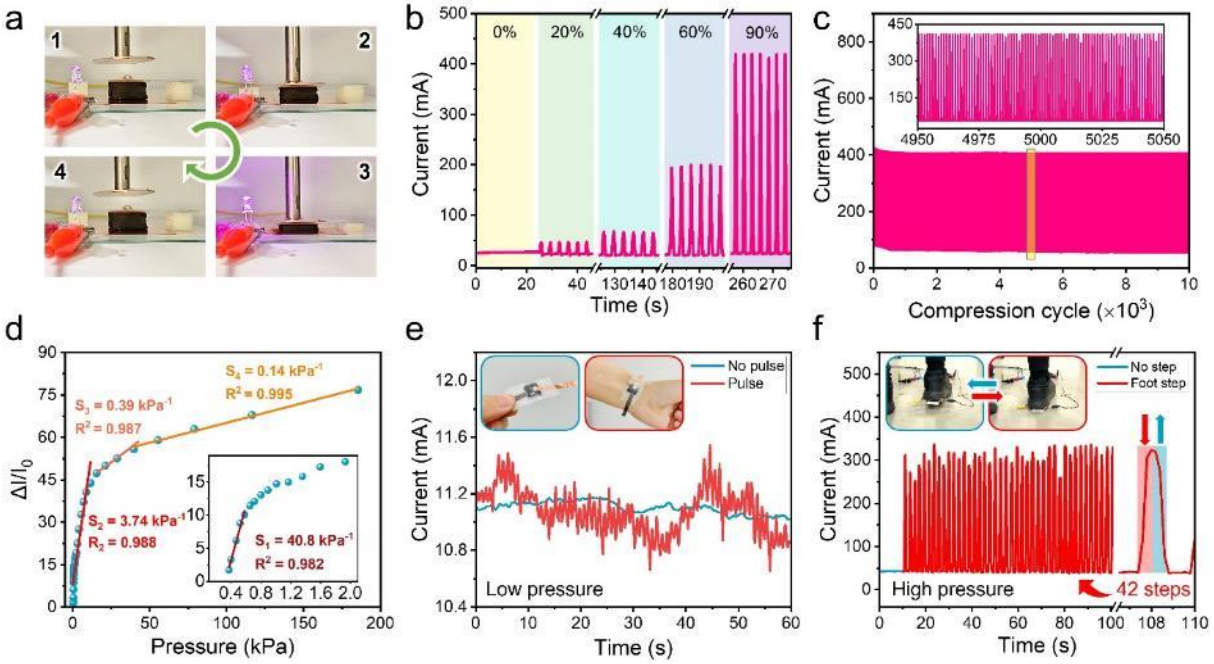


Fig. 3-9 Pressure sensing performance of the chitin nanofiber-derived carbon honeycomb. (a) The brightness of the LED is controlled by applying different pressures. (b) Current response at different compression strains from 0 to 90%. (c) Current response at a compression strain of 90% during 10,000 cycles. (d) Relative current change ($\Delta I/I_0$) and pressure sensitivity (S) over

a wide pressure range from 0 to 185.5 kPa. Changes in the current response of the carbon-honeycomb-based pressure sensor during the monitoring of human behavior: (e) low-pressure pulse vibration and (f) high-pressure footsteps. Chitin nanofiber concentration: 1.0 wt.%. Carbonization temperature: 900 °C.

The linear I–V curves (voltage range: −1 to 1 V) of the carbon honeycomb further suggest that its resistance is stable under different pressures (**Fig. 3-10**). Furthermore, the current response of the elastic carbon-honeycomb-based pressure sensor remains at almost the same amplitude, without any substantial change after 10,000 cycles at 90% strain (**Fig. 3-9c**), indicating its excellent current response stability. **Fig. 3-9d** shows the calculated pressure sensitivity. Specifically, the elastic carbon honeycomb exhibits four linear pressure sensitivities of 40.8 kPa^{-1} (0–0.58 kPa), 3.74 kPa^{-1} (0.58–11.5 kPa), 0.39 kPa^{-1} (11.5–39.7 kPa), and 0.14 kPa^{-1} (39.7–185.5 kPa), demonstrating high sensitivity toward small pressure changes over a broad range of pressures.

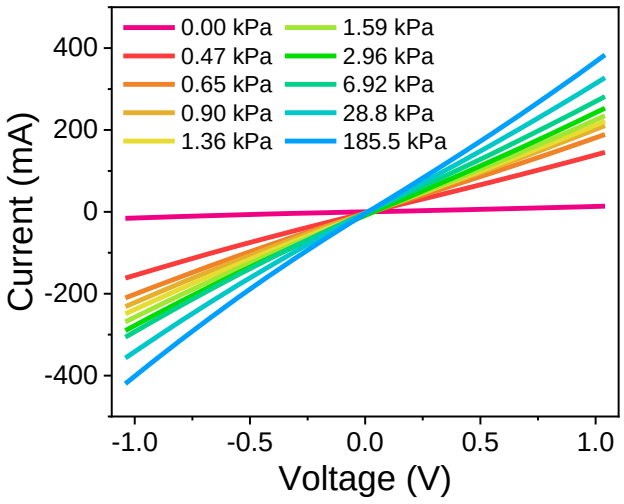


Fig. 3-10 I–V curves of the carbon honeycomb-based pressure sensor over a voltage range of –1 V to 1 V under various pressures, suggesting Ohmic contact characteristics between the carbon honeycomb and the electrodes. Chitin nanofiber concentration: 1.0 wt.%. Carbonization temperature: 900 °C.

Considering their exceptional sensitivity at both low and high pressures, the elastic carbon honeycombs were tested as wearable pressure sensors for detecting motions such as low-pressure pulse vibrations and high-pressure footsteps. As shown in **Fig. 3-9e**, the sensor current is stable at 11.1 mA when there is no pulse. By contrast, when detecting a pulse, the current profile exhibits regular peaks with time, with each peak corresponding to a single pulse. A total of 67 pulse vibrations are recorded in 60 s, which is within the normal heart rate range for adults. In addition, **Fig. 3-9f** shows that when the sensor is attached to the sole of a human foot, real-time current changes can be detected during walking. The minimum and maximum current responses for each step are stable at approximately 49 and 300 mA, respectively, indicating that the sensor is stable under heavy foot compression. These results indicate that the elastic carbon honeycomb is applicable for the detection of motion in terms of both small and large pressure changes.

The pressure-sensing performance was demonstrated *via* current changes, which entailed

monitoring the pressure-induced changes in the electrical conductivity of the elastic carbon honeycombs. The electrical conductivity of the carbon honeycombs depends on the point-to-point or point-to-plane contact numbers and the plane-to-plane contact area of the anisotropic honeycomb channels, which are elucidated as the following three key points: (i) in low-pressure regions, the electron conduction paths from one side to the other increase rapidly in the point-to-point or point-to-plane[37] form owing to the abundant free carbonized chitin nanofiber on the channel walls, thus imparting a high sensitivity (S_1: 40.8 kPa^{-1}) to pressure changes (**Fig. 3-11**); (ii) in medium-pressure regions, the electron conduction paths are gradually converted to the point-to-plane and plane-to-plane forms,[38] which are dominated by the contact area between the channel walls. With an increase in the contact area, the electron conduction path remains mostly unchanged, but the pressure variation rate gradually increases, thus exhibiting a decreased pressure sensitivity (S_2: 3.74 kPa^{-1}); and finally, (iii) in the high-pressure region, the electron conduction path is mainly determined by the plane-to-plane contact area,[39] wherein almost all channel walls are in contact with each other. As a result, the rate of variation of the plane-to-plane contact area between the channel walls decreases significantly, whereas the pressure variation rate drastically increases, weakening the electron conduction efficiency and pressure sensitivity (S_3: 0.39 kPa^{-1} and S_4: 0.14 kPa^{-1}).

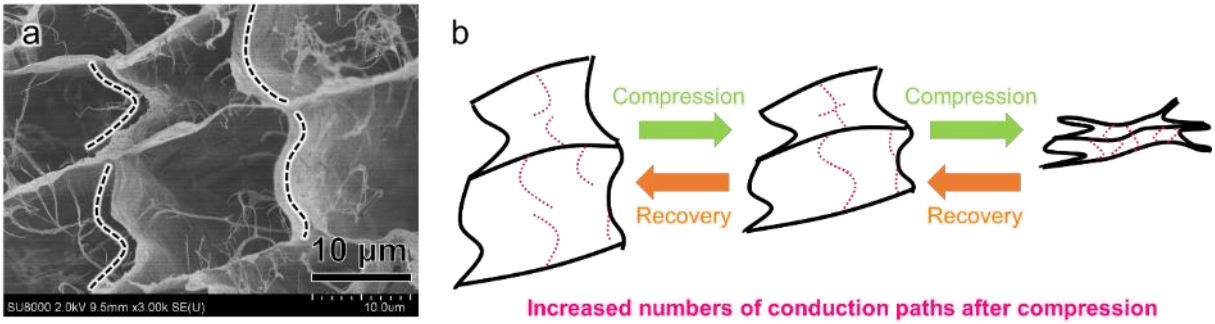


Fig. 3-11 (a) An FE-SEM image of the chitin nanofiber-derived carbon honeycomb in the direction parallel to the anisotropic honeycomb channels, showing the channel walls and free fibers outside them. (b) Schematic representation of the deformation of the honeycomb structures and increased numbers of electron conduction pathways during compression and release. Chitin nanofiber concentration: 1.0 wt.%. Carbonization temperature: 900 °C.

Excellent resistance to thermal shock is vital for the practical application of electronic devices in extreme environments such as ultra-high- or ultra-low-temperature environments. In this study, we explored the elastic properties of an optimized chitin nanofiber-derived carbon

honeycomb over a wide temperature range, such as in flames and liquid nitrogen. As shown in **Fig. 3-12a** and **Fig. 3-13**, the carbon honeycomb was nonflammable in the flames of a butane blowlamp (Approx. 1000 °C) and an alcohol lamp (Approx. 600 °C), indicating excellent fire resistance. An *in situ* compression test was performed to evaluate the elasticity of the carbon honeycomb in the flame. No significant stress reduction was observed when the carbon honeycomb was exposed to flame. Furthermore, when the carbon honeycomb was recovered to room temperature, the stress–strain curve overlapped with the original curve (**Fig. 3-12c**). This indicates the thermal stability and superelasticity of the carbon honeycomb at high temperatures. When the carbon honeycomb was placed in liquid nitrogen (−196 °C) (**Fig. 3-12b**), it again exhibited compressive and elastic behavior and could be compressed without obvious fracture and be recovered to its original shape. Notably, there was no significant deterioration in the mechanical properties of the carbon honeycombs compressed in liquid nitrogen (**Fig. 3-12d**), illustrating their excellent elasticity at low temperatures.

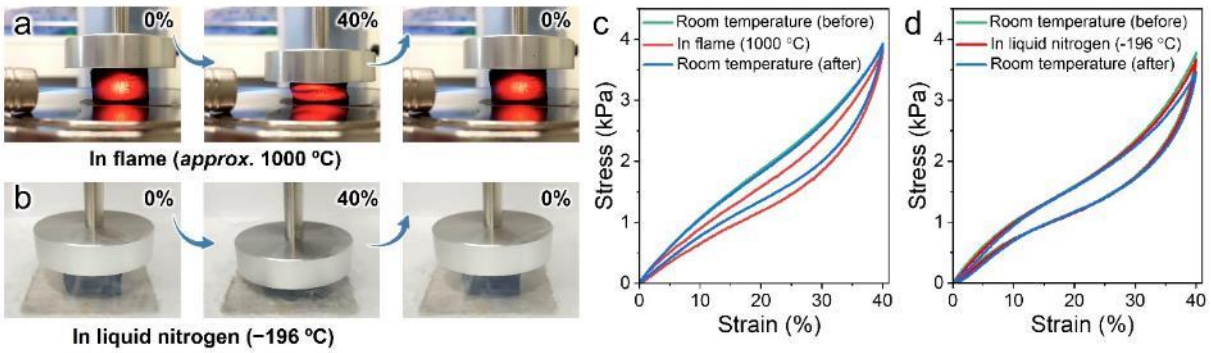


Fig. 3-12 Optical images of the carbon honeycomb during compression and release in (a) butane blowlamp flame and (b) liquid nitrogen. Stress–strain curves of the carbon honeycomb before, during, and after (c) butane blowlamp flame and (d) liquid nitrogen treatment. Chitin nanofiber concentration: 1.0 wt.%. Carbonization temperature: 900 °C.

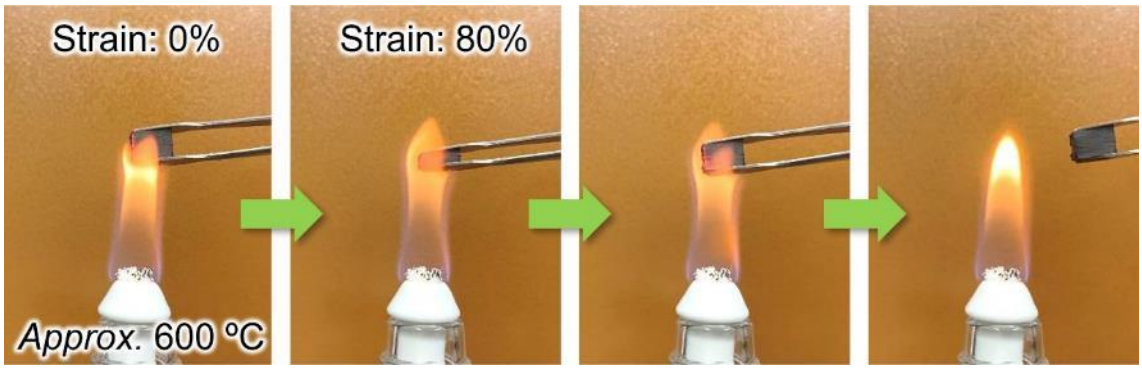


Fig. 3-13 Optical images of the chitin nanofiber-derived carbon honeycomb during compression and release in alcohol lamp flame with a temperature of approximately 600 °C. Chitin nanofiber concentration: 1.0 wt.%. Carbonization temperature: 900 °C.

These results suggest that the chitin nanofiber-derived carbon honeycomb exhibits excellent elasticity even in flame and liquid nitrogen. The elasticity in the flames was possibly due to the fire-retardant properties of the N-doped carbon molecule structure as well as the high porosity of the chitin nanofiber-derived carbon honeycomb that allowed for the quick removal of heat; thus, the honeycomb-like anisotropic porous structures could be preserved, resulting in elastic deformation. In liquid nitrogen, the carbon honeycomb was hydrophobic and had weak hydrogen bonding between the carbon nanofibers, making it difficult to freeze in liquid nitrogen. In addition, the anisotropic honeycomb channel walls were crosslinked to form a high-porosity "Steiner tree" geometry, endowing mechanical stability and effective dissipation of compression energy.

The as-designed carbon honeycomb exhibits elasticity over an ultrawide temperature range, even when exposed to flame and liquid nitrogen. To demonstrate this, the carbon honeycomb was used as a pressure sensor under severe conditions. The pressure sensing properties were measured by assembling a sensor with thermal-stable components and exposing it to alcohol lamp flame (**Fig. 3-14a** and **Fig. 3-13**) and liquid nitrogen (**Fig. 3-14d**), the temperatures of which were approximately 600 °C and −196 °C, respectively.

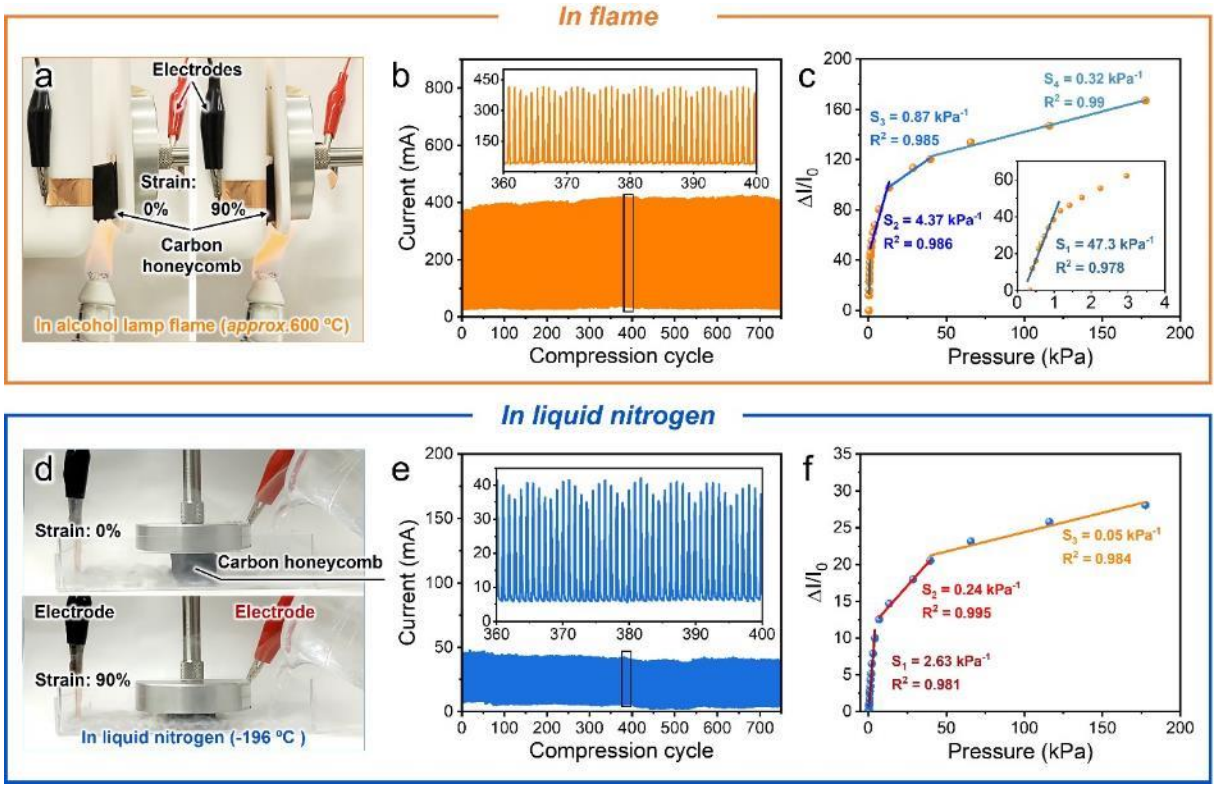


Fig. 3-14 Pressure sensing performance of the chitin nanofiber-derived carbon honeycombs over an ultrawide temperature range. (a, d) Optical images, (b, e) current response at a compression strain of 90% during 750 cycles, and (c, f) relative current change ($\Delta I/I_0$) and

pressure sensitivity (S) over a wide pressure range from 0 to 185.5 kPa in (a−c) alcohol lamp flame and (d−f) liquid nitrogen. Chitin nanofiber concentration: 1.0 wt.%. Carbonization temperature: 900 °C.

In the flame, the current response of the sensor maintains almost the same amplitude without significant changes over 750 compression cycles at a maximum strain of 90% (**Fig. 3-14b**), indicating its pressure-sensing stability. Moreover, the pressure sensitivity in flame was innovatively measured *via* an *in-situ* pressure-current recording system (**Fig. 3-14c**). The sensor demonstrates thermal stability and super elasticity in flame, exhibiting four linear pressure sensitivities of 47.3 kPa^{-1} (0−1.17 kPa), 4.37 kPa^{-1} (1.17−6.52 kPa), 0.87 kPa^{-1} (6.52−40.1 kPa), and 0.32 kPa^{-1} (40.1−177.6 kPa), which are comparable to those at 25 °C. This result indicates that the pressure sensor based on the chitin nanofiber-derived carbon honeycombs is reliable, even when exposed to a flame.

In liquid nitrogen, although the maximum current decreases to approximately 40 mA (**Fig. 3-14e**), the sensor still affords a stable current amplitude upon cyclic compression and release, verifying its excellent pressure-sensing performance. Furthermore, three linear pressure sensitivities of 2.63 (0−4.27 kPa), 0.24 (4.27−38.5 kPa), and 0.04 kPa^{-1} (38.5−172.3 kPa) are obtained (**Fig. 3-14f**), demonstrating its applicability for pressure sensing in ultra-low temperatures. Such results confirm the potential for the practical application of the developed chitin nanofiber-derived elastic carbon honeycombs in extreme environments, such as in electronic devices and outdoor environments with harsh conditions.

The excellent pressure-sensing performance of the chitin nanofiber-derived carbon honeycomb in flames and liquid nitrogen is related to its thermally stable elastic properties and tunable electrical conductivity upon compression. The elasticity even in flames and liquid nitrogen has been reported for ceramic sponges[40] and CNT materials[41], owing to their high thermal stability. The chitin nanofiber-derived carbon honeycomb was also thermally stable even against such harsh conditions. Moreover, the electrical conductivity of the carbon honeycomb changed with the changes in pressure during compression and release, varying the current values and thus demonstrating pressure-sensing performance.

3.4 Conclusion

A chitin nanofiber-derived elastic carbon honeycomb with honeycomb-like anisotropic microstructures was successfully fabricated *via* unidirectional ice templating, freeze-drying, and carbonization. A carbon honeycomb was optimized with a chitin nanofiber concentration

of 1.0 wt.% and a carbonization temperature of 900 °C, which yielded ideal anisotropic honeycomb channels with nanofibrous networks, thin channel walls with few cracks, and weak hydrogen-bonding interactions between the carbonized chitin nanofiber; this resulted in super-elasticity and high compressibility with up to 90% strain, as well as stress and height retentions of 87% and 94%, respectively, after 10,000 cycles of compression. These metrics were better than those of most reported carbon aerogels derived from fossil fuels, biomass, and their composite materials. In addition, an as-tailored carbon honeycomb exhibited robust thermal resistance and compression resilience from −196 to 1000 °C. A high-performance pressure sensor based on the carbon honeycomb demonstrated wide-range pressure detection for various motions. Furthermore, excellent pressure sensitivity was maintained even in a flame and in liquid nitrogen. These outstanding mechanical and electrical properties can potentially enable versatile applications in the future. This strategy paves the way for the multifunctional design of bio-nanofiber-derived carbon materials for diverse applications.

3.5 References

1 S. Long, Y. Feng, F. He, J. Zhao, T. Bai, H. Lin, W. Cai, C. Mao, Y. Chen, L. Gan, J. Liu, M. Ye, X. Zeng and M. Long, *Nano Energy*, 2021, **85**, 105973.

2 B. Wang, S. Li, X. Wu, J. Liu and J. Chen, *J. Mater. Chem. A*, 2016, **4**, 11789–11799.

3 H. Liu, T. Xu, C. Cai, K. Liu, W. Liu, M. Zhang, H. Du, C. Si and K. Zhang, *Adv. Funct. Mater.*, 2022, **32**, 2113082.

4 X. Peng, K. Wu, Y. Hu, H. Zhuo, Z. Chen, S. Jing, Q. Liu, C. Liu and L. Zhong, *J. Mater. Chem. A*, 2018, **6**, 23550–23559.

5 K. H. Kim, Y. Oh and M. F. Islam, *Nat. Nanotechnol.*, 2012, **7**, 562–566.

6 J. Suhr, P. Victor, L. Ci, S. Sreekala, X. Zhang, O. Nalamasu and P. M. Ajayan, *Nat. Nanotechnol.*, 2007, **2**, 417–421.

7 H. Hu, Z. Zhao, W. Wan, Y. Gogotsi and J. Qiu, *Adv. Mater.*, 2013, **25**, 2219–2223.

8 X. L. Wu, T. Wen, H. L. Guo, S. Bin Yang, X. K. Wang and A. W. Xu, *ACS Nano*, 2013, **7**, 3589–3597.

9 K. H. Kim, M. Vural and M. F. Islam, *Adv. Mater.*, 2011, **23**, 2865–2869.

10 Y. Tian, D. Estevez, H. Wei, M. Peng, L. Zhou, P. Xu, C. Wu, M. Yan, H. Wang, H. X. Peng and F. Qin, *Chem. Eng. J.*, 2021, **421**, 129781.

11 Z. Chen, H. Zhuo, Y. Hu, H. Lai, L. Liu, L. Zhong and X. Peng, *Adv. Funct. Mater.*, 2020, **30**, 1910292.

12 S. Ozden, S. Monti, V. Tozzini, N. S. Dutta, S. Gili, N. Caggiano, A. J. Link, N. M.

Pugno, J. Higgins, R. D. Priestley and C. B. Arnold, *Mater. Today*, 2022, **59**, 46–55.

13 Y. Si, X. Wang, C. Yan, L. Yang, J. Yu and B. Ding, *Adv. Mater.*, 2016, **28**, 9512–9518.

14 H. L. Gao, Y. B. Zhu, L. B. Mao, F. C. Wang, X. S. Luo, Y. Y. Liu, Y. Lu, Z. Pan, J. Ge, W. Shen, Y. R. Zheng, L. Xu, L. J. Wang, W. H. Xu, H. A. Wu and S. H. Yu, *Nat. Commun.*, 2016, **7**, 12920.

15 L. Qiu, J. Z. Liu, S. L. Y. Chang, Y. Wu and D. Li, *Nat. Commun.*, 2012, **3**, 1241.

16 C. Chen, J. Song, S. Zhu, Y. Li, Y. Kuang, J. Wan, D. Kirsch, L. Xu, Y. Wang, T. Gao, Y. Wang, H. Huang, W. Gan, A. Gong, T. Li, J. Xie and L. Hu, *Chem*, 2018, **4**, 544–554.

17 Z. Z. Pan, H. Nishihara, S. Iwamura, T. Sekiguchi, A. Sato, A. Isogai, F. Kang, T. Kyotani and Q. H. Yang, *ACS Nano*, 2016, **10**, 10689–10697.

18 M. Murcia-Morales, M. J. Gómez-Ramos, P. Parrilla-Vázquez, F. J. Díaz-Galiano, M. García-Valverde, V. Gámiz-López, J. Manuel-Flores and A. R. Fernández-Alba, *Sci. Total Environ.*, 2020, **710**, 136288.

19 J. Jiang, H. Oguzlu and F. Jiang, *Chem. Eng. J.*, 2021, **405**, 126668.

20 H. Yu, Q. Zhang, B. P. Cumming, E. Goi, J. H. Cole, H. Luan, X. Chen and M. Gu, *Adv. Sci.*, 2021, **8**, 2100141.

21 M. F. Ashby and R. F. M. Medalist, *Metall. Trans. A*, 1983, **14**, 1755–1769.

22 M. Nogi, F. Kurosaki, H. Yano and M. Takano, *Carbohydr. Polym.*, 2010, **81**, 919–924.

23 T. Yeamsuksawat, L. T. Zhu, T. Kasuga, M. Nogi and H. Koga, *Nanomaterials*, 2023, **13**, 1480.

24 L. Zhu, Y. Huang, Y. Morishita, K. Uetani, M. Nogi and H. Koga, *J. Mater. Chem. C*, 2021, **9**, 4444–4452.

25 Y. Gao, X. Chen, J. Zhang and N. Yan, *Chempluschem*, 2015, **80**, 1556–1564.

26 B. Ding, S. Huang, K. Pang, Y. Duan and J. Zhang, *ACS Sustain. Chem. Eng.*, 2018, **6**, 177–185.

27 R. Valentin, B. Bonelli, E. Garrone, F. Di Renzo and F. Quignard, *Biomacromolecules*, 2007, **8**, 3646–3650.

28 Y. Z. Hou, Q. F. Guan, J. Xia, Z. C. Ling, Z. Z. He, Z. M. Han, H. Bin Yang, P. Gu, Y. B. Zhu, S. H. Yu and H. A. Wu, *ACS Nano*, 2021, **15**, 1310–1320.

29 B. Qin, Z. L. Yu, J. Huang, Y. F. Meng, R. Chen, Z. Chen and S. H. Yu, *Angew. Chem. Int. Ed.*, 2023, **62**, e202214809.

30 C. Wang, X. Chen, B. Wang, M. Huang, B. Wang, Y. Jiang and R. S. Ruoff, *ACS Nano*, 2018, **12**, 5816–5825.

31 Z. L. Yu, B. Qin, Z. Y. Ma, J. Huang, S. C. Li, H. Y. Zhao, H. Li, Y. B. Zhu, H. A. Wu and S. H. Yu, *Adv. Mater.*, 2019, **31**, 1900651.

32 L. Feng, P. Wei, Q. Song, J. Zhang, Q. Fu, X. Jia, J. Yang, D. Shao, Y. Li, S. Wang, X. Qiang and H. Song, *ACS Nano*, 2022, **16**, 17049–17061.

33 Y. Hu, H. Zhuo, Q. Luo, Y. Wu, R. Wen, Z. Chen, L. Liu, L. Zhong, X. Peng and R. Sun, *J. Mater. Chem. A*, 2019, **7**, 10273–10281.

34 B. C. Hu, H. R. Zhang, S. C. Li, W. S. Chen, Z. Y. Wu, H. W. Liang, H. P. Yu and S. H. Yu, *Adv. Funct. Mater.*, 2023, **33**, 2207532.

35 J. Zhang, B. Li, L. Li and A. Wang, *J. Mater. Chem. A*, 2016, **4**, 2069–2074.

36 H. Zhuo, Y. Hu, X. Tong, Z. Chen, L. Zhong, H. Lai, L. Liu, S. Jing, Q. Liu, C. Liu, X. Peng and R. Sun, *Adv. Mater.*, 2018, **30**, 1706705.

37 S. R. A. Ruth, V. R. Feig, H. Tran and Z. Bao, *Adv. Funct. Mater.*, 2020, **30**, 2003491.

38 W. Liu, N. Liu, Y. Yue, J. Rao, C. Luo, H. Zhang, C. Yang, J. Su, Z. Liu and Y. Gao, *J. Mater. Chem. C*, 2018, **6**, 1451–1458.

39 H. Liu, X. Chen, Y. Zheng, D. Zhang, Y. Zhao, C. Wang, C. Pan, C. Liu and C. Shen, *Adv. Funct. Mater.*, 2021, **31**, 2008006.

40 C. Jia, L. Li, Y. Liu, B. Fang, H. Ding, J. Song, Y. Liu, K. Xiang, S. Lin, Z. Li, W. Si, B. Li, X. Sheng, D. Wang, X. Wei and H. Wu, *Nat. Commun.*, 2020, **11**, 3732.

41 M. Xu, D. N. Futaba, T. Yamada, M. Yumura and K. Hata, *Science*, 2010, **330**, 1364–1368.

42 X. Li, L. Zhu, T. Kasuga, M. Nogi and H. Koga, *Chem. Eng. J.*, 2022, **450**, 137943.

Conclusions

Chitin nanofiber-derived carbon honeycombs with anisotropic honeycomb microstructures were successfully fabricated via unidirectional ice templating, freeze-drying, and carbonization. Chapter 1 describes the fabrication of a carbon honeycomb, which had anisotropic honeycomb microstructures and defective carbon structures ideal for microwave absorption, using a chitin nanofiber with a concentration of 1.0 wt.% and a carbonization temperature of 800 °C. The anisotropic honeycomb channels exhibited good impedance matching with air and a moderate conductive loss. The defective carbon structures were responsible for the high polarization loss and moderate conductive loss. The carbon honeycomb had a strong microwave absorption of –82.2 dB at 7.22 mm. Chapter 2 describes the successful preparation of a smart microwave absorber with a tunable absorption frequency and switchable absorption/transmission using a tailored chitin-nanofiber-derived elastic carbon honeycomb (1.0 wt.%, 800 °C). The uncompressed carbon honeycomb had a maximum microwave absorption of approximately –40 dB at 6.9 mm owing to its good impedance matching with air and moderate dielectric properties. By compressing the honeycomb from 0% to 20%, 40%, and 60%, the maximum-absorption frequency could be tuned from 10.4 to 11.0, 11.5, 12.1 GHz, respectively, because the thickness of the carbon honeycomb was reduced while preserving its impedance matching and moderate dielectric properties. Further compression of the carbon honeycomb from 60% to 80% could switch it from absorption to transmission by causing an impedance mismatch and by changing the dielectric loss from moderate to low. Chapter 3 describes the fabrication of an elastic and thermally stable carbon honeycomb with a chitin nanofiber concentration of 1.0 wt.% and a carbonization temperature of 900 °C, which yielded ideal anisotropic honeycomb microstructures, thin channel walls with few cracks, and weak hydrogen-bonding interactions among the carbon nanofibers. These optimized fabrication conditions provided the carbon honeycomb with superelasticity and high compressibility up to 90% strain. A pressure sensor based on the optimized carbon honeycomb demonstrated high sensitivity over a wide working pressure range of 0−185.5 kPa and an ultrawide temperature range of −196–600 °C. This study paves the way for the multifunctional design of chitin-nanofiber-derived carbon honeycombs for use in diverse electronic and dielectric applications.

List of Publications

1. Chitin-derived-carbon nanofibrous aerogel with anisotropic porous channels and defective carbon structures for strong microwave absorption

Xiang Li, Luting Zhu, Takaaki Kasuga, Masaya Nogi, and Hirotaka Koga*

Chemical Engineering Journal, **2022**, *450 (1)*, 137943.

DOI: 10.1016/j.cej.2022.137943

https://doi.org/10.1016/j.cej.2022.137943

2. Frequency tunable and absorption/transmission switchable microwave absorber based on a chitin-nanofiber-derived elastic carbon aerogel

Xiang Li, Luting Zhu, Takaaki Kasuga, Masaya Nogi, and Hirotaka Koga*

Chemical Engineering Journal, **2023**, *469*, 144010

DOI: 10.1016/j.cej.2023.144010

https://doi.org/10.1016/j.cej.2023.144010

3. All-nanochitin-derived, super-compressible, elastic, and robust carbon honeycomb and its pressure sensing properties over an ultrawide temperature range

Xiang Li, Luting Zhu, Takaaki Kasuga, Masaya Nogi, and Hirotaka Koga*

ACS Applied Materials & Interfaces, **2023**, In press.

Accepted

DOI: 10.1021/acsami.3c08587

Copyright

The author has obtained the permissions to reuse contents from *Elsevier* and *American Chemical Society*.

Credits

Reprinted from Xiang Li, Luting Zhu, Takaaki Kasuga, Masaya Nogi, and Hirotaka Koga* Chemical Engineering Journal, 2022, *450 (1)*, 137943, with permission from the *Elsevier*.

Reprinted from Xiang Li, Luting Zhu, Takaaki Kasuga, Masaya Nogi, and Hirotaka Koga* Chemical Engineering Journal, 2023, *469*, 144010, with permission from the *Elsevier*.

Reprinted from Xiang Li, Luting Zhu, Takaaki Kasuga, Masaya Nogi, and Hirotaka Koga* ACS Applied Materials & Interfaces, 2023, with permission from the *American Chemical Society*.

Acknowledgement

Even though the COVID-19 epidemic swept the world, I was very lucky to be able to successfully come to Nogi Lab in Osaka University for pursuing my doctor study.

Lost time is never found again. Now, my education as a student will be end. When looking back of the past memory, happiness and pain emerged in my brain. Especially, I would like to thank myself for striving to the end during the PhD study and never gave up.

Firstly, I would like to express my special thanks to Prof. Masaya Nogi snesei, for his guidance and kindhearted encouragement on my scientific research. He always encouraged me to explain the complex scientific problems as simple as possible and make good presentation for wide readership.

I would like to thank my supervisor Prof. Hirotaka Koga sensei, who is a very rigorous and serious scientific researcher. Without his guidance, I would not be able to complete this thesis. I was able to learn a lot of things from him, such as experimental design, data processing, writing papers and so on.

I sincerely thank to Assistant Prof. Takaaki Kasuga sensei, who provided much assistance for the operation of the experimental equipment and reviewing of my published research papers.

I profoundly grateful to Prof. Hiroshi Uyama sensei and Prof. Norimitsu Tohnai sensei for their valuable comments and giving me valuable suggestions on preparation of this thesis.

During my three years of studying in Osaka University, I really appreciate the wonderful moment with my current and previous lab members: Ms. Nodaka Ogata, Ms. Yukiko Tomozoe, Ms. Chika Hashimoto, Ms. Ami Mizui, Ms. Hitomi Yagyu, Ms. Yoshiko Harada, Ms. Mayu Suzuki, Dr. Luting Zhu, Ms. Yunxia Wang, Ms. Yintong Huang, Mr. Thanakorn Yeamsuksawat, Ms. Chenyang Li, Mr. Yoshitaka Morishita, Mr. Keitaro Kasuya, Mr. Jun Shirahama, Mr. Kosuke Takahashi, Ms. Yurika Teraoka, Ms. Chenyun Xin, Mr. Jiahao Wang, Mr. Manabu

Mizukami, Mr. Kazuki Omote, Ms. Miao Chen, Mr. Yunfei Bai, Mr. Yuta Furuyama, Mr. Kazuki Matsumoto, Ms. Yuna Otsuka, Mr. Mirai Nishikawa. Meanwhile, I also would like to thank my friends in China.

I am also grateful to the Japan Science and Technology Agency (JST). This study was partially supported by JST SPRING program (JPMJSP2138). I would like to thank *Editage* (www.editage.jp) for English language editing.

Finally, I would like to express my greatest thanks to my family and Ms. Yujing Bian for their always support and fully understanding without any doubting. I wish the people I love and those who love me health and happiness.

Interest acts as a mentor to accumulate knowledge, and then a good accumulation ensures success in the future.

Li Xiang

産業科学研究所, 大阪大学

2023 年 6 月 14 日